Engineering Journal

American Institute of Steel Construction

Second Quarter 2015 Volume 52, No. 2

www.aisc.org

ENGINEERING JOURNAL

AMERICAN INSTITUTE OF STEEL CONSTRUCTION

Dedicated to the development and improvement of steel construction, through the interchange of ideas, experiences and data.

ENGINEERING JOURNAL (ISSN 0013-8029) is published quarterly. Subscriptions: Members: one subscription, $40 per year, included in dues; Additional Member Subscriptions: $40 per year. Non-Members U.S.: $160 per year. Foreign (Canada and Mexico): Members $80 per year. Non-Members $160 per year. Published by the American Institute of Steel Construction at One East Wacker Drive, Suite 700, Chicago, IL 60601.

Periodicals postage paid at Chicago, IL and additional mailing offices. **Postmaster:** Send address changes to ENGINEERING JOURNAL in care of the American Institute of Steel Construction, One East Wacker Drive, Suite 700, Chicago, IL 60601.

Seismic Response of Partial-Joint-Penetration Welded Column Splices in Moment-Resisting Frames

SEAN M. SHAW, KIMBERLY STILLMAKER and AMIT M. KANVINDE

ABSTRACT

Current standards require that welded column splice connections in special or intermediate moment-resisting frames (SMRFs or IMRFs) feature complete-joint-penetration (CJP) groove welds to develop the full flexural strength of the column. In contrast to partial-joint-penetration (PJP) welds, CJP welds are often costly, requiring additional material, inspection and back-gouging or backing-bar removal to ensure complete penetration. However, unlike welded beam-column connections, which fractured in the 1994 Northridge Earthquake, column splices have modest deformation demands. This suggests that perhaps with modern, toughness-rated weld filler materials and welding practice, PJP welded splices may offer acceptable performance under seismic loads. Motivated by these observations, a study featuring five full-scale tests on PJP-welded column splices is presented to examine their feasibility for use in IMRFs or SMRFs in seismic environments. The test matrix investigates a range of parameters, including column sizes (consistent with use in 4-, 9- and 20-story buildings) as well as variations in connection details (single and double-beveled, welded and unwelded webs, presence of a weld access hole). All specimens utilized columns with specified yield strength 50 ksi for the columns and ultimate strength 70 ksi for the weld electrode. The specimens were loaded cyclically in a three-point bend configuration such that the splice was subjected to demands consistent with those in severe earthquakes; a loading protocol was developed specifically for this purpose based on nonlinear time history simulations. All the full-scale specimens exhibited excellent performance, such that the splices exceeded the moment capacity of the smaller connected column. The full-scale data is complemented by a series of ancillary tests such that the results may be interpreted with respect to measured, rather than specified, material properties. A series of finite element fracture mechanics simulations is also presented to assist with the generalization of test results. The finite element simulations indicate that for the tested connections, the toughness demands are below the minimum expected toughness, suggesting that details similar to the ones tested in the study may be suitable for general use in the field. A synthesis of the test and simulation data is encouraging from the perspective of adoption of PJP welded splices in IMRFs and SMRFs in seismic regions. Limitations of the research are outlined, along with discussion of future work to develop further support for the use of PJP welded splices in moment frames.

Keywords: partial-joint-penetration groove welds, PJP welds, column splices, moment frames.

INTRODUCTION

The 1994 Northridge earthquake revealed the susceptibility of welded beam-to-column (WBC) connections to fracture. Numerous studies associated with the SAC Steel Project (SAC, 1996), such as Engelhardt and Sabol (1994), exhaustively examined the factors responsible for these fractures and developed recommendations for new construction as well as retrofit (FEMA, 2000). By and large, these studies concur that the WBC fractures may be attributed to a combination of low toughness in the base and/or weld material; poor detailing practice, such as the use of backing bars and weld runoff tabs, which produced flaws or cracks in highly stressed regions of the flanges; and connection configurations that did not account for unanticipated stress distributions, such as the amplification of shear and longitudinal stress in the flanges due to inadequate participation of the web connection. Informed by these investigations, subsequent design standards such as the 2010 AISC *Seismic Provisions for Structural Steel Buildings* (AISC 341-10) mandate stringent requirements for material toughness [based on Charpy V-notch (CVN) testing of base and weld material], detailing, and guidelines for connection design and inspection. As a result, the fracture risk in WBC connections has been mitigated to a large extent.

The post-Northridge research discussed previously primarily addressed WBC connections because a vast majority of the fractures during the Northridge earthquake were observed in these connections. However, the broader findings regarding the fracture-susceptibility of details with effect of sharp flaws and brittle materials resulted in updated design requirements for other connections as well. These include column splice connections, which are commonly used in moment frames due to one or more of the following reasons: column sections are typically transitioned to account for changes in loading over the height of the building; the

Sean M. Shaw, Design Engineer, Buehler and Buehler Structural Engineers, Sacramento, CA. Email: sshaw@bbse.com

Kimberly Stillmaker, Graduate Research Assistant, Department of Civil and Environmental Engineering, University of California, Davis, CA. Email: kstillmaker@ucdavis.edu

Amit M. Kanvinde, Associate Professor, Department of Civil and Environmental Engineering, University of California, Davis, CA (corresponding). Email: kanvinde@ucdavis.edu

height of the building is greater than the length of the available section; or shipping constraints and erection practices limit the length of the columns. To reflect the need for more stringent detailing requirements in these connections, AISC 341-10 prescribes the following for intermediate and special moment-resisting frames (IMRFs and SMRFs): "Where welds are used to make the splice, they shall be complete-joint-penetration groove welds."

Figure 1a schematically illustrates a pre-Northridge column splice connection, and Figure 1b indicates a post-Northridge connection designed using the improved guidelines outlined previously. The main difference between the pre- and post-Northridge type connections is that the post-Northridge connections incorporate complete-joint-penetration (CJP) welds in the flanges and the webs (to develop the flexural strength of the column by eliminating the crack-like flaw at the unfused weld root, UWR), whereas the pre-Northridge connections used partial-joint-penetration (PJP) welds, with weld penetration (or effective throat) in the range of 40 to 60% of the flange thickness. The newer splice details with the CJP welds are significantly more expensive to construct for several reasons. First, more weld material must be used because full penetration is required; the volume of weld material is nonlinearly proportional to the extent of penetration. Second, the use of additional weld material requires a greater number of weld passes, requiring surface preparation and cleaning between each pass. Third, and perhaps most important, complete penetration typically requires back-gouging and welding the material near the weld root from the opposite side, such that no part of the connection remains unfused. Alternative processes, such as using a backing-bar are possible as well, although sometimes undesirable due to stability concerns. Finally, demand critical CJP welds require rigorous inspection protocols. It is especially inconvenient and costly to conduct these processes because the splices are always field-welded, often several stories above the ground.

In light of these observations, it is also relevant to reference other aspects of the post-Northridge connections as well as recent research on other welded connections. Specifically, AISC 341-10 identifies the welds in the splices as demand critical welds, requiring that the weld filler metals must meet minimum toughness requirements (minimum CVN energy of 20 ft-lb at 0 °F and additionally, a CVN energy of 40 ft-lb at 70 °F from heat input envelope testing). This is significantly higher as compared to the weld materials used in pre-Northridge connections. For comparison, the E70T-4 weld filler metal typically used in pre-Northridge details exhibited CVN energy values in the range of 5 to 10 ft-lb at 20 °F (Kaufmann and Fisher, 1995). Moreover, AISC 341-10 also requires the column splice to be located either 4 ft away from the floor or at the center of the column if the story height is less than 8 ft. It is considered unlikely that this location (and hence the splice) will be subjected to high inelastic rotation demands, for the following reasons. First, the strong-column-weak-beam (SCWB) requirement encourages the development of plastic hinges in the beams, under first mode response. Second, the absence of transverse load on the column implies that the peak moments are attained at the ends (rather than in the center) of the columns; in fact, under first-mode response that dominates most low-to-mid-rise buildings, the bending moment near the center of the column approaches zero as the column bends in double curvature. Prior analytical research by Shen et al. (2010) indicates that the splices are not subjected to significant inelastic action, even under extreme seismic events. The findings of this research are confirmed by similar simulations conducted as part of the current study (described in a subsequent section of this paper). Finally, recent research on other types of connections by the lead investigator of this study, e.g., Myers et al. (2009), Gomez et al. (2010) and Dubina and Stratan (2002), indicates that when high-toughness materials (similar to those required by post-Northridge design standards) are used, the presence of

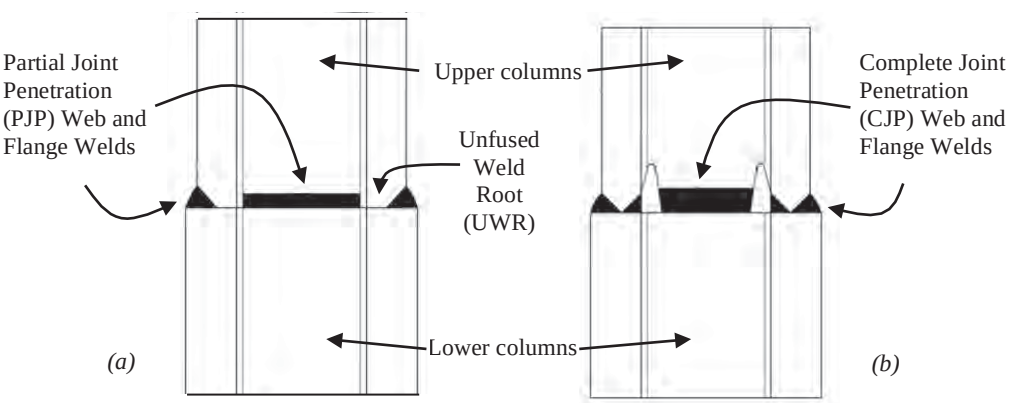

Fig. 1. Column splice construction practice (a) pre-Northridge and (b) post-Northridge. Erection plates on web not shown for clarity.

a flaw or crack-like stress raiser (produced, e.g., due to the UWR) may be tolerated without brittle fracture.

When considered together, the previous observations suggest that inelastic deformation demands in splices may be relatively modest and, even if these demands are present, the use of appropriately designed PJP details may successfully mitigate fracture risk. This is important, considering the expense and inconvenience of constructing CJP welds in column splices. Motivated by these observations, this paper presents a series of full-scale tests on column splice connections welded with PJP welds and high-toughness weld filler metals. The main objective of the study is to investigate the seismic performance of these connections and to examine their feasibility for use in SMRF/IMRF structures in highly seismic environments. The paper begins with a discussion of relevant literature in the area, with the objective of establishing context for the current study. This is followed by a discussion of a series of nonlinear time history simulations that were conducted to characterize the demands in column splices and to develop a loading protocol for the full-scale testing. The column splice tests (which feature Grade 50 base materials and E70 weld electrodes) are then presented, along with analysis and discussion, which also leverages ancillary tests conducted to establish material constitutive and toughness properties. The paper concludes with a discussion of fracture mechanics analysis, which examines the potential for generalization of test results.

LITERATURE REVIEW AND OBJECTIVES

Although guidelines for the design of column splice connections are stringent and similar to other connections such as WBC connections, research directly addressing column splice connections for seismic conditions has been relatively sparse. In fact, the only experimental study on fracture-critical welded column splices was conducted by Bruneau and Mahin (1991) prior to the Northridge earthquake. Other previous studies on column splices (Popov and Stephen, 1976; and Hayes, 1957) have examined the response of spliced columns in compression. The Bruneau and Mahin study featured two column splice specimens, which connected heavy rolled sections (W14×665 connected to W14×500 and W14×426 connected to W14×370), with flanges in the thickness range of 2.6 to 4.5 in. The specimens were constructed to replicate construction practice prevalent at the time in terms of material properties, weld and member sizes, and residual stresses as well as detailing practice and welding procedures. Of these two specimens, one featured PJP welds in the flanges with 50% penetration, whereas the other featured CJP welds with weld access holes. The specimens were subjected to cyclic loading under a four-point bend configuration, such that the splice region was subjected to pure flexure. As a consequence, the effect of shear was not considered. The prominent findings of this study were that the CJP welded splice exhibited excellent performance sustaining moments greater than the cross-sectional strength of the smaller connected column, and although the PJP welded splice failed in a brittle manner, it did so after the net-section strength of the connection (the strength based on the cross-sectional area, discounting the unfused root region) was reached. This implies that locally, the weld material had sufficient toughness to allow yielding over the entire weld ligament (the connected portion), even if the corresponding strength was not sufficient to prevent brittle fracture of the connection when considered at the component scale.

The latter is an important observation in the context of the present study because weld and base materials used in the Bruneau and Mahin (1991) tests were not subject to minimum toughness requirements, which were enforced after the Northridge earthquake and ensuing research. As outlined in the introduction, toughness of contemporaneously used weld filler metals (such as E70T-4) is significantly lower than what is currently required. Thus, the performance of PJP connections in the Bruneau and Mahin study indicate the possibility of successfully using toughness rated filler materials with PJP weld details.

Nuttayasakul (2000) conducted fracture mechanics based finite element simulations of the Bruneau and Mahin (1991) tests, as well as additional parametric simulations of column splice details with PJP welds. The finite element study confirmed the internal stress distributions determined by Bruneau and Mahin. The fracture mechanics simulations also suggest that despite the absence of a minimum specified toughness, pre-Northridge weld materials may have had sufficient toughness to develop the net-section strength (at the weaker base metal) of the PJP connection, if an adequate degree of effective throat thickness (approximately 70% of the flange thickness, assuming an overmatched weld) were provided.

Shen et al. (2010) conducted a series of nonlinear time history simulations to examine seismic demands in column splices. Given the absence of similar studies prior to this, the primary aim of the Shen et al. investigation was to develop understanding of the force and deformation demands in column splices such that the margin of safety provided by current design/detailing practice could be evaluated, with a possibility of lowering the stringency of detailing requirements. The nonlinear time history simulations were conducted for 4-, 9- and 20-story moment frame buildings subjected to a suite of 20 ground motions representative of the Southern California region. The simulations revealed that even under extreme ground motions (consistent with MCE or maximum considered earthquake levels), the inelastic deformation demand in the splices is negligible, when interpreted at the macro-scale (or cross-sectional

level). However, the force demands approach the capacity of the smaller connected column. Shen et al. (2010) characterized the force demands in terms of a *P-M* interaction ratio, *IR*, which reflects the combined effect of the axial tension and bending moment, such that an IR of 1.0 implies tensile yielding at the flange of the smaller (upper) connected column. This is because owing to the UWR, splice fracture is sensitive to a peak tensile stress in the flange of the connection. Consequently, the *IR* is an appropriate indicator of splice distress. As expected, the demands were highest (with a peak *IR* approximately equal to 1.0) for the 20-story building because of higher overturning moments, increasing the axial tension in the exterior columns and the pronounced participation of higher dynamic modes, resulting in single-curvature bending of some columns. The latter effect was dominant. For the 4- and 9-story frames, the force demands were significantly lower—peak *IR*, computed over all the motions for the 4-story frame was in the range 0.35 to 0.8, whereas for the 9-story frame it was in the range of 0.5 to 0.9.

A synthesis of these three studies on column splices, along with other research (e.g., Myers et al., 2009) that focused on the deformation capacity of other PJP welded connections (such as column base plates), yields the following observations:

1. The testing by Bruneau and Mahin (1991) and complementary finite element simulations by Nuttayasakul (2000) suggest that even without the enforcement of current toughness requirements, pre-Northridge type PJP welds offered sufficient toughness to develop the net-section strength of the welded flanges, provided sufficient weld penetration was provided.

2. While column splices may be subjected to high force demands (approaching the capacity of the smaller connected column), the inelastic deformation demands are minimal or absent.

3. Other types of connections that incorporate PJP welds (base plate connections featuring notch-tough material compliant with the AISC *Seismic Provisions*), tested by Myers et al. (2009) and more recently Gomez et al. (2010), show excellent performance with the capacity to fully develop the column flanges in yielding.

Based on these observations, the specific objectives of the study presented in this paper are:

1. To experimentally examine the performance of various PJP-welded column splices under a test protocol representative of seismic loading.

2. To conduct a program of ancillary material tests and fracture mechanics analysis to examine the feasibility of these connections in steel moment frame construction in seismic regions.

The next section describes the nonlinear time history simulations conducted for assessment of demands in the splices and the loading protocol developed from these simulations.

NONLINEAR TIME HISTORY SIMULATION, DEMAND CHARACTERIZATION AND DEVELOPMENT OF LOADING PROTOCOL

An understanding of seismic demands in column splices in moment frames is critical for two reasons. First, it provides context for evaluating the vulnerability of splices that may be constructed using PJP welds. Second, and perhaps more important to this study, an analysis of the demands enables the development of a loading protocol for application to the full-scale splice specimens described in the next section. The development of such a protocol is necessary, because existing protocols for SMRF components (Gupta and Krawinkler, 1999) address seismic demands only in deformation-controlled components (such as beam-to-column connections). Column splices in SMRFs are primarily load-controlled, because inelastic deformations are not expected at the component level, albeit local yielding in the weld region is possible. Protocols for these types of components (specifically splices) are not available, nor is it appropriate to adapt protocols developed for deformation-controlled components. Consequently, the large-scale testing requires the development of loading histories that represent seismic demands at the splice in a reasonable, yet conservative manner. A comprehensive program of nonlinear time history simulations was conducted, with the specific objective of assessing splice demands in the context of developing a loading protocol. The simulations conducted in this study are targeted specifically toward the development of loading protocols. It is relevant to discuss here that previous nonlinear time history simulations targeted toward the development of loading protocols (e.g., Gupta and Krawinkler, 1999) have employed ground motions that are scaled such that they represent a target probability of exceedance, such as 10% in 50 years (also expressed as a 10/50 hazard). Figure 2 indicates the buildings used for the nonlinear time history simulations used in this study, whereas subsequent discussion addresses the nonlinear time history simulation and protocol development.

1. Three generic frames (4-, 9- and 20-story) were used—see Figure 2. These are identical to the frames used by Shen et al. (2010) and are adapted from the SAC model buildings (Gupta and Krawinkler, 1999), with the exception that the 3-story SAC model building was replaced by a 4-story building to accommodate the splice (which is uncommon for shorter buildings). The frames have fundamental periods of 0.93, 1.75 and 2.33 s, respectively. The frames were assumed to be constructed for a seismic environment

(and typical gravity loading) consistent with the Los Angeles, California, region assuming firm soil conditions (NEHRP site class D). Refer to Shaw (2013) for more details regarding the building designs. Figure 2 shows the frames, including the locations of the splices (located 4 ft from the top surface of the beam in the lower story).

2. Each frame was subjected to a suite of 20 ground motions. These motions, developed during the SAC steel project (Somerville et al., 1997) are titled LA21-LA40, and are based on recordings from the 1994 Northridge, 1995 Kobe, 1989 Loma Prieta and the 1974 Tabas earthquakes, in addition to simulated motions. The ground motions were scaled to match two spectra, consistent with the 10/50 and 2/50 hazard (per ASCE 7-10) at a general location in the Los Angeles basin. Thus, a total of 40 motions (20 × 2 scaling levels) were used.

3. The simulations were conducted on the platform OpenSEES (2009), which has the capability to simulate several physical aspects of response. The specific modeling considerations included:

   - The use of fiber sections for simulation of the beams and columns to represent axial-moment interaction and the spread of plasticity. The fiber sections utilized a bilinear steel material model with kinematic hardening. Material parameters were calibrated to match a comprehensive data set of plastic hinge response compiled previously by Lignos et al. (2011). The calibrated values of the parameters are E = 29,000 ksi, F_y = 55 ksi (to account for material overstrength with respect to specified strength) and the post-yield (hardening) slope of 1.7% of the initial elastic modulus.
   - Finite joint sizes were modeled. This is especially important because flexural demands at the splice are sensitive to its distance from the end of the column (at the beam face).
   - Geometric nonlinearity effects (P–δ and P–Δ) were modeled.

Several variables were monitored during the nonlinear time history simulations. While the interstory drift and inelastic rotations are of interest, the time histories of longitudinal stress at the locations of the splices (specifically in the flange regions) are determined to be the most critical in the context of this study. This is because the primary concern with respect to the PJP welded splices is fracture at the UWR (see Figure 1). This type of fracture may be considered stress-controlled, because the inelastic deformation (at the splice component level) is modest or negligible. Because both bending and axial force (due to overturning effects) contribute to the longitudinal stress, each flange within each splice is subjected to a different stress history. Recognizing this, the time history of the longitudinal stresses at the extreme fiber of the splices (in the smaller connected column) was monitored for each flange within each splice,

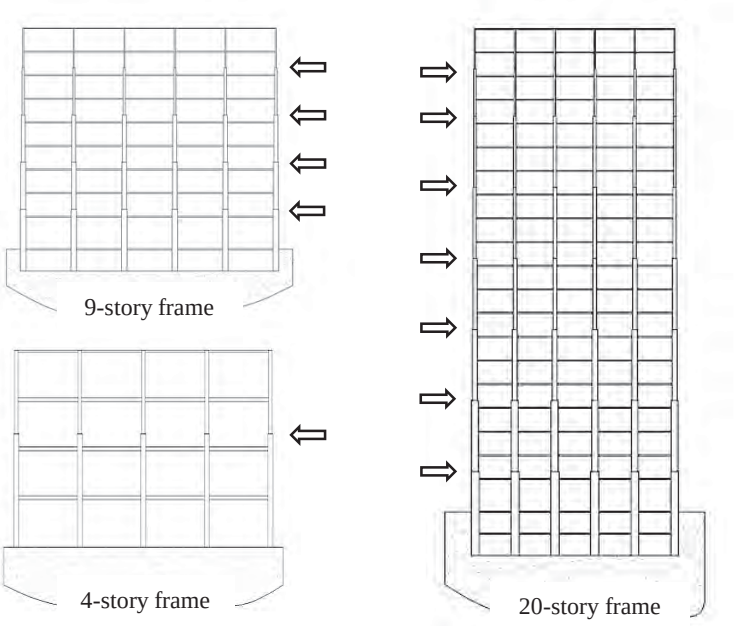

Fig. 2. Schematic illustration of the three model buildings with arrows indicating spliced stories.

Table 1. Summary of Results from Nonlinear Time History Simulations								
	Ground motions scaled to 10/50 hazard				Ground motions scaled to 2/50 hazard			
Frame	IR_{peak}^{median}	IR_{peak}^{max}	Δ_{peak}^{median}	Δ_{peak}^{max}	IR_{peak}^{median}	IR_{peak}^{max}	Δ_{peak}^{median}	Δ_{peak}^{max}
4-story	0.16	0.30 (3E)[a]	1.1%	2.9% (2)[b]	0.30	0.54 (3E)	2.4%	6.1% (2)
9-story	0.11	0.30 (2E)	0.8%	1.6% (3)	0.23	0.72 (2I)	2.0%	5.4% (4)
20-story	0.18	0.72 (5E)	0.6%	1.5% (16)	0.22	0.95 (5E)	1.1%	2.5% (2)

[a] Value in parentheses indicates location of occurrence of IR_{peak}^{max}; (3E) indicates third-story exterior column, while (2I) indicates the second-story interior column.

[b] Value in parentheses indicates location of occurrence of Δ_{peak}^{max}; (4) indicates fourth story.

for each of the nonlinear time history runs. The interaction ratio, *IR*, is a convenient indicator of the stress in the flange, normalized by the yield strength of the flange material, such that $IR = 1.0$ implies tension yielding at the extreme fiber of the cross-section. Table 1 provides an overview of the results of the nonlinear time history simulations for the three frames.

The table includes the maximum value and the median value of IR_{peak} determined from 20 nonlinear time history simulations (for each of the scaling levels). The IR_{peak} value presented in the table reflects the combination of axial force and moment that produces the peak tensile stress in any of the splice flanges. The corresponding flange is considered the critical flange for that nonlinear time history run. Corresponding statistics are also presented for the peak interstory drift, Δ_{peak} (observed in any of the stories within a nonlinear time history run). Referring to the table, the following observations may be made regarding frame and splice response:

1. For the 4-story frame, the interaction ratios are fairly modest. For example, IR_{peak}^{max} for the 10/50 and 2/50 motions are 0.30 and 0.54, respectively. This suggests that for low-rise frames, the tensile stress in the flanges is well below the yield stress. This is consistent with intuition because the response of the 4-story frame is dominated by the first mode resulting in points of inflection near the center of the columns; thereby lowering the moment at the splice and the effects of overturning moment and the associated axial tension are modest as well.

2. For the 9-story frame, the IR_{peak}^{max} are 0.30 and 0.72 for the 10/50 and 2/50 motions, respectively. These are somewhat larger as compared to the corresponding values for the 4-story frames, presumably because both the effects described previously—mode of deformation as well as overturning moments—are more prominent. However, even these are significantly lower as compared to the capacity of the smaller connected column.

3. The splices in the 20-story frame are subjected to demands that are by far the most severe. For this frame, IR_{peak}^{max} for the 10/50 and 2/50 are 0.72 and 0.95, respectively, indicating that demands approach the capacity of the smaller connected column (for the 2/50 hazard), due to a combination of higher-mode response, overturning effects and the larger dynamic forces.

Referring to Table 1, for all the frames, the interstory drift ratios are in the anticipated range. While the peak tensile stress (implied by IR_{peak} is an important parameter with respect to splice fracture, it is not appropriate to entirely disregard history effects in the development of the loading protocol, because the material at the tip the of UWR is also subject to local inelastic cyclic strain. To address this, a rigorous approach was adopted following the methodology originally developed for moment frame connections by Gupta and Krawinkler (1999), subsequently adapted by Richards and Uang (2006) and more recently Fell et al. (2009) for other components. Figure 3 schematically illustrates the loading protocol developed during this study for application to splice specimens. A detailed description of protocol development is provided in Shaw (2013), whereas the main features are briefly summarized as follows:

1. The primary objective of the loading protocol is to subject the PJP welds in the splice tests to stresses (including stress peaks and stress histories) that represent conservative as well as realistic demands consistent with specific seismic hazards.

2. The protocol is constructed in terms of the ratio $M_{splice} / M_p^{smaller-section}$, where M_{splice} is the applied (or demand) moment and $M_p^{smaller-section}$ is the plastic moment capacity about the major axis of the smaller column section, including the effect of material overstrength, taken as $M_p^{smaller-section} = R_y F_y Z_x$. Although the stresses in the splices (in archetype frames and in the nonlinear time history simulations) are a result of axial force and moments, the test apparatus (discussed in the next section) can apply only bending loads. The

loading protocol was developed such that the longitudinal stresses in the flange generated in the bending-only configuration are consistent with those implied by the nonlinear time history simulations, which are a combination of axial and bending stresses.

3. Careful consideration was given to stress-history effects. For this purpose, the following steps were carried out:

   - Each stress history was converted into equivalent constant amplitude cycles using the rainflow counting method (Matsuishi and Endo, 1968).
   - Based on these equivalent cycles, a statistical analysis of the important history parameters (e.g., the peak interaction ratio, the number of damaging cycles and cumulative stress amplitudes) was conducted with respect to the response data from the different ground motions.
   - At this point, the protocol was heuristically constructed to match or exceed specific statistical indicators (percentile values) of these history parameters. As discussed previously, Shaw (2013) provides a detailed description of these history parameters, the rationale underlying their selection, and their use in the development of the protocol.

4. Referring to Figure 3, the loading protocol indicates several checkpoints marked by text on the loading history. For example, one of the points is identified as 9_{max}. The implication is that at this instant in the protocol, all the history indicators (indicative of damage) have been exceeded with a 100% probability in the critical flange of the 9-story frame, for all ground motions scaled to the 2/50 hazard. The primed values on Figure 3 indicate that similar demands have been met or exceeded in the other flange of the specimen (the one that is subjected to tension during the first excursion). Note that this is more conservative than the benchmark established by Gupta and Krawinkler (1999) for qualification for welded-beam-to-column connections (which utilized 86 percentile values from the 10/50 motions). The implication of this is that if a test specimen survives a particular checkpoint on the protocol, it suggests that the connection is a candidate for qualification under demands implied by that checkpoint. By extension, survival through the entire protocol suggests that the splice detail may withstand demands consistent with those in 4-, 9- and 20- story buildings.

The next section describes the full-scale testing on column splices based on this protocol, along with a summary of ancillary material testing.

SPLICE COMPONENT TESTS

This section provides a detailed overview of the splice component tests, including the test setup, instrumentation, specimen fabrication, and finally, the test results. Table 2 includes

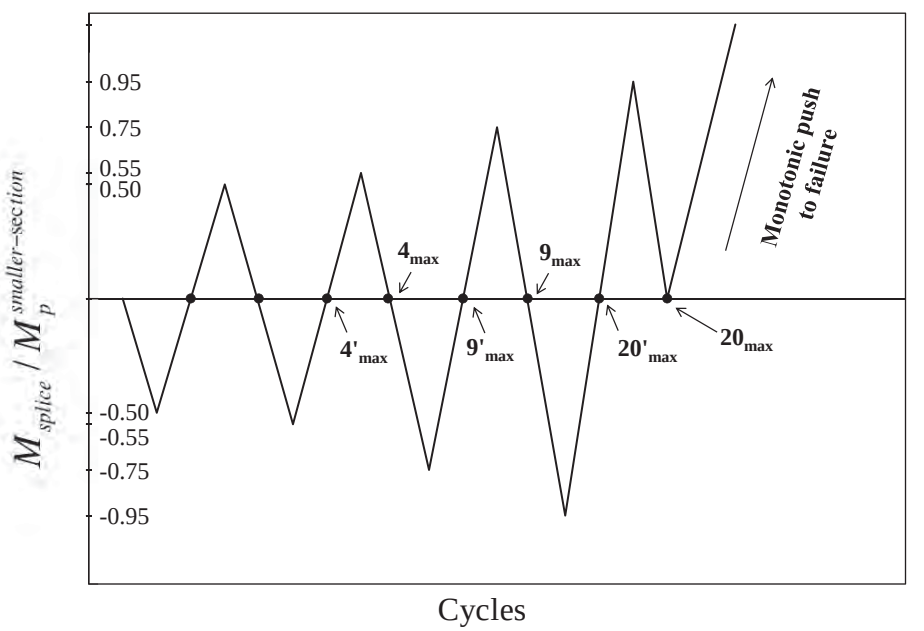

Fig. 3. Loading protocol.

Table 2. Test Matrix and Summary of Key Results							
	Specimen Details			Results[a]			
Test	Column Sizes	Weld Pen	Remarks[b]	$\frac{M_{splice}^{max}}{M_p^{smaller-section}}$	$\frac{V_{splice}^{max}}{V_y^{smaller-section}}$	$\frac{\sigma_{flange}^{max}}{F_y^{flange}}$	$\frac{\delta_{midspan}}{\delta_y}$
24A	W24×370 W24×279	82% F[c] 87% W	Single external bevel, no access hole	1.13	0.85	1.31	4.8
24B	W24×370 W24×279	82% F 87% W	Single external bevel, no access hole	1.19	0.89	1.33	5.8
14A	W14×730 W14×550	82% F 87% W	Double beveled with access hole	1.37	0.93	1.34	16.1
14B	W14×455 W14×342	55% + 40% F[d] 84% W	Double beveled with no access hole, internal flange weld terminated short of web fillet	1.24	0.86	1.34	5.0
14C	W14×145 W14×132	89% F 0% W	Single external bevel, no access hole, bolted web plate	1.04	0.72	1.43	2.0

[a] All referenced material properties are measured (see Table 3), rather than specified.
[b] All details are shown schematically in Figure 5.
[c] Flange and web welds denoted with F and W, respectively.
[d] 55% External flange weld, with 40% Internal flange weld terminated short of web fillet (see Figure 5c).

the test matrix summarizing key features of the five tests that were conducted. Also included in Table 2 are some of the test results, discussed later. The column sizes used in these experiments are consistent with those commonly used in design practice. For example, specimen 14A features one of the heaviest available W-sections (W14×730 connected to a W14×550). The tests may therefore be considered full-scale.

Specimen Construction Process

Because the performance of the PJP splices is sensitive to the execution of the weld details, it is especially important that the welds in the test specimens are representative of field welds. To ensure this, specimen fabrication and erection, including weld procedures, closely followed the processes and practices consistent with field implementation. The following process was implemented:

1. Steel column sections were procured from an AISC certified fabricator and erector. Mill certificates summarizing material yield, ultimate, and toughness properties were provided along with these sections. Data from these mill certificates is provided in Table 3.
2. The sections were shipped to a fabricator where the connection details were prepared; this included surface preparation for the weld bevels and the fabrication of erection plates.
3. The site-ready subassemblies were shipped to a steel erector where column sections were welded in a vertical position in an effort to minimize variance from field conditions.
4. These types of groove welds are not currently allowed in seismic force resisting systems. As a result, a new welding procedure specification (WPS) was created for these welds. While details of the WPS are available in Shaw (2013), the main parameters of the WPS were:
   - FCAW-S welding with E70T-6 electrode (Lincoln NR-305); 3⁄32-in. diameter.
   - Deposit rate (travel speed) was 12-10 in./min.
   - Minimum preheat temperature 350 °F (this is conservatively in excess of the 225 °F minimum required by AWS D1.1-2004 due to the welding of jumbo sections); interpass temperature between 350 and 500 °F.
   - Current: 430–470 A; Voltage: 25–26 V.
5. A procedure qualification record (PQR) was created to support the welding procedure. Data from the PQR testing (on a mockup assembly constructed to represent the splice welds) is provided in Table 3, along with similar data for the base metals (obtained from the mill certificates).

Table 3. Material Tensile and Toughness Data from Ancillary Testing								
Material source ↓		**F_y[a] (ksi)**	**F_u[a] (ksi)**	**F_y/F_u[a]**	**Elongation[a] (%)**	**CVN[a] at 0 °F ft-lb**	**CVN[a] at 70 °F ft-lb**	**CVN[a] at 70 °F ft-lb**
Applicable requirement[b] →		**50-65 ksi**	**≥65 ksi**	**≤0.85**	**≥21%**	**≥20 ft-lb**	**≥20 ft-lb**	**≥20 ft-lb**
Base metal Test 24A	W24×370	55.1	70.3	0.78	34	Not applicable		149
	W24×279	56.8	71.7	0.79	39			200
Base metal Test 24B	W24×370	54.5	70.2	0.78	38			149
	W24×279	56.9	71.9	0.79	33			200
Base metal Test 14A	W14×730	56.2	71.0	0.79	34			292
	W14×550	53.8	70.5	0.76	38			227
Base metal Test 14B	W14×455	57.0	73.9	0.77	36			297
	W14×342	52.8	71.3	0.74	28			104
Base metal Test 14C	W14×145	75.4[4]	87.2	0.86[c]	21			Not applicable[d]
	W14×132	54.2	77.7	0.70	31			
Weld	**PQR**	All-weld coupons were not tested for tensile properties, only toughness tests were conducted				52	Not tested	Not applicable
	W14B post test					Not tested	50	

[a] Average data from three coupon tests.
[b] Based on AISC 341-10.
[c] Does not meet applicable standard.
[d] Base material toughness requirements are only applicable to heavy sections, both W14×145 and W14×132 are not categorized as heavy as per the 14th edition Steel Construction Manual (AISC, 2011).

6. Upon completion, all the welds were inspected visually and with ultrasonic testing by independent inspectors. During this process, a crack was discovered at the root pass of specimen 14C. The deficient weld was removed and re-welded. Subsequent inspection of the repaired weld revealed no cracks.

These construction processes are common to all specimens; specific weld details are discussed in the subsection on experimental response.

Ancillary Testing for Characterization of Material Toughness and Constitutive Properties

The large scale tests were complemented by a comprehensive program of ancillary tests, summarized in Table 3. Table 3 also summarizes the permissible values for each quantity measured in the ancillary tests. The program comprised the following types of tests.

Tension Tests

A total of 30 coupons (three replicates from the smaller column and larger column section of each of the five large-scale test specimens) were tested to establish yield and ultimate properties for the base materials. Referring to Table 3, the yield, ultimate and elongation properties are mostly within the permissible range, with the exception of the material for W14×145 that exhibited strengths higher than the maximum allowable. However, the W14×145 is the larger column within specimen 14C, whereas the test protocol and benchmark performance is expressed in terms of the strength of the smaller column.

Charpy V-Notch Tests

Tests were conducted on coupons extracted from the base as well as weld material. For the base material (heavy sections), AISC 341-10 requires a minimum CVN toughness of 20 ft-lb at 70 °F for specimens extracted from the core of the cross section. For demand-critical welds, the minimum requirement is 20 ft-lb at 0 °F. In addition, a value of 40 ft-lb at 70 °F from heat input envelope testing is also required for the weld filler metal (to qualify the electrode). To support the weld procedure specifications for the current testing program, and to provide insight into the response of the fabricated connections, the following supplementary data was obtained:

- *CVN coupons from the PQR weld assembly.* This involved the testing of CVN coupons at 0 °F to demonstrate that the joint could meet AISC 341-10 by exhibiting a CVN energy of 20 ft-lb at this temperature. Referring to Table 3, a value of 52 ft-lb (well in excess of 20 ft-lb) was obtained.

- *CVN coupons from the compression flange of specimen 14B*. Additional CVN coupons were extracted from the compression (unfractured) flange of one of the full-scale test specimens after the completion of the test; these were tested at 70 °F. The toughness data from these tests does not reflect the intent of AISC 341-10 given that the compression flange is subjected to several inelastic cycles before the CVN extraction and testing. However, these tests provide an indication of the toughness of the as-deposited weld at room (or test) temperature. The average CVN value (from 3 coupons) was 50 ft-lb.

In addition to establishing compliance with applicable standards, the ancillary tests serve both to enable the interpretation of full-scale data with respect to measured, rather than specified material properties, and to enable the calibration of material constitutive and fracture toughness properties in finite element simulations (discussed in a subsequent section).

Test Setup and Instrumentation

Figure 4 schematically illustrates the test setup used for testing. Several factors controlled the design of the setup, including limitations in the size, configuration and capacity of the testing machine as well as the necessity to provide loading and boundary conditions that reflected field conditions with realism.

The specimens were all tested as beams in three-point bending, with a load applied at midspan. The splice is located at a distance of 18 in. from midspan, such that it is subjected to a combination of flexure and shear.

The testing machine applies load only in the downward direction. Cyclic loading was applied by rotating or flipping the specimen about its longitudinal axis after every loading excursion implied by the loading protocol shown previously in Figure 3. Although the loading apparatus cannot apply axial tension, the loading protocol is developed such that flange stresses are consistent with those produced due to a combination of axial tension and bending in building columns.

All specimens were loaded in an identical manner: cyclic loading was applied at midspan as per the loading protocol, until either failure was observed or the machine capacity was exceeded (the latter happened only in the case of specimen 14A). Note that the values in the loading protocol are the moments at the splice location normalized by the expected strength ($M_p^{smaller-section} = R_y F_y Z_x$) of the specimen; these

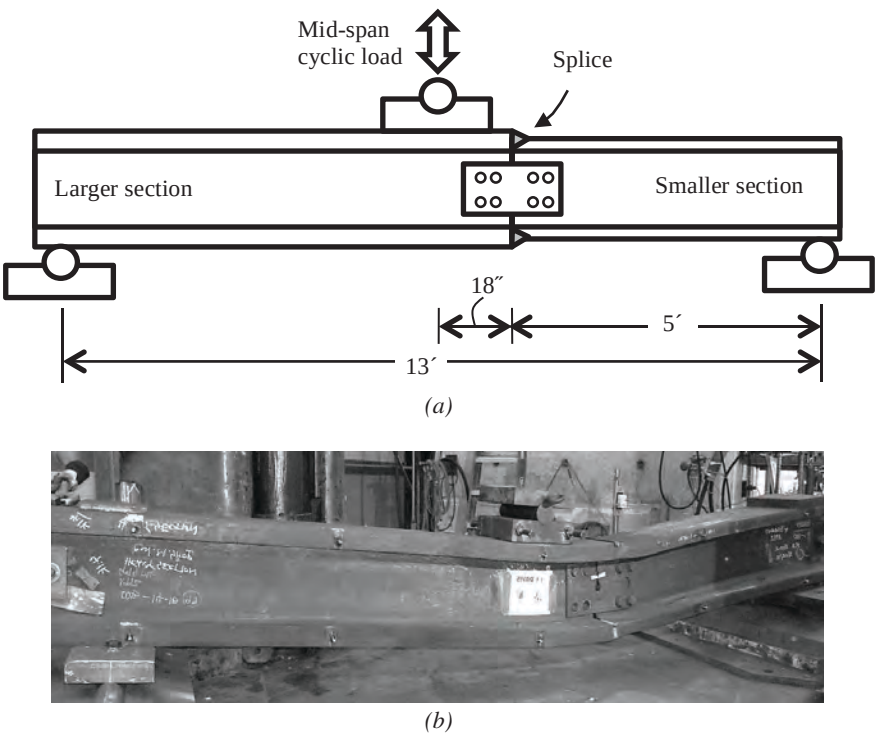

Fig. 4. (a) Schematic illustration of test setup, and (b) specimen 14B overview after test.

were converted to an equivalent midspan load for testing. The specimens were extensively instrumented. The primary control variable was the midspan force, and the associated splice moment. The midspan and splice deflections were also monitored. Strain gages were placed at multiple locations, including the flanges of the splices and the webs. The purpose of the web strain gages (rosettes) was to examine the distribution of shear between the web and the flanges. These are especially relevant for the bolted web connection (specimen 14C), in which the load path for the shear force is not as rigid as for the other (welded web) specimens. Secondary instrumentation was installed to monitor unanticipated response such as out-of-plane buckling. However, this type of response was not observed for any of the tests. The instrumentation was complemented by still and video cameras. Being supported by the Network for Earthquake Engineering Simulation (NEES), all the data from the project is freely available for download from the NEES data repository.

Test Matrix

Referring to the test matrix shown previously in Table 2, five specimens were tested. The main consideration in the selection of the section sizes was realism, such that these sections are of a comparable scale to those typically specified in moment frames. Testing archetype-scale components is especially important in the context of weld fracture because scale-effects in fracture (Bažant, 1984; Anderson, 1995) are well known, wherein fracture mechanics must be invoked, often with some subjectivity, to generalize test results. Also, the thermo-mechanical process of heat-transfer, cooling and phase change that occur during welding affect weld toughness and may be scale dependent, especially if multi-pass welds are used. Finally, the residual stress patterns in large specimens are likely to be different than those developed in small-scale specimens due to the constraint to shrinkage provided by the larger sections. All details were designed in consultation with the steel fabricator and erector, as well as AISC, to provide an efficient means of obtaining the desired level of weld penetration representative of future practice (if, based on this study, PJP welds are determined to be suitable for column splices). Highlights of the test matrix are as follows (refer to Table 2):

1. **Tests 24A and 24B.** Two replicate specimens featuring W24 columns (specifically W24×279 attached to W24×370) were tested. The size of these sections is representative of usage in 15- to 20-story moment frame buildings. Figure 5a schematically illustrates the splice detail for these specimens. The flanges (2.09 in. for the W24×279 and 2.72 in. for the W24×370) were connected with one PJP weld on the outside of the flange, equivalent to 82% penetration with respect to the smaller (W24×279) flange. Because only an external weld with a single bevel was used, a weld access hole was not provided in the web. The web featured a single beveled PJP weld with 87% with respect to the thinner (W24×279) web. A bolted erection plate, sized for erection loads, was provided as also indicated in Figure 5a.
2. **Test 14A.** This specimen was fabricated from a W14×730 column connected to a W14×550; which are two of the heaviest available W-sections. In fact, the flange sizes are 4.91 and 3.82 in. for the larger and smaller columns, respectively, requiring the largest possible weld in a column splice for W-sections. Figure 5b schematically illustrates the splice detail for this specimen. The flanges were double beveled and welds were provided on the inside and outside of the flanges. The total connected penetration was 82% with respect to the smaller (W14×550) flange. A weld access hole (in compliance with AWS D1.8, 2009) was provided in the web. The web featured a single-sided PJP weld with 87% penetration. Similar to the W24 specimens, a bolted erection plate was provided. This plate was ground to follow the contour of the weld access hole.
3. **Test 14B.** This specimen was fabricated from a W14×455 column connected to a W14×342, which have flange sizes 3.21 and 2.47 in. for the larger and smaller columns, respectively. Referring to Figure 5c, the flange of the smaller column was double beveled, similar to specimen 14A. The external weld penetration was 55%, whereas the internal weld penetration was 40% (with respect to the thinner flange). However, the internal bevel (and weld) was stopped short of the web fillet. Thus, the detail was designed to examine the performance of a cost-effective connection that did not require a weld-access hole. From a fracture mechanics perspective, this absence of the continuous weld on the inside of the flange generates a large unfused area in the k-region of the columns. An erection plate was provided, similar to the W24 specimens.
4. **Test 14C.** This specimen features the smallest specimens, a W14×145 connected to a W14×132. These member sizes are representative of those typically used in low-to-mid-rise frames (roughly 2 to 5 stories tall), which constitute a large percentage of the building stock. The flange of the smaller column was provided with a single, external bevel and a PJP weld with 89% penetration. No weld access hole was provided. The distinguishing characteristic of this specimen was that the webs of the columns were not welded; rather, a bolted web-splice plate was provided for shear transfer

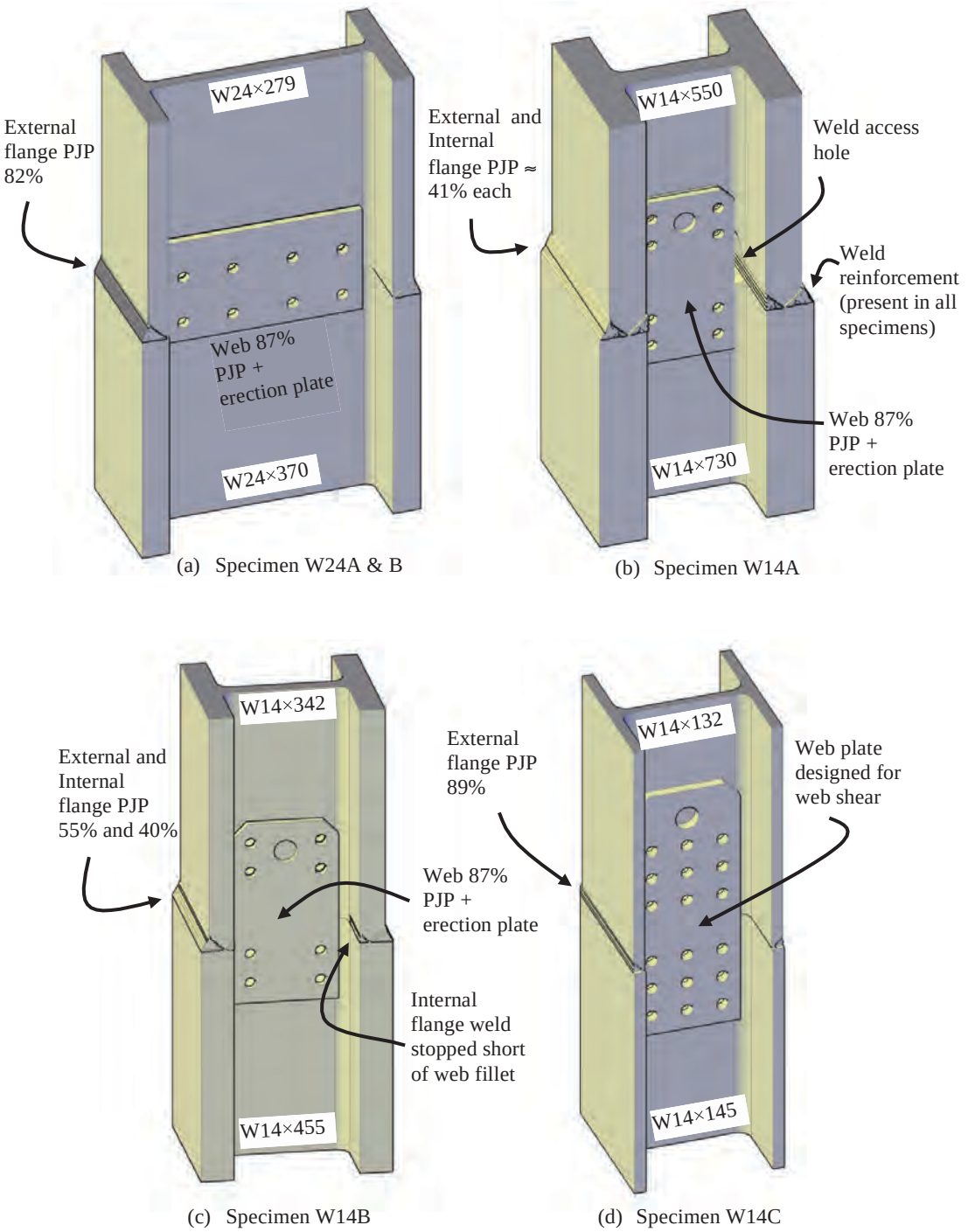

Fig. 5. Splice connection details.

between the webs. Post-Northridge research (FEMA, 2000) indicated that bolted webs are inefficient in transferring shear, producing secondary bending in the flanges and increasing the susceptibility to premature fracture. However, referring to previous discussion, Table 1, and the loading protocol shown in Figure 3, recall that the force demands for low-to-mid-rise frames are rather modest, with $IR_{peak}^{max} < 0.5$. With this consideration, specimen 14C was designed in this manner to explore the possibility of an economical connection for low-to-mid-rise frames. The web plate was designed to develop the full shear capacity of the web, and the bolt pattern was determined assuming an eccentrically loaded bolted connection (Shaw, 2013). Figure 5d illustrates this detail schematically.

For all the specimens, a smooth transition was obtained between the thicker and the thinner flange (indicated on Figure 5a, but representative of all the specimens), in compliance with AWS D1.8 (2009). This has two implications. First, the flared shape of the weld provides reinforcement at the section of the UWR. Second, no sharp discontinuities or re-entrant corners, other than the UWR itself, are present in the detail. The next section describes the qualitative and quantitative results from the splice experiments.

Experimental Observations

Table 2 summarizes results from all the tests. All the specimens survived the cyclic portion of the loading history (shown in Figure 3), and all (with the exception of specimen 14A, which did not fail because machine capacity was reached) failed during the final monotonic push. This implies that all specimens exhibited excellent performance when assessed in the context of demands imposed by the loading protocol. Figures 6a through 6d illustrate the load-deformation response of all the splice connections. The loads indicated on Figure 6 are expressed in terms of the moment at the splice (normalized by the plastic moment, based on measured material properties) versus the midspan deflection. The primary indicators of performance are the peak moment at the splice—this was always observed during the final cycle; the estimated stress in the flange at the splice; and the peak shear at the splice. These quantities are

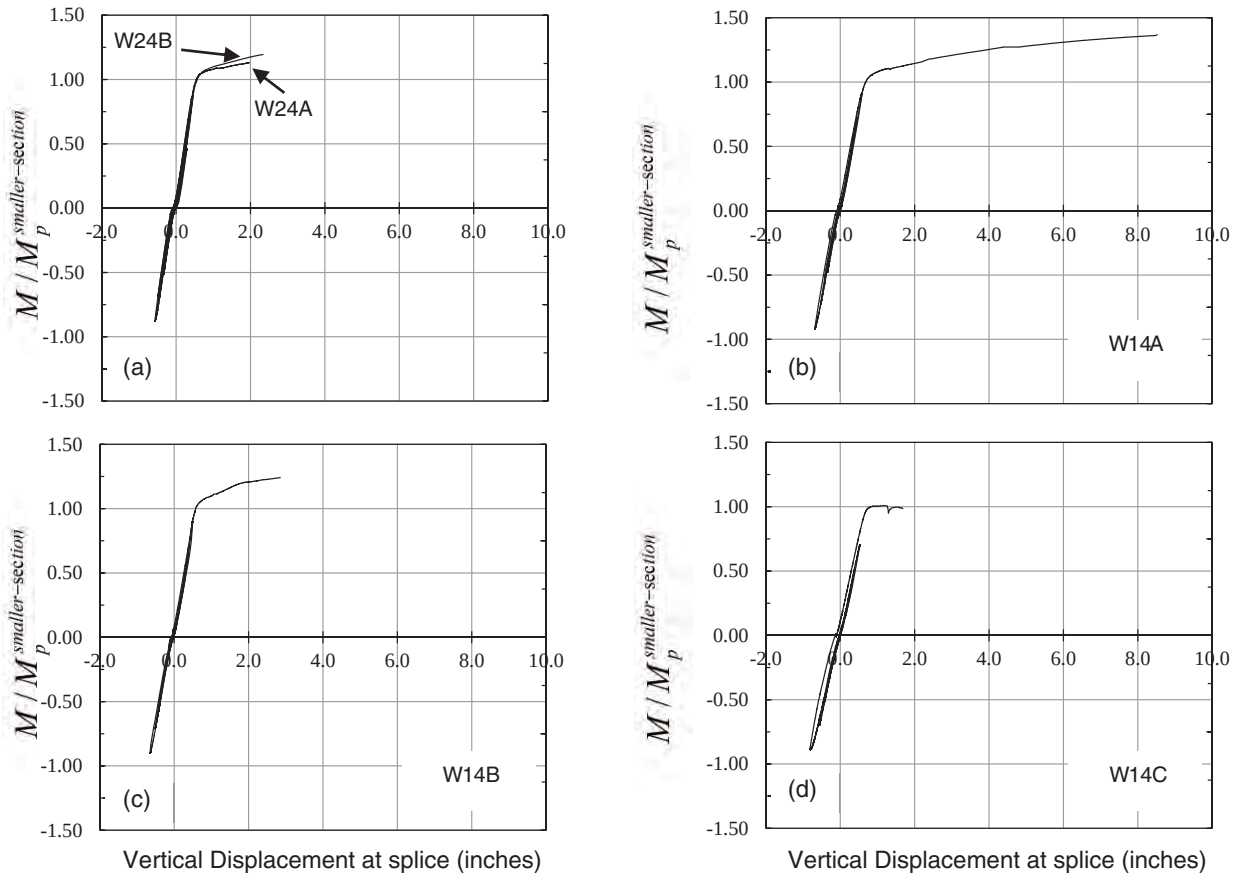

Fig. 6. Load displacement curves for full-scale tests: (a) W24A and B; (b) W14A; (c) W14B; (d) W14C.

summarized in Table 2. Other indicators of performance, such as the total deformation of the column provide a general, qualitative understanding of specimen response. The following discussion, which outlines the test data from each of these splices individually, is based on these results presented in Table 2 and Figure 6.

Response of Specimens 24A and 24B

Referring to Figure 6a, both these specimens exhibited virtually identical response. The initial cycles produced no observable signs of distress. However, during the cycles with amplitude $0.95M_p$, minor flaking of the mill scale was observed in the vicinity of the splice, indicating the onset of yielding. During the final, monotonic push, widespread yielding was observed in the splice region, as well as the surrounding areas, including in both the smaller and the larger column sections. The test was concluded when fracture was suddenly observed at a force corresponding to the development of the splice moment $M_{splice} = 1.13 \times M_p^{smaller-section}$ for specimen 24A and $M_{splice} = 1.19 \times M_p^{smaller-section}$ for specimen 24B. The fracture initiated at the tip of the UWR and the surface was coincident with the heat-affected zone (HAZ). Based on an inverse section analysis (using the measured stress-strain data from the materials), weld stress, σ_{flange}, at the instant of fracture was estimated to be approximately $1.32F_y^{flange}$, where $F_{y'}^{ange}$ is the measured yield stress of the particular section (Table 3). This suggests that the weld was fully yielded at the PJP section, and that the net section strength of this section was achieved. Also at this instant, the shear force in the splice, V_{splice}, was $0.85V_y^{smaller-section}$, where $V_y^{smaller-section} = 0.6F_yA_{web}^{smaller-section}$. The fracture completely severed the tension flange and propagated up through the PJP weld in the web, severing most of the web. Several bolts in the erection plate fractured as the crack propagated through the web weld. Figures 7a and 7b show photographs of both the tests taken after fracture.

Response of Specimen 14A

Similar to specimens 24A and 24B, the initial loading cycles produced no observable signs of distress in the specimen. However, during the cycles with amplitude $0.95M_p$, minor flaking of the mill scale was observed in the vicinity of the splice, indicating the onset of yielding. During the final push, large-scale yielding was observed in the splice, accompanied by widespread flaking of mill scale and the formation of visible slip bands. Figure 6b shows the load-deformation response, whereas Figure 7c shows a photograph of the specimen after the conclusion of the experiment. Referring to Figure 7c, fracture propagation was not observed for this experiment, which had to be concluded owing to safety concerns, wherein the applied load approached the capacity of the laboratory strong floor. Shown in Figure 7d is a closeup view of the unfused weld root. Small cracks (approximately 0.5 in. long) initiated at both tips. The degree of inelastic deformation in this specimen is striking. At the conclusion of the test, the estimated weld stresses, σ_{flange}, are approximately $1.34F_y^{flange}$. At this time, the moment in the splice, M_{splice}, was $1.37M_p^{smaller-splice}$, whereas the shear in the splice, V_{splice}, was equal to $0.93V_y^{smaller-section}$.

Response of Specimen 14B

Similar to the other specimens, the initial loading cycles produced no observable signs of distress in the specimen. During the final push, large-scale yielding was observed in the splice, accompanied by widespread flaking of mill scale and the formation of visible slip bands. Figure 6c shows the load-deformation curve, while Figure 7e shows a photograph of the specimen after the conclusion of the experiment. Qualitatively, the response of the specimen was similar to that of specimen 14A, except that fracture was observed during the final push, when the moment in the splice, M_{splice}, was $1.24M_p^{smaller-splice}$, whereas shear in the splice, V_{splice}, was $0.86V_y^{smaller-section}$. The estimated weld stresses, σ_{flange}, (based on strain gage data) are approximately $1.34F_y^{flange}$.

Response of Specimen 14C

Specimen 14C featured a bolted web plate, with no weld connection between the webs. Figures 6d and 7f show the load-deformation curve and post-test photograph, respectively. The response of this specimen was somewhat different than the other specimens, primarily in that yielding was observed at lower moments; in fact, some yielding was observed even in the cycles corresponding to $0.75M_p$. This may be attributed to the absence of full stress transfer through the web, in the tension region, such that development of full moment capacity is not theoretically possible. However, fracture was not observed until the final push—Figure 7f shows a post-test photograph. At the time of fracture, the moment in the splice, M_{splice}, was $1.04M_p^{smaller-section}$, whereas the shear in the splice, V_{splice}, was $0.72V_y^{smaller-section}$. Thus, even when judged relative to the entire loading protocol, the connection exhibited excellent performance. It is important to recall here that this detail, with the bolted web splice (and associated section sizes) is targeted toward low-rise structures, where the demands are quite low—refer, for example, to Table 1. When evaluated in this context, the response of the specimen is even more impressive. The strain rosette attached to the web splice plate recorded negligible shear strain. When combined with the observation that negligible shear deformation was noted in the flanges, this suggests that the shear was predominantly transferred through friction in the bearing portion of the sections, which provides the most rigid load path for the shear. This bearing zone develops as a result of the flexure in the cross-section. Two

points may be made based on this observation. First, adequate friction was likely generated even in the absence of net axial compression, which is typically present in low-rise buildings, wherein overturning moments are low. Second, unlike moment connections, in which the shear tab separates the web of the beam from the flange of the column, friction may be a reliable mechanism of shear transfer in column splices where the sections are in direct contact. In summary, it appears that other than the loss of some flexural capacity (due to the unavailability of the web in the tension region), the absence of a welded web splice does not compromise the effectiveness of the connection in any significant way.

Analysis and Discussion

The preceding sections provide specific discussion of individual specimen response. Based on this discussion, several general observations are now presented to evaluate the

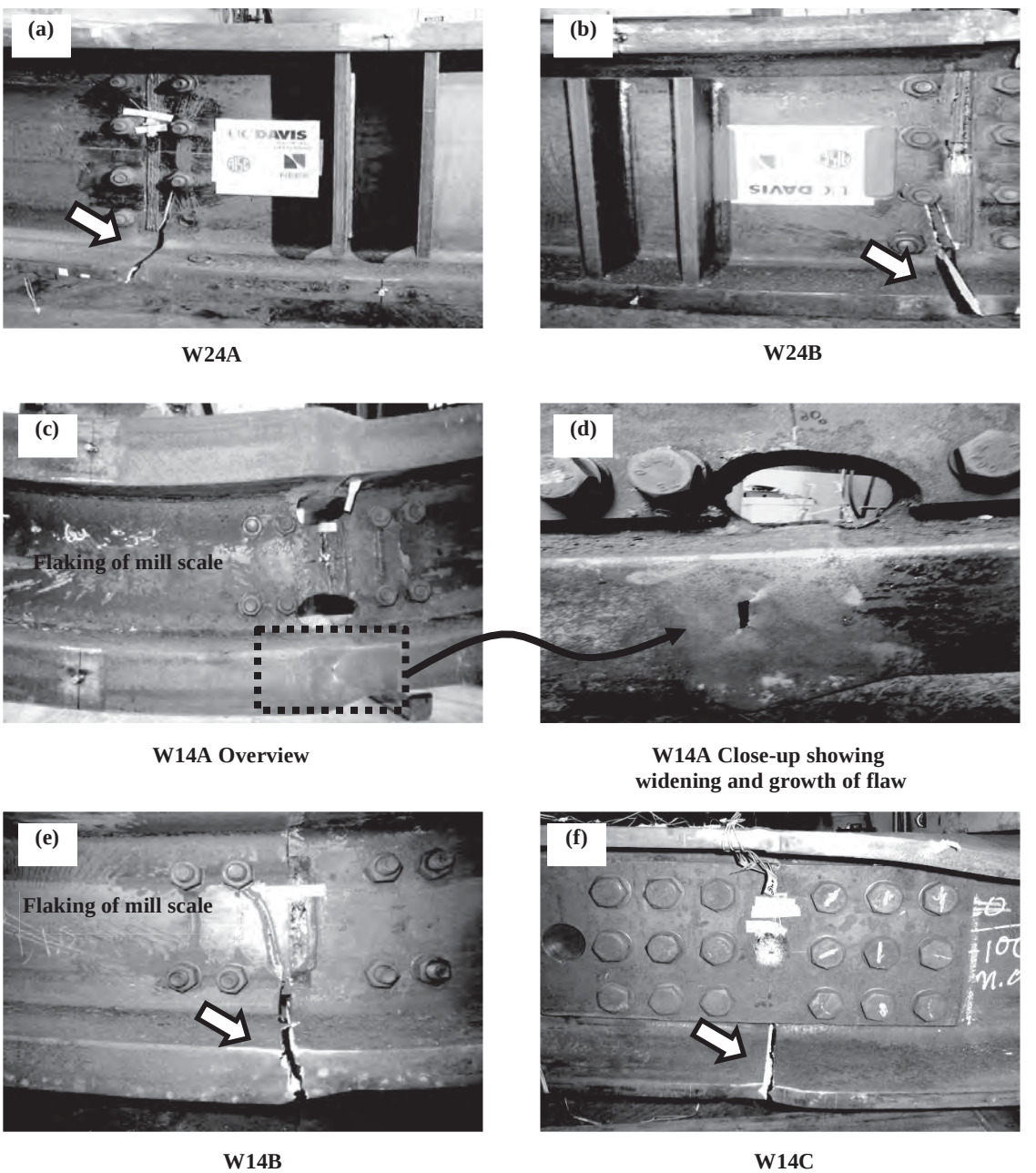

Fig. 7. Post-test photographs of all the specimens; block arrows indicate fracture.

suitability of these types of connections in IMRF and SMRF structures in highly seismic regions. The main observations are:

1. All specimens survived the cyclic portion of the protocol, and all (with the exception of specimen 14A) fractured on the final push. Recall that the protocol (if applied through completion) represents peak expected demands in 20-story buildings subjected to 2/50 ground motions. In this context, all the specimens (as tested in the lab) may be considered suitable candidates for application in such buildings.

2. In addition to exceeding the demands implied by the protocol, all the specimens also show significant inelastic deformation capacity. Referring to Table 2, the displacements (recorded at the midspan of the specimen) were several times yield displacement. Referring to previous discussion on demands, recall that column splices are mainly force-controlled components, with little expectation of inelastic action.

3. All the splice specimens were subjected to intense shear at the time of fracture. The shear demands in these splices were in the range of $0.72V_y^{smaller\text{-}section}$ to $0.93V_y^{smaller\text{-}section}$. This is significantly higher than may be expected in archetype buildings, wherein high moments at the splice location (which is typically near the center of the column) are accompanied by low shear because this type of response is associated with single curvature bending of the column associated with higher mode response. Recall that the test setup utilized by Bruneau and Mahin (1991) did not apply shear to the splices.

4. Two of the specimens featured somewhat innovative details: specimen 14B did not have a weld access hole, despite the presence of a weld on the inside of the web; and specimen 14C did not feature a welded web splice. Both these details exhibited excellent performance.

These observations indicate that the as-tested details are suitable for resisting seismic demands in moment frames. However, additional analysis needs to be conducted to generalize the test results to evaluate the possibility of their implementation in field details. For example, while the observed performance exceeded anticipated demands, the material toughness properties (specifically the weld properties, see Table 3) also exceeded the minimum required. Thus, extrapolation of the test results to field details (for which only minimum toughness may be relied upon, but which also will have reduced demands relative to the test splices) cannot be conducted without fracture mechanics analysis. The next section presents such an analysis.

FRACTURE MECHANICS ANALYSIS OF SPLICE CONNECTIONS

The primary purpose of the fracture mechanics simulations presented in this section is to provide support for generalization of the experimental findings. The following points define the scope and intent of the simulations—

1. The main objective of the simulations is to examine the fracture toughness demands (represented by a stress intensity factor K_I), and its relationship to applied stresses in the column flange. This relationship may be used to evaluate the suitability of current material toughness requirements for details similar to the ones tested in the study.

2. The simulations did not examine details distinct (in terms of shapes welded, extent of penetration or other features) from the ones tested in this study. This is because:

   a. In terms of configuration, it is anticipated that the test specimens represent key geometric aspects of PJP-welded splices, which may be considered for use in the future.

   b. The test splices are fairly large, and fracture mechanics results based on larger specimens are in general conservative when applied to geometrically similar details that are smaller (Anderson, 1995; Bažant, 1984). Thus while not precise, a simulation of the test specimens provides a reasonable basis for extrapolation to similar details that are physically smaller in size

   c. A full parametric study examining all possible types of splice details and sizes is prohibitively expensive.

Fracture mechanics simulations were conducted for the flange regions of four specimens: W14A, W24A and B (identical simulation, given that the specimens are nominally identical) and W14C. The specimen W14B was not simulated, because the termination of the internal weld would require 3D simulation. All simulations were conducted using the commercial platform ABAQUS (ABAQUS, 2012). Figure 8 schematically illustrates a finite element mesh for one such simulation (shown for the W24 specimen); the mesh for the W14C specimen is qualitatively similar. The mesh for W14A is somewhat different to accommodate the embedded crack with two crack tips (refer Shaw, 2013). Key features of the simulations are:

1. All the simulations modeled only the flange region of the splices, subjected to pure tension. This is based on the assumption that this loading state controls the fracture toughness demands at the UWR. As shown

in Figure 8, the models were 2D plane-strain models, because stress variations through the width of the flange are relatively modest and the plane strain approximation represents out of plane constraint in a conservative manner. This modeling approach has been previously adopted with good agreement with test data by Nuttayasakul (2000).

2. Each simulation featured approximately 20,000 plane-strain 8-node quadrilateral elements, although 114,000 were used for the W14A simulation due to the two crack tips. As indicated in the inset in Figure 8, the crack tip was greatly refined at the tip of the flaw, such that the smallest element size was on the order of 0.0005 in. The crack tip was modeled with a diameter of 0.001 in. (significantly lower than the anticipated critical crack tip opening displacement, *CTOD*c, for structural steels, which is typically on the order of 0.01 in.). This type of finite element mesh at the crack tip has been shown to adequately capture the stress gradients as well as the effects of crack tip blunting through the work of McMeeking and Parks (1979) and subsequently Kanvinde and Deierlein (2006).

3. Material constitutive properties were based on von Mises plasticity with isotropic hardening. For the base material, the properties were calibrated from the coupon tests described previously and summarized in Table 3. For the weld material, all-weld coupon data (for a similar type of weld) generated previously by Kanvinde et al. (2008) was used for calibration.

4. Loading was applied in the form of a stress traction on the smaller (top) flange as shown in Figure 8. The contour J-integral (Rice, 1968) was evaluated at each loading step. The J-integral is a well-established index for characterizing fracture toughness demands (and capacities) in steel component with small to moderate yielding. The ABAQUS platform provides functionality for calculation of the J-integral. For each loading step, the J-integral was calculated from approximately 40 contours around the crack tip to minimize numerical inconsistencies. The J-integral (J_I, where the subscript I denotes mode I, or crack opening) may be converted to an equivalent stress intensity factor K_I (which may be interpreted as toughness demand) as per the following relationship:

$$K_I = \sqrt{EJ_I \Big/ \left(1 - \nu^2\right)} \tag{1}$$

where E is the elastic modulus, ksi, and ν is Poisson's ratio.

Figures 9a, 9b and 9c illustrate the results of the W24, W14A and W14C simulations, respectively. To interpret these figures effectively, it is useful to consider relationships between the CVN energy (for which minimum values are required as per AISC 341-10) and the critical stress intensity factor K_{IC} (which is a measure of the fracture toughness capacity). One such relationship (based on statistical correlation) is provided by Barsom and Rolfe (1999). Equation 2 illustrates this relationship:

$$K_{IC}^{dynamic} = 0.001\sqrt{5000 \times CVN \times E} \tag{2}$$

In the previous equation *CVN* is the Charpy energy in ft-lb, E is the modulus of elasticity in ksi, and $K_{IC}^{dynamic}$ is the stress intensity factor (in ksi$\sqrt{\text{in.}}$ under dynamic loading rates (because it is derived from the CVN data which is obtained from high-rate dynamic tests). In contrast, loading rates in the tests described in this paper, or even in field

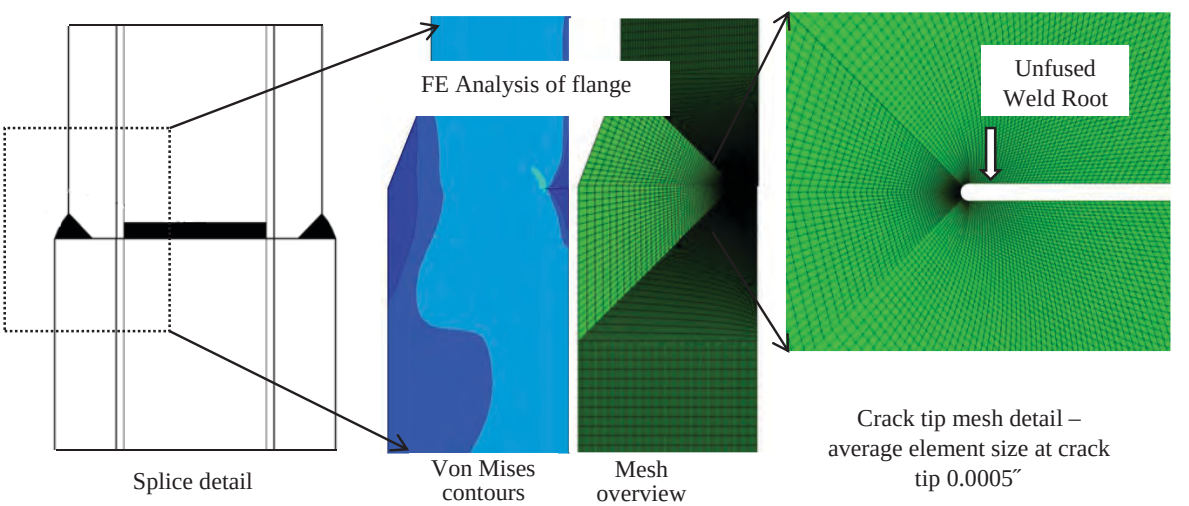

Fig. 8. Finite element simulation of splice flanges (W24 simulation shown as representative).

details subjected to earthquakes, may be considered "static," because they are several orders of magnitude lower than those observed in CVN tests (Barsom and Rolfe, 1999). In general, the $K_{IC}^{dynamic}$ is a lower bound on the available fracture toughness in seismic details. In each of the figures, the stress intensity factor K_I determined from the finite element simulations is plotted against the applied stress in the smaller flange. Because W14A has two crack tips, Figure 9b has two curves. However, these are almost coincident indicating that the fracture toughness demand at both crack tips is virtually identical.

A close inspection of Figures 9a through 9c provides the following insights:

1. For all the simulations, the K_I increases, as expected, monotonically with respect to the applied stress level. The points labeled *test performance* on the figures indicate the estimated longitudinal stress in the flange in each of the specimens at the time of fracture (based on an inverse sectional analysis outlined earlier). Referring to these labels on the figure, these stresses are in 65- to 75-ksi range. At these stresses, K_I is in the range of 150 to 200 ksi$\sqrt{\text{in.}}$, implying it to be the available fracture toughness at the crack tips in the full-scale specimens. For comparison, if the CVN values from the PQR assembly (52 ft-lb) or the post-test weld from the W14B specimen (50 ft-lb) are converted to equivalent $K_{IC}^{dynamic}$ values per Equation 2, then $K_{IC}^{dynamic} \approx 85$ ksi$\sqrt{\text{in.}}$ The difference—the significantly higher implied toughness in the splice simulations as compared to $K_{IC}^{dynamic} \approx 85$ ksi$\sqrt{\text{in.}}$ determined previously—is not entirely surprising because both of the PQR tests as well as the W14B CVN tests are dynamic, such that 85 ksi$\sqrt{\text{in.}}$ is a lower bound on the available toughness; and the PQR tests were conducted at a lower temperature (0 °F), which is lower than the temperature at which the full-scale tests (approximately 60 °F) were conducted. In fact, the value $K_I \approx 150$ to 200 ksi$\sqrt{\text{in.}}$ is in the range of fracture toughness values for similar weld materials tested using static (rather than dynamic) fracture mechanics tests (Kanvinde et al., 2008).

2. In each of the Figures 9a through 9c, the marker *peak demands* indicates the maximum anticipated stress in the splice flange based on the nonlinear time history simulations described earlier. This is equal to the expected yield stress, approximately 55 ksi. Based on the intersection of this marker with the curves in Figures 9a through 9c, the toughness demands at this value of flange stress are 45 ksi$\sqrt{\text{in.}}$, 26 ksi$\sqrt{\text{in.}}$ and 27 ksi$\sqrt{\text{in.}}$ for W24, W14A and W14C, respectively. Also shown in the figures is the horizontal line labeled *minimum expected toughness*. This value, *K*IC = 54 ksi$\sqrt{\text{in.}}$, is obtained by substituting CVN = 20 ft-lb into Equation 2. The value of 20 ft-lb may be considered a suitable lower bound for material toughness because, for the weld filler metal, a value of 20 ft-lb at 0 °F is required; and for heavy sections (base metal), a CVN value 20 ft-lb at 70 °F in the core of the section is required; toughness elsewhere will likely be higher. As a result, $K_{IC} = 54$ ksi$\sqrt{\text{in.}}$ is a reasonable lower bound on the expected toughness in a demand critical weld, such as the PJP welds in splices. Relative to this value, the demands are lower (see Figure 9), suggesting that the splice details tested in this study are suitable for field use even if a low estimate of material toughness is considered. A possible exception to this is in the case of buildings where the column splices may be exposed to low temperatures (50 °F and lower), because the base metal toughness requirement (20 ft-lb) is applicable at 70 °F. AISC 341-10 requires that "the minimum qualification temperature for AWS D1.8/D1.8M Annex A be adjusted such that the test

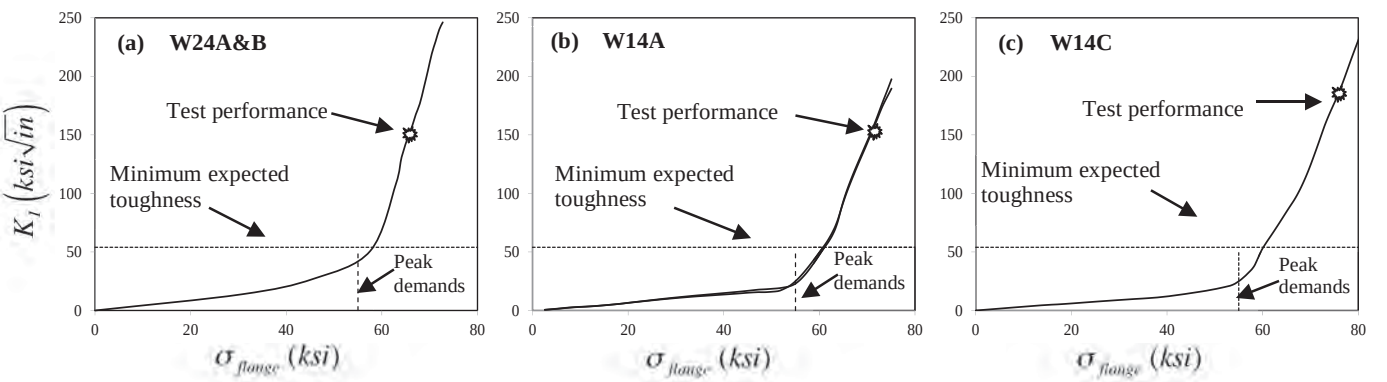

Fig. 9. Results of finite element simulations for (a) W24 specimens; (b) W14A; and (c) W14C.

temperature for the Charpy V-notch toughness qualification tests be no more than 20 °F (11 °C) above the lowest anticipated service temperature (LAST)."

In summary, the finite element simulations provide quantitative insight into the relationships between fracture toughness demands and applied stresses. For the connection details tested in this study, it is apparent that the toughness demands are lower as compared to the minimum available toughness capacity. This provides a suitable basis for generalizing the test results to connections that are geometrically similar to (and smaller than) the ones tested in this study. The next section summarizes the study along with its findings, implications, and limitations.

SUMMARY AND CONCLUSIONS

AISC 341-10 requires the use of complete-joint-penetration (CJP) groove welds for column splices in intermediate and special moment frames in seismic design. These requirements are a result of research following the Northridge Earthquake on welded beam-column connections (SAC, 1996) that demonstrated the detrimental effect of embedded flaws (such as those produced at PJP welds) on the response of welded joints. However, more recent research (Myers et al., 2009; Gomez et al., 2010; and Dubina and Stratan, 2002) indicates that when high-toughness materials are used (as also mandated by post-Northridge design standards), then excellent performance may be obtained even if a flaw is present. Motivated by this research, the main objective of the current study is to examine the feasibility of PJP-welded column splices for steel moment frame construction in seismic regions.

The main scientific component of this study is a series of five full-scale column splice tests. The full-scale tests are supported by a comprehensive program of nonlinear time history simulation as well as ancillary material tests. The objective of the simulations is to quantitatively establish force and moment demands in the splices, ultimately leading to the development of a loading protocol for the full-scale experiments. The ancillary tests enable the interpretation of full-scale test data with respect to measured, rather than specified, material properties. The program of testing is also complemented by finite element simulations that employ fracture mechanics to develop support for the generalization of test results.

The full-scale test matrix includes a range of column sizes and details. The key variables interrogated in the test matrix include:

1. Column size, such that the tested specimens included sections from W14×132 to W14×730 with approximately 5-in.-thick flanges, as well as two specimens featuring W24 sections. The sizes represent commonly used sections for 4- to 20-story buildings.
2. Weld details, including single-bevel (W14C, W24A and B), and double-bevel specimens with (W14A) and without (W14B) a weld-access hole.
3. The absence of a welded web on one of the specimens (W14C) to examine the feasibility of bolted web connections for low-rise construction where the demands are modest.

The specimens were all subjected to reversed cyclic loading as per a loading protocol based on the nonlinear time history simulations. The load was applied in a three-point bend configuration such that the splice was subjected to a combination of flexure and shear. All the specimens exhibited excellent performance, surviving the entire loading protocol. Four out of the five specimens fractured in the tension flange of the splice during the final monotonic push after completion of the protocol. One specimen, W14A, did not fracture before machine capacity was reached, requiring the termination of the test. All specimens showed a high degree of inelastic deformation prior to fracture with yielding in both the larger and smaller column. Given that inelastic action is not expected in column splices (based on design intent as well as simulation), this performance is especially impressive. The peak moment sustained by the splices was in the range of $1.04M_p^{smaller\text{-}section}$ for the bolted web, and the W14C specimen was $1.37M_p^{smaller\text{-}section}$ for the W14A specimen, indicating that these splices developed the strength of the smaller connected column. The shear in these splices ranged from $0.72V_y^{smaller\text{-}section}$ to $0.93V_y^{smaller\text{-}section}$; these combinations of high moment and shear are highly unlikely in an archetype frame.

A series of fracture mechanics simulations was conducted to develop support for the generalization of test results. The main objective of the finite element simulations was to examine the relationship between the fracture toughness demand (represented by the stress intensity factor K_I, and the applied stress in the flange). The simulations indicated that for the tested connections, the toughness demands are below the minimum expected toughness (considering the requirements of AISC 341-10). This suggests that details similar to the ones tested in the study may be suitable for general use in the field. While the results of the study are encouraging from the perspective of adoption of PJP splices in IMRFs and SMRFs, the study has several limitations that must be considered when interpreting the results:

1. While the experiments incorporated a range of details and member sizes, field details that are significantly dissimilar to the tested specimens may have higher toughness demands, and thus be more fracture critical. Examples of these situations include details where the extent of weld penetration or effective throat thickness is smaller (and the UWR is larger) than in the tests and details where flanges of similar thickness

are connected, where the reinforcement provided by the flared shape of the weld is absent (in contrast to the unequal flange connection where significant reinforcement is present due to the shape of the weld transition; see Figure 5). An accurate assessment of these factors is possible only through additional testing or a comprehensive parametric study using finite element simulations similar to the ones described in this paper.

2. A rigorous reliability analysis to determine capacity factors (ϕ factors) for design of these connections has not been conducted, neither has a strength characterization approach been developed. These are subjects of ongoing study. However, based on the performance of these details, and the insights provided by the finite element simulations, a possible route for implementation of this research is the prescriptive use of details similar to the ones tested.

3. The toughness estimate used in the fracture mechanics analysis (20 ft-lb) may not be conservative for columns that are exposed to low temperatures (50 °F and lower), because the base metal (in the core of heavy sections) toughness is required at 70 °F. AISC 341-10 requires that toughness qualification tests be no more than 20 °F above the lowest anticipated service temperature. It is also pertinent to mention here that the 20 ft-lb at 70 °F toughness (in the core) is not required when the column flanges are thinner than 1½ in., because adequate toughness is expected from these. Consequently, while it is highly likely that the results of this study are applicable to these situations (test 14C supports this), it is noted that the 20 ft-lb toughness is not explicitly required by the AISC 341-10 for these situations.

4. Residual stresses in welds, as well as in-situ weld toughness are sensitive to parameters of the welding procedures as well as physical constraints at the time of welding (Masubuchi, 1980). This should be considered as a factor in the generalization/implementation of results.

5. The demand analysis (the nonlinear time history simulations) is based on a small set of archetype buildings subjected to a limited number of ground motions. While the results of this analysis are applied in a conservative manner, aspects of structural response not considered by the simulation (e.g., buildings taller than 20 stories, near fault ground motions and vertical accelerations) may influence demands in the splices. Similarly, the effect of the use of high-strength steel for columns on splice demands is also undetermined. As discussed previously, columns with Grade 50 material ($F_y = 50$ ksi) were used along with E70 welds. However, given that the columns in the nonlinear time history simulations showed very limited (or no) yielding, it may be argued that the strength of the columns may not affect demands in the splices.

6. Because the nonlinear time history simulations are based on planar frames, three-dimensional effects (due to bidirectional shaking) are not explicitly incorporated in this study. However, the effects of this are anticipated to be modest. Moreover, it is important to recall that the simulations only featured special moment resisting frames and not intermediate moment frames (IMFs), which are not subject to the SCWB requirement. Thus, it may be argued that the results are not applicable to IMFs wherein the splice force/moment demands may be larger. However, two points may be made in response. First, even in the SMRFs (considered in this study), which have the SCWB requirement, the column end interaction ratio approached yield for the 20-story frame. Second, IMFs are limited to a 35-ft height restriction in seismic design category D. The nonlinear time history results for the 4-story SMRF (which is similar in height to this limit) suggest that the response in these cases is dominated by first mode response with low demands at the splice. It is not unrealistic to extrapolate this response to IMFs.

7. While the effects of these factors have not been determined, in some ways, the results of the study may also be conservative with respect to field conditions. For example, the test specimens required flipping for the application of reversed cyclic loading. Each of these flips required approximately 1 to 2 hr to execute, introducing the possibility of strain aging and associated detrimental effects on splice performance. These effects are not present in field splices, which are subject to a higher rate of loading.

Thus, while the results of this study are promising from a standpoint of utilizing PJP-welded splices in seismic moment frames, some of the issues previously discussed need to be considered in adopting these findings in standards. While it may not be feasible to conduct additional full-scale testing, focused parametric simulation through FE simulation may greatly aid the generalization and implementation of these results.

ACKNOWLEDGMENTS

This project was funded by the American Institute of Steel Construction (AISC). Herrick Steel of Stockton, California, and Gayle Manufacturing Company of Woodland, California, generously donated and fabricated steel materials for this research, and their donations are gratefully acknowledged.

California Erectors of Benicia, California, donated its time toward welding of the specimens. The authors also thank Tom Schlafly of AISC, Bob Hazelton of Herrick Steel, and Gary Glenn of Gayle Manufacturing in addition to the AISC research committee, specifically James Malley and John Barsom, for providing oversight and direction to the testing plans and interpretation of results. The large-scale experiments described in this report were conducted at the Network for Earthquake Engineering Simulation (NEES) equipment site at the University of California at Berkeley in Richmond, California. The authors would also acknowledge the NEES and William Vuong, undergraduate researcher from the University of California at Davis, for assisting with the testing. The findings and opinions of this paper are those of the authors and do not necessarily represent those of the major sponsor, AISC.

SYMBOLS

$CTOD_c$	Critical crack tip opening displacement.
E	Modulus of elasticity of steel, 29,000 ksi.
F_y	Specified yield stress.
F_y^{flange}	Measured yield stress of smaller column flange.
IR	Interaction ratio of column section, defined as $IR = \frac{P}{P_y} + \frac{8}{9}\frac{M}{M_p}$ for $\frac{P}{P_y} \geq 0.2$ $IR = \frac{P}{2P_y} + \frac{M}{M_p}$ for $\frac{P}{P_y} < 0.2$ where P_y and M_p are the axial force capacity and plastic moment capacities, respectively, of the smaller column. P and M are force and moment, respectively, at the splice.
IR_{peak}^{median}, $IR_{peak}^{\max}$	The median and maximum (over 20 ground motions) values of the peak interaction ratio (peak within each time history).
J_I	J-integral for mode I.
K_I, K_{IC}	Stress intensity factor demand, capacity.
M_{splice}	Applied moment at the splice.
$M_p^{smaller-section}$	Plastic moment capacity of the smaller cross section such that $M_p^{smaller-section} = R_y F_y Z_x$, where R_y is the ratio of the estimated to specified yield strength, and Z_x is the plastic section modulus of the smaller section.
$M_{splice}^{\max}$	Maximum moment observed in the splice during experiment.
$V_{splice}^{\max}$	Maximum shear observed in the splice during experiment.
$V_y^{smaller-section}$	Shear strength of the smaller cross-section, equal to $0.6F_y A_{web}^{smaller-section}$.
Δ_{peak}^{median}, $\Delta_{peak}^{\max}$	The median and maximum (over 20 ground motions) values of the peak interstory drift (peak within each time history).
ν	Poisson's ratio, 0.3.
σ_{flange}	Estimated stress in the tension flange based on section analysis.

REFERENCES

ABAQUS (2012), *User's Manual*, Hibbitt, Karlsson, and Sorensen, Inc., Providence, RI.

AISC (2010), *Seismic Provisions for Structural Steel Buildings*, AISC 341-10, American Institute of Steel Construction, Chicago, IL.

AISC (2011), *Steel Construction Manual*, 14th Ed., American Institute of Steel Construction, Chicago, IL.

Anderson, T.L. (1995), *Fracture Mechanics*, 2nd Ed., CRC Press, Boca Raton, FL.

ASCE (2010), *Minimum Design Loads for Buildings and Other Structures*, ASCE 7, American Society of Civil Engineers, Reston, VA.

AWS (2004), *Structural Welding Code—Steel,* AWS D1.1/D1.1M: 2004, American Welding Society, Miami, FL.

AWS (2009), *Structural Welding Code—Seismic Supplement*, AWS D1.8/D1.8M: 2009, American Welding Society, Miami, FL.

Barsom, J.M. and Rolfe, S.T. (1999), *Fracture and Fatigue Control in Structures*, 3rd ed., Butterworth-Heinemann, Waltham, MA.

Bažant, Z.P. (1984), "Size Effect in Blunt Fracture: Concrete, Rock, Metal," *Journal of Engineering Mechanics,* ASCE, Vol. 110, No. 4, pp. 518–535.

Bruneau, M. and Mahin, S., (1991), "Full-scale tests of Butt-Welded Splices in Heavy-Rolled Steel Sections Subjected to Primary Tensile Stresses," *Engineering Journal*, AISC, First Quarter, pp. 1–17.

Dubina, D. and Stratan, A. (2002), "Behaviour of Welded Connections of Moment Resisting Frames Beam-to-Column Joints," *Engineering Structures,* Elsevier, Vol. 24, No. 11, pp. 1431–1440.

Engelhardt, M.D. and Sabol, T.A. (1994), "Testing of Welded Steel Moment Connections in Response to the Northridge Earthquake," Research Progress Report, Northridge Steel Update I, American Institute of Steel Construction, Chicago, IL.

Fell, B.V., Kanvinde, A.M., Deierlein, G.G. and Myers, A.T. (2009), "Experimental Investigation of Inelastic Cyclic Buckling and Fracture of Steel Braces," *Journal of Structural Engineering,* ASCE, Vol. 135, No. 1, pp. 19–32.

FEMA (2000), *Recommended Design Criteria for New Steel Moment-Frame Building*s, FEMA 350, Federal Emergency Management Agency, Washington, DC.

Gomez, I.R., Kanvinde, A.M. and Deierlein, G.G. (2010), "Exposed Column Base Connections Subjected to Axial Compression and Flexure," Report Submitted to the American Institute of Steel Construction, Chicago, IL.

Gupta, A. and Krawinkler, H. (1999), "Seismic Demands for Performance Evaluation of Steel Moment Resisting Frame Structures, (SAC Task 5.4.3), Report No. 132, John A. Blume Earthquake Engineering Center, Stanford University, Stanford, CA.

Hayes, J.M. (1957), "Effects of Initial Eccentricities on Column Performance and Capacity," *Journal of the Structural Division*, American Society of Civil Engineers, Paper 1440.

Kanvinde A.M. and Deierlein G.G. (2006), "The Void Growth Model and the Stress Modified Critical Strain Model to Predict Ductile Fracture in Structural Steels" *Journal of Structural Engineering,* ASCE, Vol. 132, No. 12, pp. 1907–1918.

Kanvinde A.M., Fell B.V., Gomez I.R. and Roberts M. (2008), "Predicting Fracture in Structural Fillet Welds Using Traditional and Micromechanics-Based Models," *Engineering Structures,* Elsevier, Vol. 30, No. 11, pp. 3325–3335.

Kaufman, E. and Fisher, J. (1995), "A Study of the Effects of Materials and Welding Factors on Moment Frame Weld Joint Performance Using a Small-scale Tension Specimen," *Technical Report 95-08*, SAC Joint Venture, Sacramento, CA, December.

Kaufmann, E.J., Metrovich, B.R., and Pense, A.W. (2001), "Characterization of Cyclic Inelastic Strain Behavior on Properties of A572 Gr. 50 and A913 Gr. 50 Rolled Sections," Final Report to American Institute of Steel Construction, ATLSS Report 01-13, Lehigh University, Bethlehem, PA.

Lignos, D.G., Krawinkler, H. and Whittaker, A. S. (2011), "Prediction and Validation of Sidesway Collapse of Two Scale Models of a 4-Story Steel Moment Frame," *Earthquake Engineering and Structural Dynamics,* Vol. 40, No. 7, pp. 807–825.

Masubuchi, K., (1980), *Analysis of Welded Structures*, Pergamon Press, Elmsford, NY.

Matsuishi, M. and Endo, T. (1968), *Fatigue of Metals Subjected to Varying Stress*, Japan Society of Mechanical Engineering, Tokyo, Japan.

McMeeking, R.M. and Parks, D.M. (1979), "On Criteria for J-Dominance of Crack-Tip Fields in Large Scale Yielding," *Elastic-Plastic Fracture*, ASTM STP 668, J.D. Landes, J.A. Begley and G.A. Clarke, Eds., American Society for Testing and Materials, West Conshohocken, PA, pp. 175–194.

Myers, A.T., Kanvinde, A.M., Deierlein, G.G. and Fell, B.V. (2009), "Effect of Weld Details on the Ductility of Steel Column Baseplate Connections," *Journal of Constructional Steel Research*, Elsevier, Vol. 65, No. 6, pp. 1366–1373.

Nuttaysakul, N. (2000), "Finite Element Fracture Mechanics Study of Partial Penetration Welded Splices," Master's Thesis, Stanford University, Stanford, CA.

OpenSEES (2009), "Open System for Earthquake Engineering Simulation," Pacific Earthquake Engineering Center, Berkeley, CA.

Popov, E.P. and Stephen, R.M. (1976), "Capacity of Columns with Splice Imperfections," *Engineering Journal,* American Institute of Steel Construction, First Quarter, pp. 16–23.

Rice, J.R. (1968), "A Path-Independent Integral and the Approximate Analysis of Strain Concentration for Notches and Cracks." *Journal of Applied Mechanics*, Vol. 35, pp. 379–386.

Richards, P.W. and Uang, C-M. (2006), "Testing Protocol for Short Links in Eccentrically Braced Frames," *Journal of Structural Engineering*, ASCE, Vol. 132, No. 8, pp. 1183–1191.

SAC Joint Venture (1996), "Selected Results from the SAC Phase 1 Beam-Column Connection Pre-Test Analyses," Technical Report 96-01, Sacramento, CA.

Shen, J, Sabol, T., Akabas, B. and Sutchiewcharn, C. (2010), "Seismic Demand of Column Splices in Special Moment Frames," *Engineering Journal,* AISC, Fourth Quarter, pp. 223–240.

Shaw, S.M., (2013), "Seismic Performance of Partial Joint Penetration Welds in Special Moment Resisting Frames," Ph.D. Dissertation, University of California, Davis, CA.

Somerville, P., Smith, N., Punyamurthula, S. and Sun, J. (1997), "Development of Ground Motion Time Histories for Phase 2 of the FEMA/SAC Steel Project," SAC Background Document, Report No. SAC/BD-97/04.

Effect of Link-Beam Stiffener and Brace Flange Alignment on Inelastic Cyclic Behavior of Eccentrically Braced Frames

REZA IMANI and MICHEL BRUNEAU

ABSTRACT

Finite element analysis was used to investigate the effects of the misalignment of the brace flange-to-beam connection point with the link-end stiffener (referred to as the offset in the paper) on the ductility of eccentrically braced frames (EBF). The offset was speculated to be a possible reason for the unexpected EBF failures observed in the aftermath of the Christchurch earthquake series of 2010 and 2011. EBF models with different detailing at the offset area were analyzed under monotonic and cyclic displacements. Results showed severe stress and strain concentration in the offset area, preventing the EBF from developing its expected ductility, and suggested possible initiation of a failure from the part of link flange located in the offset area. Simulation using the ductile fracture model implemented in ABAQUS resulted in a fracture pattern in agreement with the actual failed EBF. Results from analyses on different detail configurations showed that removal of the offset by modifying the brace section to build an ideal case, or by a simple change in the location of the link stiffener, can mitigate the problem of possible premature failure, with the latter solution being slightly less effective but much easier to be used in practice.

Keywords: Eccentrically braced frames, EBF failure, eccentricity, offset at brace flange-to-beam connection.

INTRODUCTION

Previous analytical and experimental research has demonstrated that properly designed eccentrically braced frame (EBF) systems can provide the ductility and energy dissipation capacity needed to serve as an effective lateral load resisting system to resist earthquake demands (e.g., Roeder and Popov, 1978; Merovich et al., 1982; Hjelmstad and Popov, 1983; Malley and Popov, 1984; Kasai and Popov, 1986a, 1986b, 1986c; Ricles and Popov, 1987a, 1987b; Popov et al., 1987; Engelhardt and Popov, 1989a, 1989b). The EBF design requirements of the AISC *Seismic Provisions* (AISC, 2010b) are intended to concentrate the large inelastic deformations in EBFs subjected to seismic loading primarily into specially detailed ductile links. This will lead to cyclic yielding and energy dissipation in the link while all of the other members remain essentially elastic (AISC, 2010b).

While a number of EBF systems have been constructed around the world, EBFs were tested under an actual severe seismic event for the first time during the Christchurch earthquake series of 2010 and 2011. Reports from the aftermath of these events showed a relatively better performance for steel structures compared to other structural systems (Bruneau et al., 2010; Clifton et al., 2011). The EBF systems that had been used in a few buildings in Christchurch generally exhibited a satisfactory behavior under the relatively intense shakings that occurred in the two largest earthquakes recorded during the 2010 and 2011 events. For instance, two multi-story buildings in the Christchurch central business district, which had EBFs as part of their lateral load resisting system, were green tagged and occupied after the earthquake series (Clifton et al., 2011), even though a life safety performance would be acceptable in seismic action of that intensity. However, some unexpected EBF link failures occurred during the 2011 event, including two in the EBF systems used in a parking garage in Christchurch's central business district. Those links typically exhibited a large fracture that had initiated in the link flange and progressed into the beam outside the link (Clifton et al., 2011).

Although the fracture, shown in Figure 1a, didn't jeopardize the overall performance of the building and the structure survived on account of the redundancy of the system (at least 6 EBF frames existed at the story where the link failure was observed), it remains that this is an undesirable behavior that has raised questions regarding the design and detailing of EBF systems to ensure development of their expected capacity and ductility. Clifton et al. (2011) speculated that this failure was possibly caused by a local stress concentration due to an offset between the brace flange-to-beam connection point and the link end-stiffener. The AISC *Seismic Provisions* require the use of full depth stiffeners at both

Reza Imani, Graduate Research Assistant, Department of CSEE, University at Buffalo, Amherst, NY (corresponding author). Email: rezaiman@buffalo.edu

Michel Bruneau, Professor, Department of CSEE, University at Buffalo, Amherst, NY. E-mail: bruneau@buffalo.edu

ends of all links to ensure the proper transfer of link shear forces to the reacting elements.

This paper reports the findings of a limited study conducted to investigate whether this eccentricity could have been the cause of the observed failures. Finite element analyses were used to investigate the cyclic inelastic behavior of EBF systems having different connection eccentricity details to identify the possible impact of such eccentricities, and recommend desirable configurations.

THE PROBLEMATIC CONNECTION DETAIL AND PROPOSED ALTERNATIVES

A closer look at the details of the connection in Figure 1a reveals that the brace flange was connected to the beam with an offset from the edge of the link stiffener. As indicated above, it was speculated that this eccentricity might have caused stress concentrations in that location, leading to a premature fracture in the beam flange in the offset area between the link stiffener and the brace flange, which then continued into the web of the beam outside the link. However, there were other EBF frames in the same building, which did not have the mentioned offset in the brace-to-beam connection and that showed a significant amount of yielding in the link without any fractures. Figure 1b shows one such link located in an upper story of the same structure, in which the link stiffener and the brace flange were vertically aligned.

Note that, according to a recent study on the two fractured EBFs by Marshall (2013), drawings of the details for the EBFs used in the parking garage showed a vertical alignment between the link stiffener and brace flange, while the intersection of the beam and brace centerlines was located inside the link. The main reason for the occurrence of misalignment for some the EBFs in that building remains unknown to the authors. Because no fractures were seen in the other EBFs of the same building that had braces with flange connecting to the beams at a point more aligned with the link stiffener, circumstantial evidence seemed to support the conclusions of Clifton et al. (2011). However, quantifiable verification is desirable to more tangibly establish whether or not this issue was the possible cause of the observed fractures.

The reported EBF fractures were studied in a forensic examination by Kanvinde et al. (2012). Material samples were extracted from the fractured structures and subjected to Charpy-V notch toughness tests and tensile tests, to establish if potential deficiencies in material properties could explain the observed fractures. The material test results revealed satisfactory ductile behavior for the extracted coupons. A few finite element analyses on EBF models with detailing similar to the fractured structures were also conducted, showing stress concentrations at the eccentricity between the link stiffener and the brace flange.

The work reported here expands on the prior work by assessing the effect of brace flange alignment and work-line eccentricity on behavior of the connection. Four detail geometries, shown in Figure 2, were arbitrarily selected in this study and investigated using finite element analysis when subjected to monotonic and cyclic displacements.

Case EBF-1 is similar to the configuration used in the reported fractured EBFs, in that the stiffener is placed at the intersection of the brace and beam centerlines but doesn't vertically line up with the edge of the brace flange. This

(a) *(b)*

Fig. 1. Photos of EBFs taken inside a parking garage following the Christchurch earthquake of 2011 (Clifton et al., 2011): (a) fractured EBF (lower level); (b) evidence of plastic action without fracture (top level).

geometry is selected as a generic case of an EBF with a wide flange brace directly welded to the beam, with the specific misalignment conditions mentioned above, and does not represent the exact geometry of the EBFs fractured in Christchurch. Analysis of one of those actual fractured EBF links, based on as-built dimensions, is presented in the last section of this paper.

The piece of the beam's bottom flange that is located between the link end-stiffener and the point where the flange of the brace is welded to the beam is referred to as the offset area from this point on in this report. Case EBF-2 represents the ideal configuration in which the stiffener is at the intersection of the beam and brace centerlines and the brace flange connects to the beam under the vertical stiffener (achieved by using a deeper brace member than the one in the previous case). The third case, EBF-3, is similar to EBF-1, except that the link end-stiffener has been moved to align vertically with the point where the flange of the brace is welded to the beam (as a consequence, the work-line of the brace intersects that of the beam inside the link, which is described as permitted in the Commentary to AISC 341-10. The last case, EBF-4, combines the misalignment of case EBF-1 with the situation where the work-lines of the beam and brace intersect outside the link; this last case, while not permitted by the 2005 AISC *Seismic Provisions* (AISC 341-05) was accepted into the 2010 version (AISC 341-10) with the condition that the beam outside the link must be designed for the subsequent additional moments (AISC, 2005; 2010b). This case is investigated out of curiosity, to determine if the effect of brace flange misalignment is compounded when the stiffener is not at the intersection of the brace and beam centerlines.

Two types of finite element analyses were conducted in this study. A first set of analyses examined the effects of the eccentricities mentioned above on the stress-strain distribution and deformations in the link and the elements close to the intersection of the brace and the beam. For the case where results showed critical stress and strain concentration, a second type of analysis was conducted to simulate the possible consequent path of fractures to compare with those occurred following the Christchurch earthquake.

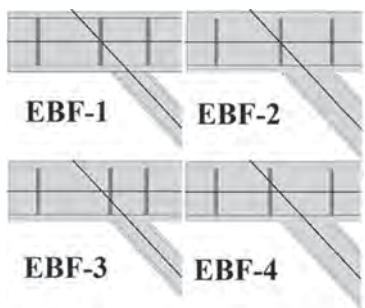

Fig. 2. Detailing alternatives for brace-to-beam connection.

FINITE ELEMENT MODELING

The general finite element software ABAQUS was used to study the behavior of EBF systems designed with different brace-to-beam connection details under monotonic and cyclic loading. Four models were built according to the design alternatives described above using approximately 100,000 linear 8-node 3D brick elements with reduced integration (i.e., element type C3D8R). Initial design parameters of the beam, column and brace were taken from a past experimental study on EBF frames (Berman and Bruneau, 2008) and were slightly modified to match the four cases mentioned above. All of the sections were modeled as wide-flange beams to resemble the conditions of the frame which fractured in the Christchurch earthquakes. Meshing strategy started with a uniform pattern for the whole model and was refined at the critical locations, after some preliminary analyses, to achieve more reliable results. Due to anti-symmetric condition of the system, only half of each frame was modeled with its corresponding connection detail.

A simple bilinear steel material with von Mises yield criteria was used for the beam, including the link. The material was defined with a uniaxial behavior that started with a linear elastic part with Young's modulus of 200,000 MPa (29,000 ksi) and yield stress of 350 MPa (50 ksi) at the strain value of 0.2%. The post-yield segment consisted of a linear strain hardening branch that continued up to the strength of 444.5 MPa (65 ksi) at the strain value of 15%. This resulted in a strain hardening slope equal to 3% of the initial stiffness. The column and the brace were set to remain elastic in all of the models throughout the analysis, because they were not expected to yield, and to accelerate execution time. Note that this assumption was validated by looking at the 3D state of stress in the column and brace members, which showed that their maximum von Mises stress values remained below the yield limit (these values were less than 50% of the yield in most of the cases).

Considering that no damage criteria were added to the model at this stage to simulate the behavior of the material from the point of maximum strength toward fracture, the uniaxial behavior of the steel material was defined to linearly lose its strength (from maximum to a value close to zero) over the strain range of 15% to 20%, while the latter was assumed to be the fracture strain. This configuration made it possible for the analysis to provide realistic results in terms of the strength of the frames, particularly at certain points throughout the analysis when a portion of element in the beam or the link had to go through severe plastic strains. The strain of 15%, which is corresponding to the von Mises stress value of 444.5 MPa, was defined as the limit beyond which the strength of the element starts to decline (onset of strength reduction), gradually making it ineffective in the overall behavior of the model. All four models were built with identical columns and beams, but with the

slight differences in stiffener positions and brace sections to implement the different connection details described earlier (Figure 2). Figure 3 shows two views of a typical built model.

The base of the column was modeled as a simply supported end as column deformations were not relevant for the plastic mechanisms studied. The nodes at the left of the beam were constrained to comply with the anti-symmetric boundary conditions (same horizontal translation and no vertical translation at the plane of symmetry). All of the members were modeled using the 8-node 3D solid elements. Monotonic or cyclic displacements were applied to the half frame by horizontally pushing and pulling the top of the column. Although the cyclic loading simulations were defined in the quasi-static mode (i.e., dynamic effects are not investigated in this study), the analyses were conducted using the dynamic explicit method, with appropriate considerations to avoid inertia effects, as it is a more effective approach to problems involving relatively high strains compared to the implicit method. All of the analyses were continued up to the point that severe deformations and distortions occurred at a number of elements in which the strain values surpassed the maximum limit defined above. After reaching this point, the strength loss and excessive distortions of the elements make it impossible for the analysis to continue.

RESULTS FROM FEM ANALYSIS ON DIFFERENT BRACE-TO-BEAM CONNECTION DETAILS

Push-over Analysis on EBF-1 Model (with Offset)

The main objective in the design of EBF systems is to concentrate the plastic action in the link while keeping the other parts, especially the beam outside the link, essentially elastic. Considering this design objective, plastic behavior of model EBF-1 was studied under push-over analysis to track the initiation and distribution of the plastic strains in different parts of the structure to identify possible failure mechanisms. Because only half of the frame was modeled using anti-symmetric conditions in the middle of the link, two separate push-over analyses were conducted with displacements applied in opposite directions to check certain parts of the model for both tensile and compressive forces.

Figure 4 shows the graphs of base shear versus plastic link rotation for EBF-1 under monotonic applied displacements in two opposite directions. Both of the curves show significant strength loss at plastic link rotation values in the range 0.15 to 0.2 rad, which is expected for properly stiffened EBF frames. To distinguish the two opposite directions of applied displacements for push-over analyses, note that applying displacement in direction A causes tensile forces in the link bottom flange and applying displacement in direction B causes compression in the link bottom flange.

Considering the fact that the addition of a descending branch to the uniaxial behavior of the material can cause mesh-sensitive results for the elements which go beyond the maximum strength limit, push-over analysis for EBF-1 in direction B was repeated for a model with finer mesh. Mesh pattern 1 had elements with the approximate size of 10 mm fitting two elements along the thickness of the beam flange. Mesh pattern 2 was defined with elements half that size, with four elements across the thickness of the beam flange. Results from the two mesh patterns show the convergence of the finite element analyses for the different mesh sizes considered (Figure 4). The final mesh size was chosen such as to accommodate three elements across the thickness of the beam flange for all models to be used in the subsequent analyses in this study.

Results in Figure 4 show that EBF-1 loses strength at a relatively smaller plastic link rotation when monotonic loading is applied in the direction B. Loading in directions A and B creates positive and negative bending moments in the link, respectively. Significant loss of strength shows that a number of elements have surpassed the 15% strain limit (the onset of strength reduction) and are on the descending

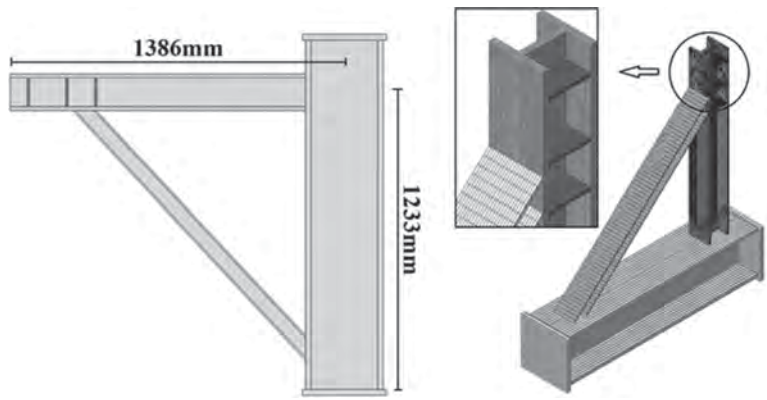

Fig. 3. Geometry and meshing of the finite element model.

branch of the stress-strain material model. To further investigate the differences between the location and strain response of the critical elements that cause the strength loss of EBF-1 under oppositely applied push-over loads, strain distribution and deformation plots were extracted from the ABAQUS analysis results for the two cases. Figure 5 shows the final deformed shapes of the EBF-1 half frame for both loading directions. Case A shows excessive deformations and element distortions in the web of the link close to one of the intermediate stiffeners leading to the strength loss of the structure. This type of behavior can be expected of EBF frames because the plastic action is intended to happen mostly in the link. On the other hand, case B shows excessive distortions for a different group of elements that are located in the offset area, which can be considered as a sign of improper behavior based on the design objective of EBF systems.

The difference in the mechanisms leading to strength loss under loading from two opposite directions is due to the different stress and strain distribution that occurs in the offset area for the two cases. The relatively small piece of beam flange that is located between the link stiffener and the edge of the brace flange is under combined axial and shear forces that are applied in opposite directions for cases A and B (Figure 6). The onset of base shear loss seen in Figure 4 for cases A and B is when, having reached the von Mises yield surface and progressed to larger equivalent plastic strain values, the state of 3D stress in a number of elements in the

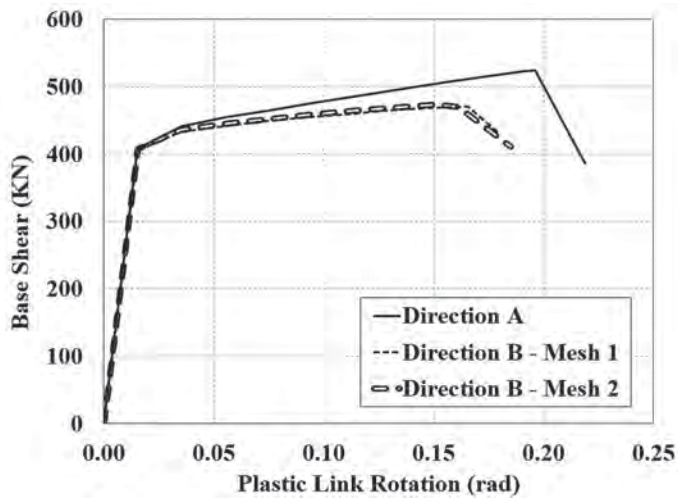

Fig. 4. Push-over analysis results for EBF-1 half frame under monotonic displacements in two opposite directions (plastic link rotation at the onset of base shear loss = 0.196 rad for case A and 0.161 rad for case B).

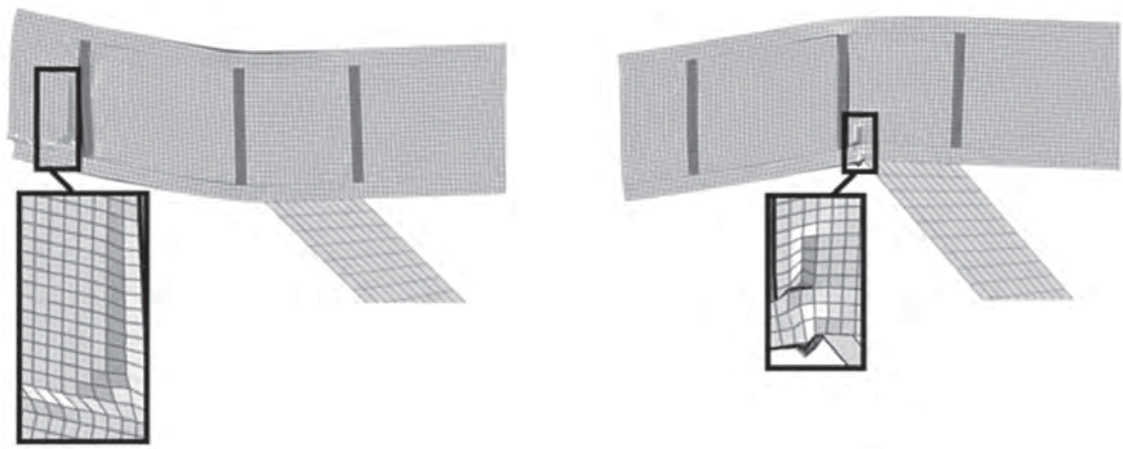

(a) *(b)*

Fig. 5. Final deformation results from push-over analysis of EBF-1 in two opposite directions: (a) loading in direction A; (b) loading in direction B (plastic link rotation at the onset of base shear loss is 0.196 rad for case A and 0.161 rad for case B).

model reaches a point where their von Mises stress is equal to the maximum stress defined at the end of the strain hardening branch of the material's behavior (the stress of 444.5 MPa corresponding to the strain of 15% for the problem at hand). Any fraction of added plastic strain from this point on takes the elements into the stress declining branch, leading to strength reductions and element distortions seen in Figures 4 and 5.

Cases A and B reach this limit at different plastic link rotation values and, more importantly for the purposes of this study, for elements located in different parts of the EBF model. Figure 7 shows Mohr's diagrams for the 3D state of stress at the offset area for cases A and B. Stresses were calculated based on average values for 342 elements located in the offset area at the onset of base shear loss. The figure shows that for case A, von Mises stress of the elements in the offset area have not reached the set maximum stress limit, and the drop in base shear was caused by the failure of a group of elements in the web of the link, as shown in Figure 5a. This is a preferred failure mode, as it allows development of yielding over the entire EBF link, prior to ultimately reaching strength degradation. For case B, on the other hand, the von Mises stress of the elements located in the offset area reached the set maximum stress limit, leading to a maximum shear stress on one of the principal planes equal to the corresponding maximum shear strength limit of the material ($\cong 0.57 \times 444.5 \cong 255$ MPa). Analogous to slip planes for yielding, attainment of the set shear strength limit

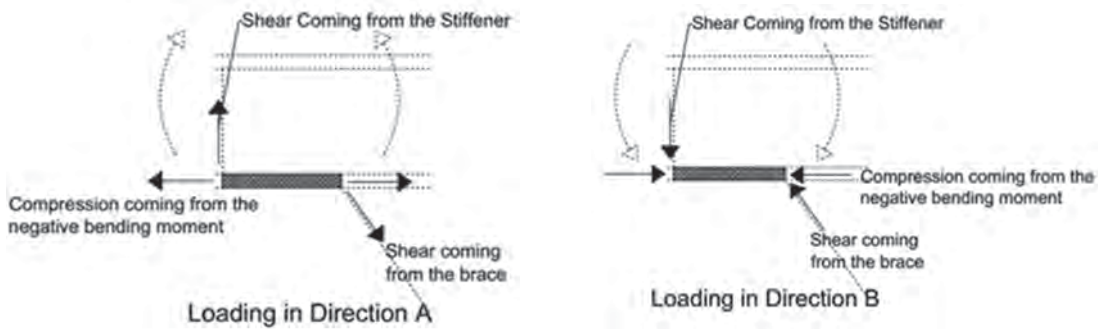

Fig. 6. Loads applied to the segment of the beam flange located at the offset: (a) loading in direction A; (b) loading in direction B.

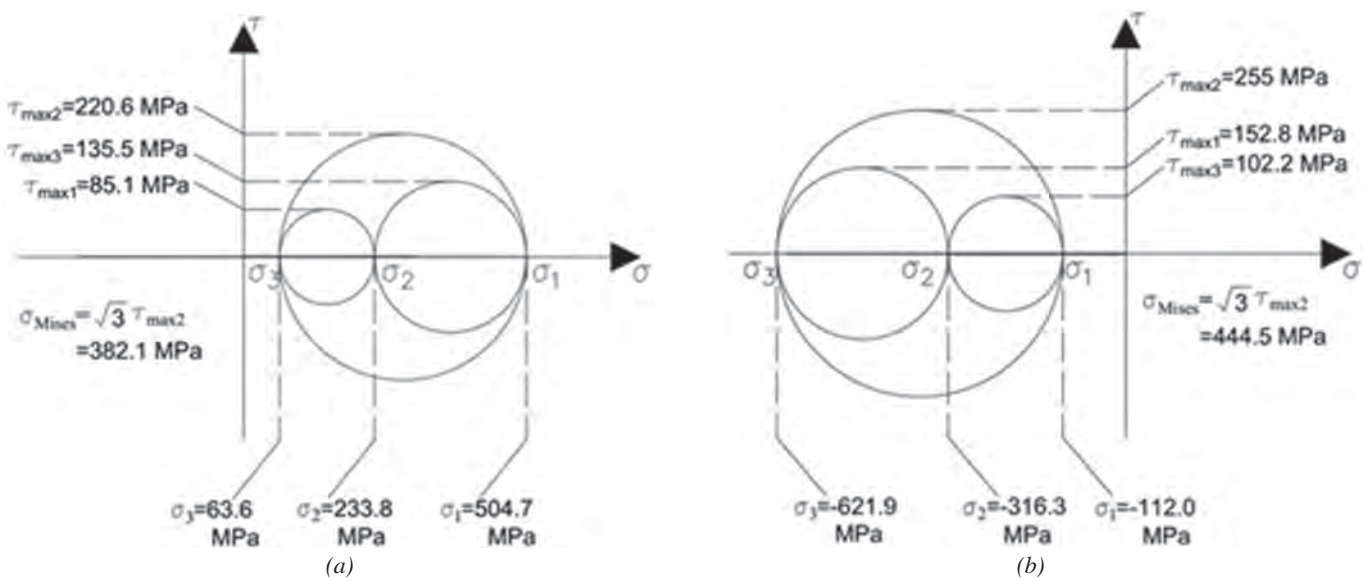

Fig. 7. Mohr's circle for 3D state of stress for elements in the offset area: (a) push-over loading in direction A; (b) push-over loading in direction B.

can be attributed to causing the possible onset of subsequent fracture. This assessment of stress conditions confirms that the failure of case B will start in the offset area.

The axial strain values (tensile for loading in direction A and compressive for loading in direction B) are plotted for a selected group of elements in the offset area versus the plastic link rotation values in Figure 8. The curves show that for case A the axial strain increases with the increasing plastic link rotation in the push-over analysis up to the point when the von Mises stress values for a number of elements in the web of the link reach the arbitrarily chosen maximum limit, causing the distortions shown in Figure 5a. From this point no more load is taken by the frame, and the axial strain remains constant for the elements in the offset area (excessive increase of plastic strains is limited to the distorted area in the web of the link). The scenario is different for case B, in which, as mentioned above, reaching the maximum stress level occurs in the beam flange at the offset area. This leads to an excessive increase in the average axial strain value for the selected group of elements in the offset area, as shown in Figure 8.

The equivalent plastic strain response parameter, $\bar{\varepsilon}^{pl}$, provided by ABAQUS was used to identify the initiation and propagation of the potential fractures in the structure. The parameter integrates the combined effects of all the plastic strain components in the 3D space and gives the cumulative plastic strain for each element using the following equation:

$$\bar{\varepsilon}^{pl} = \bar{\varepsilon}_0^{pl} + \left(\sqrt{\frac{2}{3} \dot{\varepsilon}^{pl} : \dot{\varepsilon}^{pl}} \right) dt \qquad (1)$$

where $\bar{\varepsilon}^{pl}$ is the initial equivalent plastic strain, which is set to zero for all the elements, and $\dot{\varepsilon}^{pl}$ is the plastic strain rate tensor. According to the ABAQUS *Theory Manual*, the integration over time accumulates the incremental plastic strains of the elements throughout the analysis (Simulia, 2012). Based on the material behavior defined for the beam (including the link), an equivalent plastic strain equal to 19.8% for any element in the models built in this study means that it has reached the fracture strain limit (total strain of 20%, considering the elastic strain limit of 0.2%). Going past this limit, the element will continue to experience higher plastic strain values without contributing to the strength or resistance of the structure.

Figure 9 shows the distribution of equivalent plastic strain for EBF-1 under monotonic loading in two opposite directions. The contours are plotted on the undeformed shapes to get a clearer picture of the equivalent plastic strain distribution. Locations with $\bar{\varepsilon}_0^{pl}$ values above 19.8% (areas shaded in gray) can be considered as those having exceeded the fracture initiation points. Results show that the elements reaching the fracture plastic strain limits are located at the web of the link for the frame loaded in direction A and at the offset area for the frame loaded in direction B (as indicated previously, in Figure 5). The color contours for EBF-1 loaded in direction B suggest that a fracture may initiate in the beam flange and propagate further into the beam outside the link, following a pattern that resemble the one reported for the EBF damaged during the Christchurch 2011 earthquake.

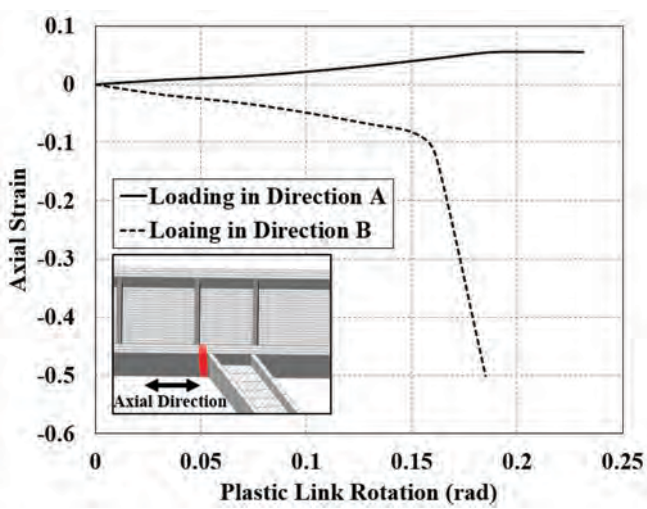

Fig. 8. Average axial strain values for a selected group of elements at the offset area from the push-over analysis of EBF-1 under loading in two opposite directions.

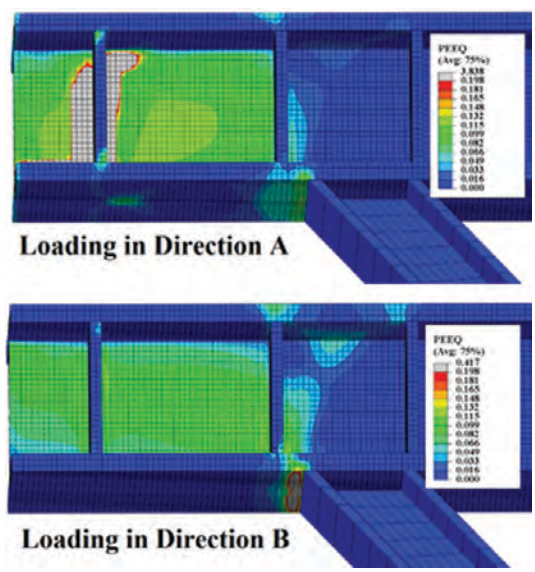

Fig. 9. Equivalent plastic strain distribution for EBF-1 under monotonic loading in two opposite directions (plastic link rotation at the onset of base shear loss is 0.196 rad for case A and 0.161 rad for case B).

Push-over Analysis on EBF-2 Model (without Offset)

To further examine the effects of the mentioned detailing issue on the static behavior of the EBF frames, model EBF-2 was subjected to a push-over analysis for displacements in direction B, which puts the bottom flange of the link in compression. Recall that in EBF-2, the brace flange connection point to beam lines up vertically with the link stiffener, which is located at the intersection of the centerlines of the beam and the brace.

Figure 10 shows the final deformed shape of EBF-2 after the occurrence of excessive distortions, along with the equivalent plastic strain distribution for the elements plotted on the undeformed shape of the frame. Results show that, when subjected to a push-over loading conditions similarly to case B discussed above for EBF-1, the average von Mises stress values for the elements in the beam to brace flange connection point (close to the link stiffener), did not reach the maximum stress limit (and onset of strength loss) until the frame started to lose base shear strength because a number of elements located in the web of the link reached the maximum stress limit at the plastic link rotation of 0.27 rad, which is significantly larger than the onset of base shear strength loss for EBF-1 (i.e., 0.161 rad for case B). Thus, results show that proper alignment of the brace flange with the link stiffener (which was located at the intersection of the beam and brace centerlines) transferred the plastic action into the link, preventing the occurrence of yielding (and subsequently reaching the maximum stress level) in the brace-to-beam connection area.

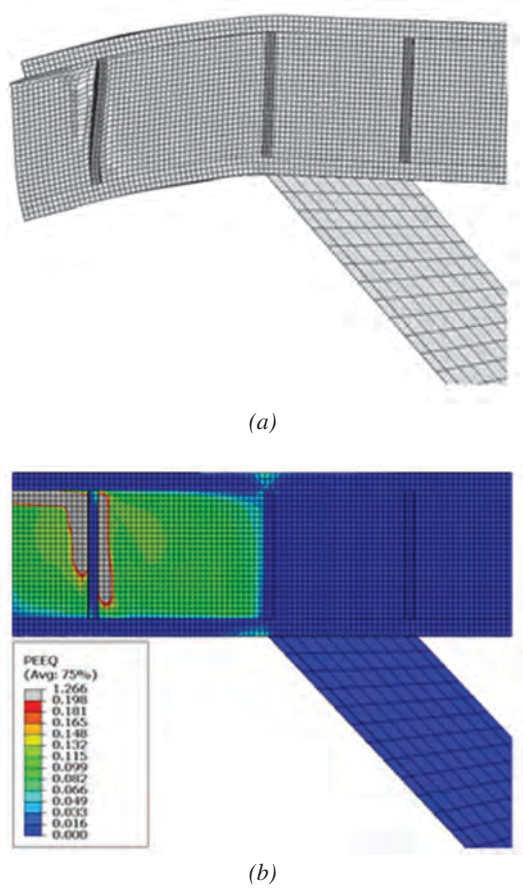

(a)

(b)

Fig. 10. Results from push-over analysis of EBF-2 with bottom flange of the link in compression after occurrence of excessive element distortions: (a) final deformed shape; (b) distribution of equivalent plastic strains on all elements (plastic link rotation at the onset of base shear loss= 0.27 rad).

Comparison of results in Figures 9 and 10 highlights the possible impact on behavior caused by slight differences in the detailing of the brace-to-beam connection, and how location of the link stiffener with respect to these two members can affect the ultimate inelastic behavior of the EBF frame. Under similar push-over analysis conditions, EBF-2 developed a maximum plastic link rotation of 0.27 rad and all significant plastic behavior concentrated in the link, whereas EBF-1 lost resistance at the significantly smaller plastic link rotation of 0.16 rad and developed substantial plastic behavior in the offset area (average stress values reached the maximum defined value).

Cyclic Analysis on Models with All Four Detailing Alternatives

To further investigate whether the stress concentration observed above can have an impact on the seismic performance of links, the four detailing configurations shown in Figure 2 were subjected to cyclic lateral loading. Although low-cycle fatigue is not considered in this study, cyclic loading was applied to the models because cumulative cyclic inelastic deformations in load reversals can induce imperfections in the structure. These imperfections can generally lead to total strength losses and element distortions, which, for the models studied here, is equivalent to reaching to the arbitrarily chosen maximum stress or its corresponding maximum strain limit, at smaller lateral displacements than those predicted under monotonic loading conditions.

Cyclic lateral displacements were applied to all models to create the plastic link rotation cycles shown in Figure 11. The arbitrarily selected displacement protocol consists of inelastic cycles creating different amplitudes of plastic link rotation of the EBF frames. Starting with a plastic rotation of 0.025 rad, it increases in two steps up to 0.08 rad and stops at rotation of 0.06 rad during the final unloading segment. Actual maximum plastic link rotation was slightly above or below the 0.08 rad limit for some of the models considered because the link's geometry was changed slightly for the different models, but the same lateral displacements were applied to all models. As mentioned before, because low-cycle fatigue issues were not considered in this study, and for computational expediency, just a few inelastic

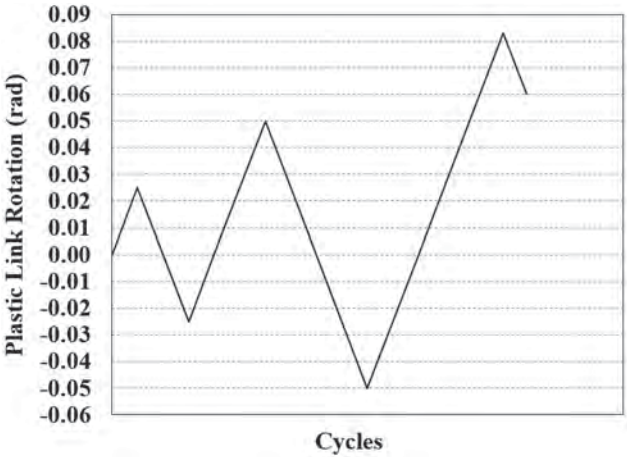

Fig. 11. Cyclic lateral loading protocol applied to the models.

cycles were applied to the structure to create imperfections, avoiding replicating the type of cyclic displacement protocols typically done in experimental studies (as this would have required substantially longer computational time). The arbitrarily chosen maximum equivalent plastic strain limit of 19.8% (used for push-over analysis) was kept as the limit for the cumulative plastic strain in the cyclic analyses. This limit was chosen to provide a uniform basis of comparison for all models while limiting analysis to a small number of cycles (for computational expediency), recognizing that a significantly higher limit would have to be used if the models were analyzed under the full AISC loading protocol to consider the qualification of EBFs (which is not necessary here, for the purpose of the current study).

Figure 12 shows the resulting base shear versus plastic link rotation values from cyclic analyses for all four models.

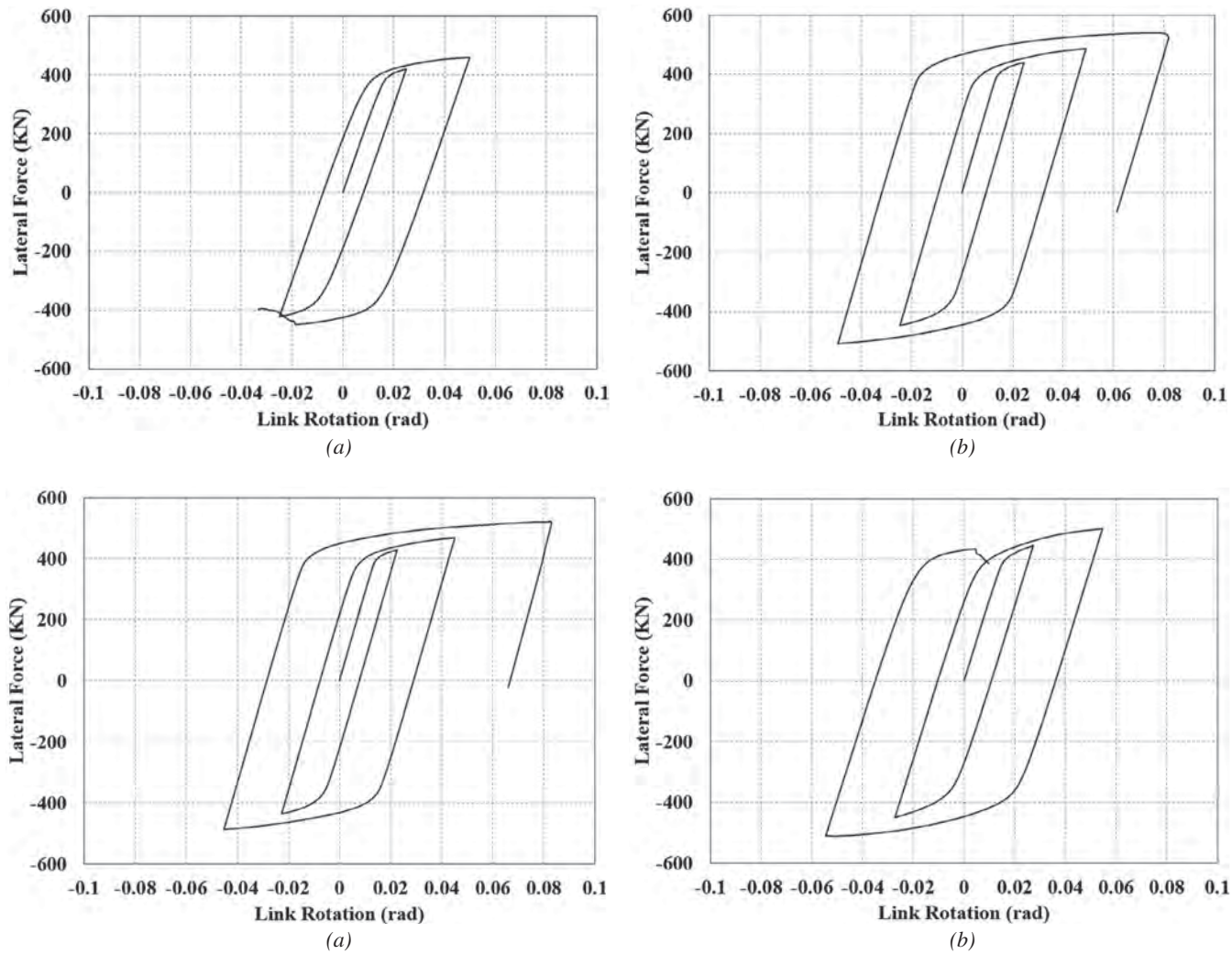

Fig. 12. Base shear versus plastic link rotation results from cyclic analyses: (a) EBF-1; (b) EBF-2; (c) EBF-3; (d) EBF-4.

Analysis of model EBF-1 terminated due to high compressive strains and element distortions in the offset area, similarly to what was observed in the push-over analysis but at a relatively smaller plastic link rotation value (0.03 rad for cyclic analysis as opposed to 0.16 rad for the monotonic one). The difference is due to the fact that equivalent plastic strain for the elements in the offset area reaches the defined maximum limit (19.8%) much sooner in the cyclic analysis because of the accumulation of plastic strain during the cycles. Because plastic action is concentrated in the offset area rather than being distributed in the whole link, the accumulated plastic strain values reach the maximum limit in a few cycles.

EBF-2 exceeded the plastic link rotation of 0.08 rad without problem, showing the effectiveness of the adjustment made to the connection. The removal of the offset has transferred the plastic action into the link, preventing the elements at the connection point from reaching the maximum limit of the equivalent plastic strain. Interestingly, EBF-3 also exceeded the 0.08 rad plastic link rotation, which supports the AISC 341-10 recommendation, provided that the link stiffener lines up with the point where the brace's flange connects to the beam flange. This result shows that if the geometry of EBF-2 cannot be accomplished (due to limits in available brace depths), satisfactory ductile behavior of the frame can still be ensured by locating the stiffener such as to eliminate the stiffener-to-brace flange offset.

Finally, while EBF-4 resisted two complete cycles (i.e., exhibiting a ductile behavior better than EBF-1), it lost strength at the beginning of the third cycle in a pattern similar to that of EBF-1 in the offset area. However, better performance of EBF-4 suggests that it has been more effective in distributing the plastic action into the link compared to EBF-1. To further investigate this issue and overall differences in the behaviors of the four detailing alternatives considered here, contours of equivalent plastic strain, $\bar{\varepsilon}^{pl}$, were plotted on the undeformed shapes of the models at the final stages of their analyses (Figure 13). The analysis for each model was terminated either because of the completion of the displacement protocol (for EBF-2, 3) or because of significant strength loss and element distortions in the model (for EBF-1, 4). The latter occurred when a number of elements surpassed the maximum plastic strain limit (19.8%), which led to their severe distortions. The plastic link rotation values for all models at the analysis termination points can be determined from the ends of the curves plotted in Figure 12.

The orientation of the equivalent plastic strain contour lines in Figure 13 suggests (in ideal conditions) probable failure patterns that may occur once strains have reached extreme values. However, it is recognized that the ultimate failure mode of EBF links may also be affected by a number of other factors not considered here, such as triaxial residuals stresses and micro-defects introduced during welding of the stiffeners, which may impact low-cycle fatigue life.

The plots in Figure 13 show that models EBF-1 and EBF-4 will have a failure at the offset between the link stiffener and the brace flange similar to what was seen following the Christchurch earthquake series. The stress contours reveal that the elements of the link for EBF-4 have equivalent plastic strain values in the range of 0.10 to 0.13 rad, which is considerably higher than the values for the link elements of EBF-1 (0.02 to 0.06 rad). The difference shows the more effective distribution of plastic action in the link of EBF-4 as the main reason for its better performance with respect to EBF-1. It should be mentioned that a closer look at the arbitrarily selected geometry of EBF-4 (Figure 2) reveals that the intersection of beam and brace centerlines (located outside the link) almost lines up vertically with the brace flange to beam connection point, although the stiffener is moved away to create the offset. This might be one possible reason for the EBF-4's being more effective in transferring the plastic action toward the link, as compared to EBF-1. Note that this is a just a suggested interpretation of the simulation results and that, at any rate, a detailing similar to EBF-4 is unlikely to occur in real cases.

Model EBF-2 has experienced its maximum equivalent plastic strain value in the web of the link close to the intermediate stiffener. The contour colors show that if the applied displacement protocol was extended to continue the analysis, the first group of elements surpassing the fracture plastic strain limit would be located in the same area as expected of EBF systems. EBF-3 shows an acceptable ductile behavior by transferring the plastic action to the link and surviving during the applied displacement protocol. Although EBF-3 seems like an easier solution to implement than EBF-2 to eliminate the offset problem, the orientation of the contour lines and their colors, which are plotted at the same stage of analysis for both models (i.e., at the end of the displacement protocol, when plastic link rotation have reached 0.06 rad), show the possibility of a more premature failure for EBF-3 compared to the ideal case EBF-2. Figure 13 suggests that the possible fracture of EBF-3 may start in the link flange, close to its meeting point with the brace flange, and progress in a path toward the intersection of the link and brace centerlines. It appears that although moving the stiffener to line up with the brace flange has eliminated the offset for EBF-3 leading to an acceptable behavior, it may still ultimately fail by a fracture starting in the link flange (rather than in the web of the link) if higher displacement amplitudes are applied. Considering the plots of Figure 13 altogether, EBF-2 shows the best behavior among the four alternatives.

SIMULATION OF THE POTENTIAL FRACTURE IN EBF SYSTEMS

In the above nonlinear inelastic finite element analyses, average equivalent plastic strain values were calculated, and elements with strain values exceeding the specified fracture limit of the material were deemed to have failed (even though the elements remained part of the continuum). While the resulting strain contours displayed zones of largest strains near the region where actual fracture was observed in Christchurch for a similar configuration (EBF-1), it is worthwhile to further investigate the behavior of that specific case using the damage model for ductile materials available in ABAQUS. This model can simulate fracture propagation in the EBF-1 frame by automatically deleting elements that reach a full-damage criterion during the analysis. Moreover, because the damage evolution capability used in the ABAQUS model degrades the element stiffness based on plastic displacements and fracture energy measures rather than just plastic strain, it can generally provide reasonable accuracy in replicating fracture propagation, although it is recognized that exact matching of a fracture

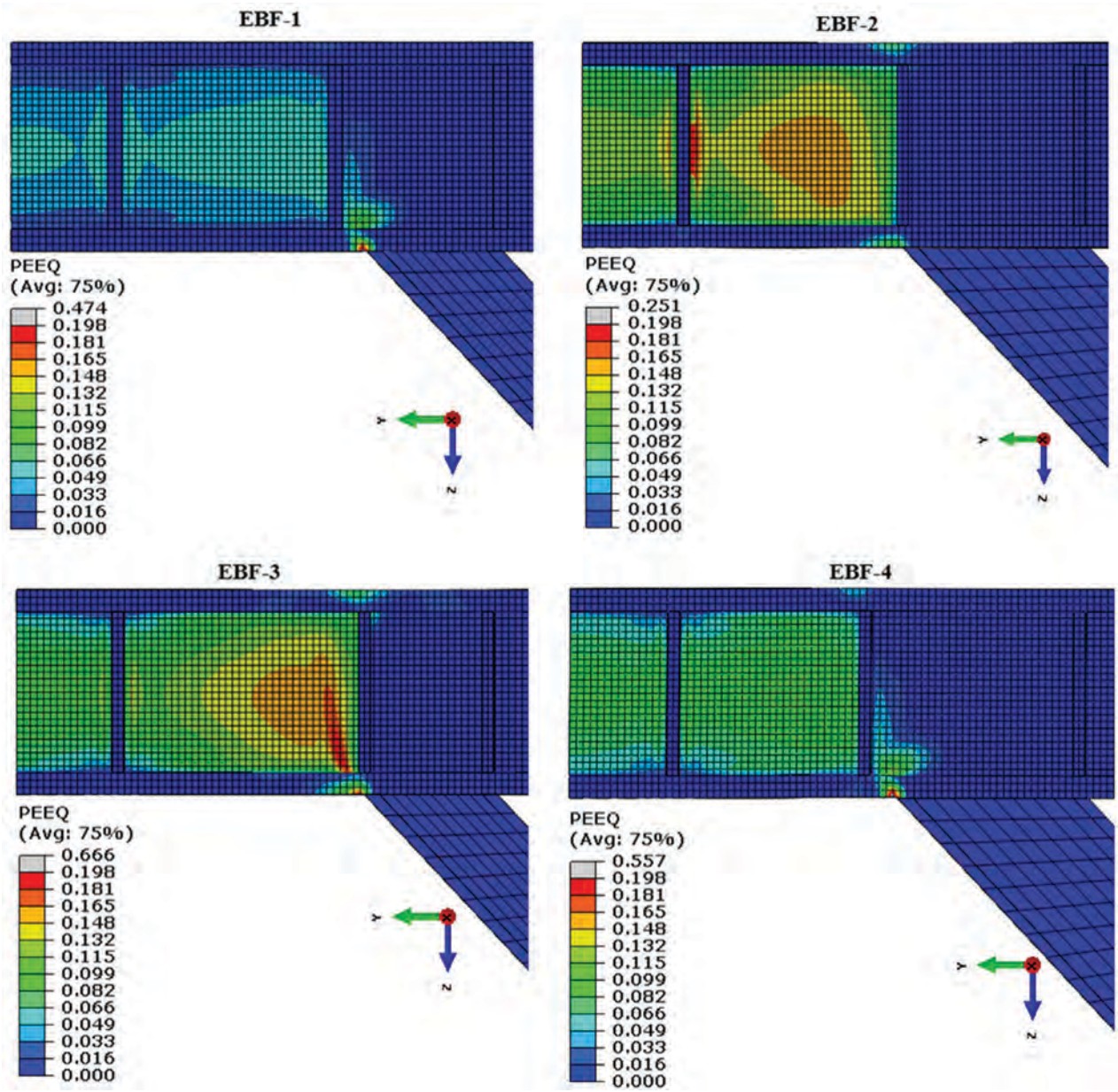

Fig. 13. Distribution of equivalent plastic strain values for all four models close to their failure under cyclic loading.

path may be difficult. The purpose is not to obtain perfect replication of the progression and path of the fracture, but to get a preliminary indication of how it could propagate after its initiation. Note that achieving a perfect replication of the fracture propagation path would need the implementation of an adaptive step-by-step mesh refinement strategy at the crack tip, similarly, for example, to what was done in a study by Roy and Dodds (2001) on the simulation of ductile crack growth in thin aluminum panels—but such a level of refinement was beyond the of scope of this study.

This type of material modeling, to predict the onset of damage and model the progressive damage and failure of ductile metals, requires three main properties: the elastic-plastic behavior of the undamaged material, a damage initiation criterion and a damage evolution response that can include the criteria for removal of failed elements. The specifics of the damage simulation model for ductile metals used in this investigation are summarized in the following paragraphs (Simulia, 2012).

The ductile fracture criterion was used as the damage initiation model in this study. The model assumes that the equivalent plastic strain at the onset of damage, $\bar{\varepsilon}_D^{pl}$, can be defined as a function of stress triaxiality and strain rate:

$$\bar{\varepsilon}_D^{pl} = f(\eta, \dot{\bar{\varepsilon}}^{pl}) \tag{2}$$

where $\eta = -p/q$ is the stress triaxiality, p is the pressure stress, q is the von Mises equivalent stress, and $\dot{\bar{\varepsilon}}^{pl}$ is the equivalent plastic strain rate. A state variable, ω_D, is defined by Equation 3 and increases monotonically with plastic deformation with incremental steps that are calculated by Equation 4 for each increment of the analysis. The damage initiation criterion is met when the condition $\omega_D = 1$ is satisfied.

$$\omega_D = \int \frac{d\bar{\varepsilon}^{pl}}{\bar{\varepsilon}_D^{pl}} \tag{3}$$

$$\omega_D = \frac{\bar{\varepsilon}^{pl}}{\bar{\varepsilon}_D^{pl}} \tag{4}$$

The damage evolution capability in this model works by progressive degradation of material stiffness leading to its failure. The model is based on mesh-independent measures, including plastic displacements and energy dissipation, to simulate the damage evolution of the material after the damage initiation. Figure 14 shows the stress-strain curve for a material with progressive damage degradation, where $\sigma_{y0}, \bar{\varepsilon}_0^{pl}$ are the yield stress and equivalent plastic strain at the onset of the damage and $\bar{\varepsilon}_f^{pl}$ is the equivalent plastic strain at failure when the overall damage variable reaches its maximum value ($D = 1$).

Because the value of $\bar{\varepsilon}_f^{pl}$ depends on the characteristic length of the element, L, which is a mesh dependent parameter, the damage evolution law is either based on the equivalent plastic displacement, $\bar{u}^{pl}$, or fracture energy dissipation, G_f.

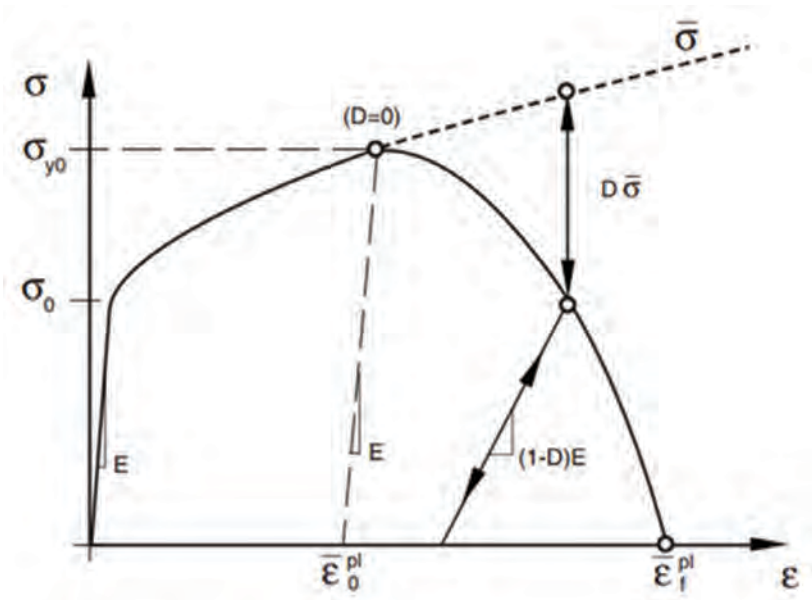

Fig. 14. Stress-strain curve for material with progressive damage degradation (Simulia, 2012).

$$G_f = \int_{\bar{\varepsilon}_0^{pl}}^{\bar{\varepsilon}_f^{pl}} L\sigma_y d\bar{\varepsilon}^{pl} = \int_0^{\bar{u}_f^{pl}} \sigma_y d\bar{u}^{pl} \quad (5)$$

The fracture energy is calculated based on the characteristic length of each element according to Equation 5. The definition of the characteristic length, L, depends on the geometry and formulation of the element. It is defined as the length of a line across a first order element, or half of same length for second-order elements. Equation 5 also introduces the definition of the equivalent plastic displacement, $\bar{u}^{pl}$, which has the change rates of $\dot{\bar{u}}^{pl} = 0$ before damage initiation and $\dot{\bar{u}}^{pl} = L\dot{\bar{\varepsilon}}^{pl}$ after it. At any given time during the analysis the stress tensor is given by:

$$\sigma = (1 - D)\bar{\sigma} \quad (6)$$

where D is the overall damage variable and $\bar{\sigma}$ is the effective (undamaged) stress tensor computed in the current increment. ABAQUS can be set up to remove the elements that reach the limit $D = 1$.

For these analyses, damage initiation was set up to start at the equivalent plastic strain of 0.15 for the beam of EBF-1 model (including the link). Damage evolution was defined based on the equivalent plastic displacement with a linear softening that would reach failure at the equivalent plastic displacement calculated using the characteristic length of 5 mm (from the mesh size) and failure plastic strain of 19.8%. ($\bar{u}_f^{pl} = L\bar{\varepsilon}_f^{pl}$). The element deletion option was also used to remove the elements that reach the failure criterion. EBF-1 was subjected to cyclic lateral displacements for fracture simulation. The mesh size with three elements along the thickness of the beam flange, which was shown to be fine enough based on the mesh sensitivity analysis check mentioned above, was used in an attempt to predict the direction of the fracture at the offset area.

Figure 15 shows plots of the resulting simulated fracture in the EBF-1 model with and without the equivalent plastic strain contour lines. The simulated fracture initiated at almost the same location as the one reported from the Christchurch earthquake (Figure 1a) and progressed into the web of the beam outside the link. However, due to the mesh dependency of the fracture growth path and the fact the simulated fracture growth could only occur along the element edges, the simulated fracture progresses in a relatively more vertical path compared to the one occurred in the Christchurch earthquake. The problems of mesh size and mesh orientation sensitivity for fracture simulation can be resolved by using an adaptive mesh refinement strategy, where the new topology around the crack tip goes through mesh refinement for the next step of the analysis (similar to the study mentioned above by Roy and Dodds). However, using such computational techniques was beyond the scope of this study. Note that the fracture also follows a path similar to what was predicted from the equivalent plastic strain distribution contours in Figure 9 obtained from the static push-over analysis of EBF-1 with the link's bottom flange in compression. Contour line colors reveal that most of the plastic behavior is concentrated in the offset area with a limited yielding in the link (which is consistent with slight flaking of the paint seen in the link of the fractured EBF shown in Figure 1).

CASE STUDY

Push-over Analysis of a Model Built Using the As-Constructed Dimensions and Details of the EBF Frame Fractured in Christchurch

Considering the problematic effects of the offset in the brace-to-beam connection area on the overall behavior of EBF frames (as demonstrated above), an additional finite element model was built using the as-constructed dimensions and details of one of the EBF frames that was reported

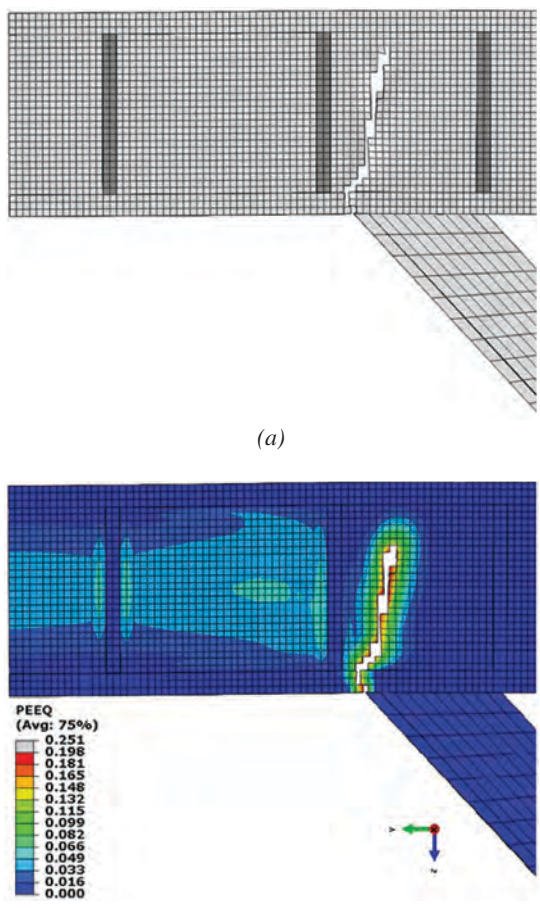

(a)

(b)

Fig. 15. Simulated fracture at the offset between the link stiffener and the brace flange of EBF-1 (with and without the equivalent plastic strain contour lines).

to have fractured during the Christchurch earthquake series. This model is referred to as EBF-5 from this point on in this paper. The dimensions of the members (i.e., 460UB67 and 250UC73 sections for the beam and brace) were adopted from a recent study on these fractures (Marshall, 2013) and the model was built as a complete frame to account for the fact the offset was only observed on one side of the fractured frame. Push-over analyses were conducted in two opposite directions and the results of equivalent plastic strain distribution at the onset of base shear loss is shown in Figure 16.

Figure 16a shows that for push-over loading in direction A (i.e., offset area in compression), considerable plastic action has occurred in the link, while the flange of the beam in the offset area remains well below the 15% equivalent plastic strain limit; in other words, no strength loss has occurred for the elements of the beam flange in the offset area when the elements in the link reached the onset of strength loss. Loading in direction B (i.e., offset area in tension), on the other hand, has caused a significant plastic strain concentration in the elements of the beam flange in the offset area, which can be considered as a possible premature fracture initiation point (Figure 16b). Note that this situation is somewhat different than what had been observed previously for push-over of EBF-1 (discussed above), as the critical stresses in the offset occur in tension rather than compression. The difference is due to the fact that EBF-5 has a much thinner and more flexible beam flange, and most of the compression load, when the frame is pushed in direction A, is sustained by the web of the beam. Note that no such strain concentration occurred on the right side of the link where brace flange aligned with the link end stiffener.

Even though loading in direction B has the more critical equivalent plastic strain distribution, the offset area can also be considered to cause problems for the frame when loading is applied in direction A. Overall, the behavior of EBF-5 under push-over loading underscored the possibility of the occurrence of premature EBF fractures due to the stress and strain concentrations in the offset area.

Incidentally, it was suspected that, for the specific case of the Christchurch EBF, local web yielding in the beam in the offset area might have increased the demand in the beam flange, thereby leading to a possible subsequent fracture. To verify this, a simple check of the 2010 AISC *Specification* criteria (Specification Equation J10-2) for local web yielding under concentrated loads was performed using the vertical component of the load in the brace flange connected to the beam in the offset area (calculated from the finite element analysis results). Calculations showed that the concentrated load applied by the brace flange was about 70% of the available strength provided per AISC *Specification* Equation J10-2. It was inferred that local web yielding in the beam could not be the main reason for the fracture initiation.

CONCLUSION

Four eccentrically braced frames having different locations for their link stiffeners with respect to the beam-to-brace flange connection point and intersection of brace-to-beam centerlines were analyzed using the finite element method to investigate their potential vulnerabilities and possibly explain some of the fractures reported following the Christchurch earthquake series of 2010 and 2011.

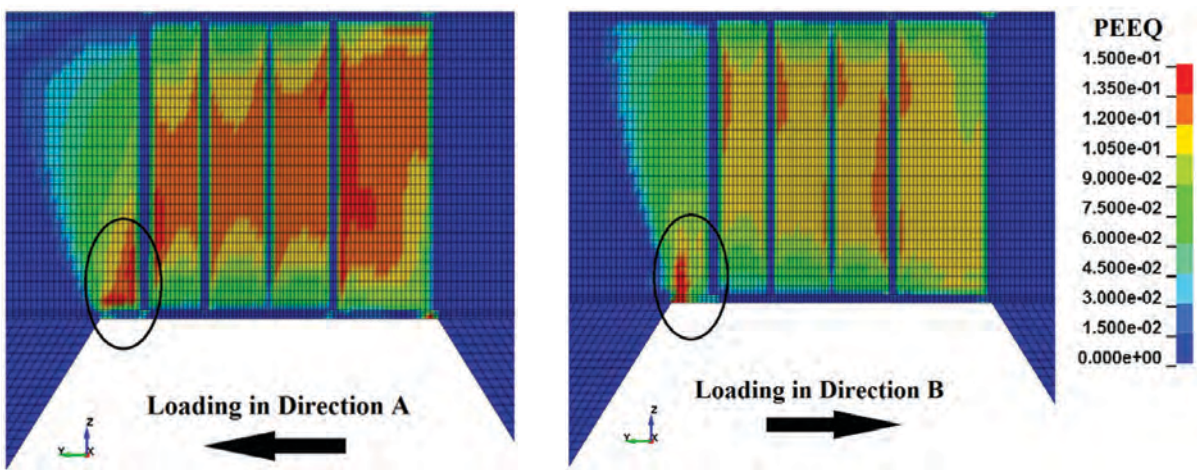

Fig. 16. Distribution of equivalent plastic strains at the onset of base shear loss for EBF-5 subjected to push-over loading in (a) direction A (plastic link rotation = 0.23 rad); (b) direction B (plastic link rotation = 0.18 rad).

Results from limited monotonic and cyclic analyses, as well as from analyses considering fracture propagation based on the use of damage models, combine to demonstrate that the eccentricity (misalignment) of link stiffeners with respect to the beam-to-brace flange connection point is responsible for the observed premature failures outside of the link. This is attributed to the severe stress concentration condition that develops in that area. The conditions leading to such failures were not observed to develop in absence of this eccentricity.

Modifying the section of the brace to achieve a condition in which the intersection of the beam and brace centerlines line up vertically with the edge of the brace flange as well as with the link-end stiffener was shown to be effective in solving the potential fracture problem by properly transferring the plastic action into the link. For cases where modifying the brace section to achieve the above condition is not possible, analyses showed that simply moving the link stiffener to eliminate the offset between the end stiffener and beam-to-brace flange connection point is almost as effective to improve the overall behavior of the EBF frame, even if the intersection of brace-to-beam centerlines falls inside the link. Note that the results of this study are limited to EBF frames with wide flange braces, as all of the simulation models were built with that configuration. Even though it is likely that the existence of the offset might cause similar problems for frames in which other types of brace sections and connections are used, the distribution of the plastic strains and subsequent damage might be different for those cases and needs further investigation.

REFERENCES

AISC (2005), ANSI/AISC 341-05, *Seismic Provisions for Structural Buildings,* American Institute of Steel Construction, Chicago, IL.

AISC (2010a), ANSI/AISC 360-10, *Specification for Structural Steel Buildings,* American Institute of Steel Construction, Chicago, IL.

AISC (2010b), ANSI/AISC 341-10, *Seismic Provisions for Structural Steel Buildings, American Institute of Steel Construction,* Chicago, IL.

Berman, J. and Bruneau, M. (2008), "Tubular Links for Eccentrically Braced Frames. II: Experimental Verification, *Journal of Structural Engineering*, ASCE, Vol. 134, No. 5, pp. 692–701.

Bruneau, M., Anagnostopoulou, M., MacRae, G., Clifton, C. and Fussell, A. (2010), "Preliminary Report on Steel Building Damage from the Darfield (New Zealand) Earthquake of September 4, 2010," *New Zealand Society for Earthquake Engineering Bulletin*, Vol. 43, No. 4, pp. 351–359.

Clifton, C., Bruneau, M., MacRae, G., Leon, R. and Fussell, A., (2011), "Steel Structures Damage from the Christchurch Earthquake of February 22, 2011, NZST," *Bulletin of the New Zealand Society for Earthquake Engineering*, Vol. 44, No. 4, pp. 297–318.

Engelhardt, M.D. and Popov, E.P. (1989a), "On Design of Eccentrically Braced Frames," *Earthquake Spectra*, Vol. 5, No. 3, pp. 495–511.

Engelhardt, M.D. and Popov, E.P. (1989b), "Behavior of Long Links in Eccentrically Braced Frames," *Report: UCB/EERC*-89/0*1,* California University, Richmond. Earthquake Engineering Research Center, Sponsor: National Science Foundation, Washington, DC.; American Iron and Steel Institute, Washington, DC, 415p, January, 1989.

Hjelmstad, K.D. and Popov, E.P. (1983), "Cyclic Behavior and Design of Link Beams," *Journal of Structural Engineering*, Vol. 109, No. 10, pp. 2387–2403.

Kanvinde, A.M., Grilli, D.A. and Marshall, K. (2012), "A Framework for Forensic Examination of Earthquake Induced Steel Fracture Based on the Field Failures in the 2011 Christchurch Earthquake," *Proceedings of Fifteenth World Conference on Earthquake Engineering*, Lisbon, Portugal.

Kasai, K. and Popov, E.P. (1986a), "General Behavior of WF Steel Shear Link Beams," *Journal of Structural Engineering*, ASCE, Vol. 112, No. 2, pp. 362–382.

Kasai, K. and Popov, E.P. (1986b), "Cyclic Web Buckling Control for Shear Link Beams," *Journal of Structural Engineering*, ASCE, Vol. 112, No. 3, pp. 505–523.

Kasai, K. and Popov, E.P. (1986c), "Study of Seismically Resistant Eccentrically Braced Steel Frame Systems," *Report: UCB/EERC*-86/01*,* California University, Richmond. Earthquake Engineering Research Center, Sponsor: National Science Foundation, Washington, DC, 303p.

Malley, J.O. and Popov, E.P. (1984), "Shear Links in Eccentrically Braced Frames," *Journal of Structural Engineering*, Vol. 110, No. 9, pp. 2275–2295.

Marshall, K. (2013), "Earthquake Induced Eccentrically Braced Frame Link Fracture in the Christchurch Hospital Parking Garage," Master's Thesis, University of California, Davis.

Merovich, A.T., Nicoletti, J.P. and Hartle, E. (1982), "Eccentric Bracing in Tall Buildings," *Journal of the Structural Division*, Vol. 108, No. ST-9, pp. 2066–2080.

Popov, E.P., Kasai, K. and Engelhardt, M.D. (1987), "Advances in Design of Eccentrically Braced Frames," *Bulletin of the New Zealand National Society for Earthquake Engineering*, Vol. 20, No. 1, pp. 22–29.

Ricles, J.M. and Popov, E.P. (1987b), "Dynamic Analysis of Seismically Resistant Eccentrically Braced Frames," *Report: UCB/EERC*-87/07, California University, Richmond. Earthquake Engineering Research Center, Sponsor: National Science Foundation, Washington, DC; American Iron and Steel Institute, Washington, DC, 364p.

Ricles, J.M. and Popov, E.P. (1987a), "Experiments on Eccentrically Braced Frames with Composite Floors," *Report: UCB/EERC*-87/06, California University, Richmond. Earthquake Engineering Research Center. Sponsor: National Science Foundation, Washington, DC; American Iron and Steel Institute, Washington, DC, 330p.

Roeder, C.W. and Popov, E.P. (1978), "Eccentrically Braced Steel Frames for Earthquakes," *Journal of the Structural Division,* ASCE, Vol. 104, No. 3, pp. 391–412.

Roy, Y.A., and Dodds R.H, Jr. (2001), "Simulation of Ductile Crack Growth in Thin Aluminum Panels Using 3-D Surface Cohesive Elements," *International Journal of Fracture*, Vol. 110, No. 1, pp. 21–45.

Simulia (2012), "Abaqus Documentation," http://www.3ds.com/products-services/simulia/support/documentation/.

The Chevron Effect—Not an Isolated Problem

PATRICK J. FORTNEY and WILLIAM A. THORNTON

ABSTRACT

Vertical braces that connect concentrically to frame beams away from the beam-column joint are referred to as V-type or inverted V-type braced frames, as chevron braced frames or as mid-span braces. The braces are commonly connected to the frame beam using gusset plates. Typically, these gusseted connections are analyzed and designed considering only the effect of the brace forces on the region of the beam within the connection region. This is a reasonable approach when the summation of the vertical components of the brace forces is zero. However, when the vertical components result in a non-zero net vertical force (also referred to as an unbalanced force), analyzing and designing the connection as if it were isolated from the frame may result in a significantly undersized beam, requiring expensive beam web and flange reinforcement. In this paper, the effect of the brace forces on the beam in this type of braced frame configuration is referred to as the *chevron effect*. This paper presents a method for determining the distribution of brace forces within the connection and also the impact of the brace force distribution on the frame beam. The mechanism analysis required by the 2010 AISC *Seismic Provisions for Structural Steel Buildings*, AISC 341-10, is presented, and the discussion illustrates the importance of considering the entire frame when evaluating the impact of the brace forces on the beam.

Keywords: Gusset plates, chevron braces, V-braces, brace forces, analysis, design.

When vertical braces connect concentrically to frame beams away from the beam-column joint, these concentrically configured braces are referred to as V-type or inverted V-type braced frames. It is also common to refer to these types of braced frames as chevron braced frames or mid-span braces. The braces are commonly connected to the frame beam using gusset plates. Typically, these gusseted connections are analyzed and designed considering only the effect of the brace forces on the portion of the beam within the connection region. This is called designing the connection in isolation and is a reasonable approach when the summation of the vertical components of the brace forces is zero. However, when the vertical components result in a non-zero net force, the connection should not be analyzed and designed as if it were isolated from the frame. The beam span and the location of the work point along the span of the beam must be considered in order to fully understand the impact of the brace forces on the frame beam. In this paper, the effect of the brace forces on the beam in this type of braced frame consideration is referred to as the *chevron effect*. This paper presents a method for determining the distribution of brace forces within the connection and also the impact of the brace force distribution on the frame beam. To illustrate the chevron effect, the mechanism analysis required by AISC 341-10, *Seismic Provisions for Structural Steel Buildings* (AISC, 2010a) is presented. The discussion illustrates the importance of considering the entire frame when evaluating the impact of the brace forces on the beam and the potentially unconservative results when evaluating the connection as if it were isolated from the frame.

Concentric braced frame structures can be set up in various configurations. Braces can frame to beam-column joints, to various locations along the height of the frame column and to various locations along the span of the frame beam. The discussion presented in this paper focuses on a concentric brace configuration referred to in AISC 341-10 as V-type or inverted V-type configurations, also known as chevron braces or mid-span braces. In the V-type configuration, two braces connect to the top side of the frame beam somewhere along the clear span of the frame beam away from the beam-column joint. In the inverted V-type configuration, two braces connect to the bottom side of the frame beam somewhere along the clear span of the frame beam away from the beam-column joint. In some cases, the configuration is such that the braces form a two-story X-brace in a manner where both V-type and inverted V-type braces connect to the intermediate frame beam level. Figure 1 shows these three types of chevron configurations.

There are two common types of gusseted connections used in the types of brace configurations shown in Figure 1. A combined gusset, which is one plate that is used to connect both braces to the beam, or, when geometry permits, a single gusset can be used to connect each brace to the beam individually. Figures 2a and 2b show these two common types of gusset connections. The discussion presented in this

Patrick J. Fortney, Ph.D., P.E., S.E., P.Eng., President and Chief Engineer, Cives Engineering Corporation, Roswell, GA (corresponding). Email: pfortney@cives.com

William A. Thornton, Ph.D., P.E., NAE, Corporate Consultant, Cives Engineering Corporation, Roswell, GA. Email: bthornton@cives.com

paper focuses on combined gussets. However, it is important to recognize that the issues addressed in this paper apply equally to chevron braces connected with single gussets. The only significant difference between the two types of gussets is how the forces acting at the gusset-to-beam interface are calculated.

Unlike connection design for braces that frame to a beam-column joint, where the Uniform Force Method (UFM) is typically used to distribute brace forces through the connection, the force distribution in a chevron brace connection can be determined using any type of distribution that satisfies static equilibrium. Part 13 of the 14th edition AISC *Steel Construction Manual* (2011b) provides comprehensive guidance how to distribute forces in brace connections for braces that frame to a beam-column joint. However, there is very little published work on how to distribute brace forces in other types of brace configurations, such as V-type and inverted V-type brace configurations (see example problem II.C-5 of the AISC *Design Examples* Manual, v.14.1). A method for doing so is presented in this paper. The impact of the force distribution on the frame beam must also be considered. A thorough treatment on this topic is also presented.

In chevron brace connections, the algebraic sum of the vertical components of the brace forces can have a significant impact on the shear and moment distribution in the frame beam. When the sum of the vertical components of the brace forces is non-zero, the beam shear and moment distribution along the span of the beam are highly dependent on the span of the beam as well as the location of the work point along the span of the beam. Furthermore, the maximum beam shear and moment can be potentially underestimated or overestimated if the impact of the brace forces is evaluated as if the connection is isolated from the frame. Maximum beam shear and moment may also be located outside of the connection region of the beam. This impact on the beam is referred to in this paper as the chevron effect, and will be discussed in detail.

There are various reasons why the summation of the vertical components of the brace forces is non-zero. The most common reason involves mechanism analysis as required in seismic braced frame analysis and design. It is also possible to have a non-zero vertical component summation when braces are permitted to resist gravity loads simultaneous with a lateral load analysis.

This paper presents the following:

1. A procedure for determining an admissible force distribution within the connection.
2. The current typical method for determining beam shear.

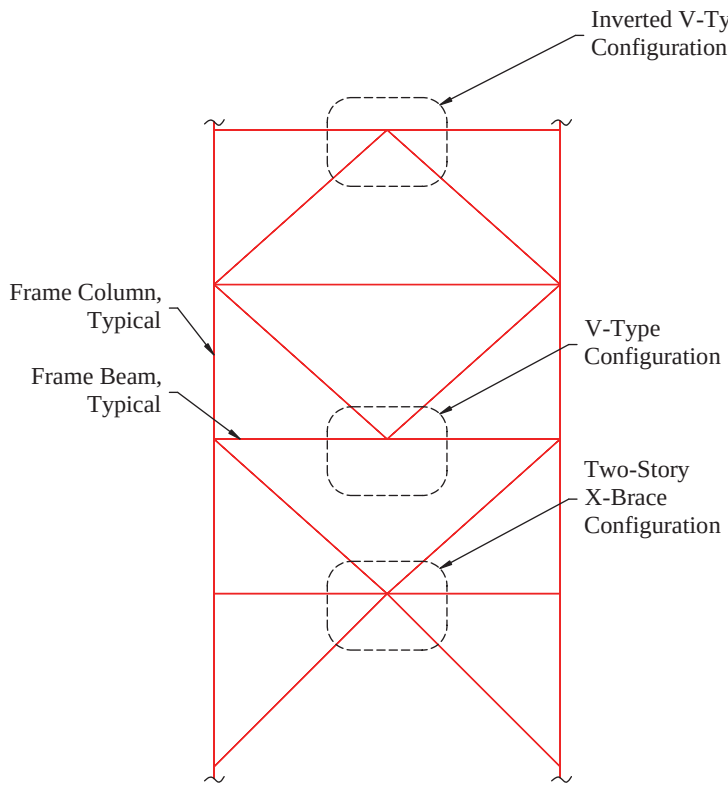

Fig. 1. V-type, inverted V-type and two-story X-braced frame configurations.

3. Distribution of forces acting on the beam-to-gusset interface.
4. Beam shear and moment distribution.
   a. The effect of the span of the beam.
   b. The effect of the location of the work point along the span of the beam.
5. The chevron effect.
6. A rule of thumb for estimating the moment acting at the gusset-to-beam interface.
7. Actual design problem.

Example problems to support the discussion are provided throughout the paper. It's worth noting that in this type of work, the calculated values part of the solutions are typically shown using three significant figures. However, in order to have beam shear and moment diagrams close nicely, the authors have chosen to present values with higher number of significant figures than would typically be presented.

1. AN ADMISSIBLE CHEVRON BRACE FORCE DISTRIBUTION

When generating an admissible force distribution in the connection, a control section must be selected. The method presented in this paper assumes a horizontal control section that is taken at the edge of the gusset that interfaces with the beam.

Horizontal Control Section

This method first evaluates the forces acting on the horizontal edge of the gusset adjacent to the frame beam. This section is referred to as section *a-a*. See Figure 3a for geometry and parameters used. Once the forces acting on section *a-a* are determined, a vertical section located at one-half of the gusset length, L_g, is cut. This section is referred to as section *b-b* (see Figures 3d and 3e). Each half of the gusset is evaluated. For each half-gusset body, the forces acting on the horizontal edge are taken as one-half of the forces acting on section *a-a*. The moment acting on section *a-a* is applied to the horizontal edge of the body as a couple and is taken as $2M_{a\text{-}a}/L_g$, as shown in Figures 3b and 3c. Figures 3d and 3e show the free body diagrams of each the half-gusset bodies.

Note that the analysis considers brace bevels, brace forces and the effects of any eccentricities that may exist in both the horizontal and vertical directions. The eccentricity, Δ, accounts for variations between brace 1 and brace 2 bevels and the vertical components of the brace forces. The eccentricity resulting from the horizontal components delivered by the gusset to the beam flange is accounted for with the parameter e_b. The sign convention used assumes that a brace force component is positive when acting to the right in the horizontal direction and when acting upward in the vertical direction. A clockwise moment is considered to be positive. It is important to recognize that this is not the only way this analysis can be approached.

The equations derived from statics for the forces and moments acting on sections *a-a* and *b-b* using the approach shown in Figure 3 will be derived in their entirety.

Referring to Figure 3a, the vertical eccentricity parameter, Δ can be written as,

$$\Delta = \frac{1}{2}(L_1 - L_2) \tag{1}$$

Note that Δ is positive when to the left of the work point.

Forces Acting on Section a-a

Referring to Figure 3b, equations for the forces and moment acting on section *a-a* can be written using the three equations of equilibrium. In these equations, the subscripts 1 and 2 refer to the brace forces from the left and right braces,

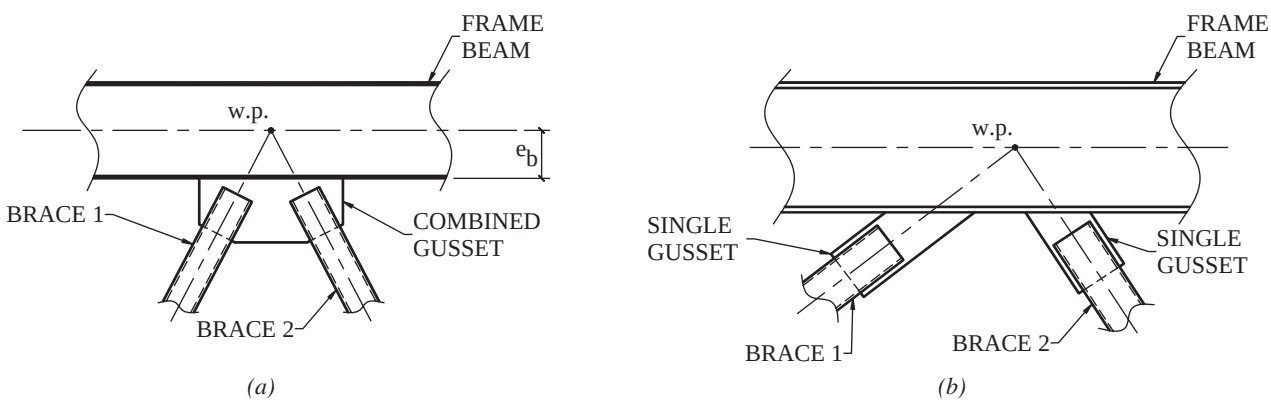

Fig. 2. Representative sketches of combined and single chevron gusset plates: (a) combined gusset; (b) single gusset.

respectively. The subscripts *H* and *V* refer to forces acting in the horizontal and vertical directions, respectively. The subscript *w.p.* refers to the work point, and the subscript *a-a* refers to section *a-a* as shown in Figure 3.

$$\begin{aligned}
\sum F_H &= 0 = H_{a-a} + H_1 + H_2 \\
H_{a-a} &= -(H_1 + H_2) \\
\sum F_V &= 0 = V_{a-a} + V_1 + V_2 \\
V_{a-a} &= -(V_1 + V_2) \\
\sum M_{w.p.} &= 0 = -(V_1 + V_2)(\Delta) + (H_1 + H_2)e_b + M_{a-a} \\
M_{a-a} &= (V_1 + V_2)\Delta - (H_1 + H_2)e_b
\end{aligned}$$

In summary, the forces and moments acting on section *a-a* are as given in Equations 2, 3 and 4.

$$H_{a-a} = -(H_1 + H_2) \tag{2}$$

$$V_{a-a} = -(V_1 + V_2) \tag{3}$$

$$M_{a-a} = (V_1 + V_2)\Delta - (H_1 + H_2)e_b \tag{4}$$

Force Acting on Section* b-b *(left half of the gusset)

Referring to Figure 3d, equations for the forces and moment acting on section *b-b* at the left half of the gusset can be written using the three equations of equilibrium. As discussed previously, note that the forces acting on the horizontal section of the left half gusset are taken as one-half of the total forces acting on section *a-a*. Also, the moment M_{a-a} is converted to a couple acting at $L_g/4$ of the gusset on both the left and right halves of the gusset. In the following derivations, the subscript *b*1 refers to forces and moments acting on section *b-b* due to the brace force from brace 1. Refer to Figure 3d.

$$\begin{aligned}
\sum F_H &= 0 \\
&= H_{b1} + H_1 - \frac{1}{2}(H_1 + H_2) \\
H_{b1} &= \frac{1}{2}(H_1 + H_2) - H_1 \\
\sum F_V &= 0 = V_{b1} + V_1 - \frac{1}{2}(V_1 + V_2) + \frac{2M_{a-a}}{L_g} \\
V_{b1} &= \frac{1}{2}(V_1 + V_2) - \frac{2M_{a-a}}{L_g} - V_1 \\
\sum M_b &= 0 \\
&= M_{b1} + H_1\left(e_b + \frac{h}{2}\right) - V_1 \quad + \frac{2M_{a-a}}{L_g}\left(\frac{L_g}{4}\right) \\
&\quad -\frac{1}{2}(V_1 + V_2)\left(\frac{L_g}{4}\right) - \frac{1}{2}(H_1 + H_2)\left(\frac{h}{2}\right)
\end{aligned}$$

$$\begin{aligned}
M_{b1} &= \frac{L_g}{8}(V_1 + V_2) + \frac{h}{4}(H_1 + H_2) \\
&\quad -\frac{M_{a-a}}{2} + V_1\Delta - H_1\left(e_b + \frac{h}{2}\right)
\end{aligned}$$

The couple, N_{eq}, of the moment, M_{a-a}, shown in Figures 3d and 3e is given in Equation 5.

$$N_{eq} = \frac{2M_{a-a}}{L_g} \tag{5}$$

In summary, the forces and moment acting on section *b-b* from the perspective of the left half of the gusset are as given in Equations 6, 7 and 8.

$$H_{b1} = \frac{1}{2}(H_1 + H_2) - H_1 \tag{6}$$

$$V_{b1} = \frac{1}{2}(V_1 + V_2) - \frac{2M_{a-a}}{L_g} - V_1 \tag{7}$$

$$\begin{aligned}
M_{b1} &= \frac{L_g}{8}(V_1 + V_2) + \frac{h}{4}(H_1 + H_2) \\
&\quad -\frac{M_{a-a}}{2} + V_1\Delta - H_1\left(e_b + \frac{h}{2}\right)
\end{aligned} \tag{8}$$

Forces Acting on Section* b-b *(right half of the gusset)

Referring to Figure 3e, equations for the forces and moment acting on section *b-b* at the right half of the gusset can be written using the three equations of equilibrium. As discussed previously, note that the forces acting on the horizontal section of the right half gusset are taken as one-half of the total forces acting on section *a-a*. In the following derivations, the subscript *b*2 refers to forces and moments acting on section *b-b* due to the brace force from brace 2. Refer to Figure 3e.

$$\begin{aligned}
\sum F_H &= 0 \\
&= H_{b2} + H_2 - \frac{1}{2}(H_1 + H_2) \\
H_{b2} &= \frac{1}{2}(H_1 + H_2) - H_2 \\
\sum F_V &= 0 \\
&= V_{b2} + V_2 - \frac{2M_{a-a}}{L_g} - \frac{1}{2}(V_1 + V_2) \\
V_{b2} &= \frac{1}{2}(V_1 + V_2) + \frac{2M_{a-a}}{L_g} - V_2
\end{aligned}$$

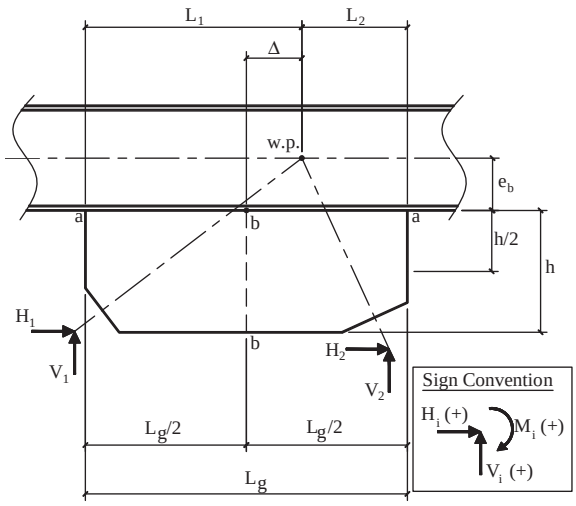

(a) Geometry, parameters and sign convention

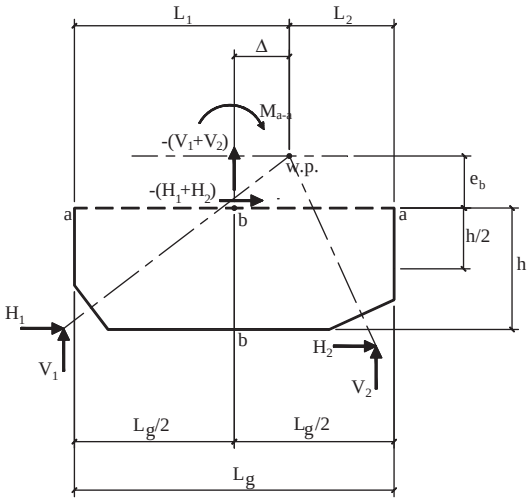

(b) Forces and moment on section a-a

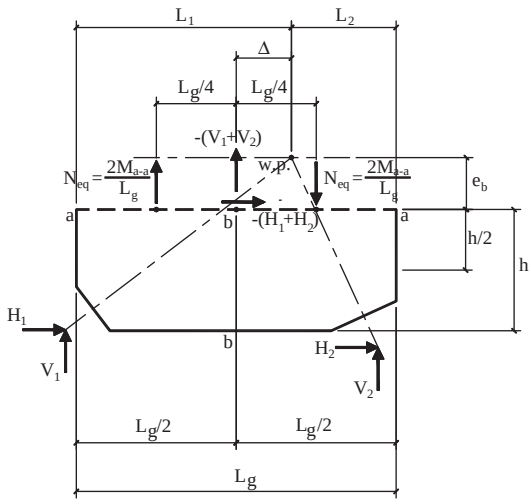

(c) Equivalent forces on section a-a

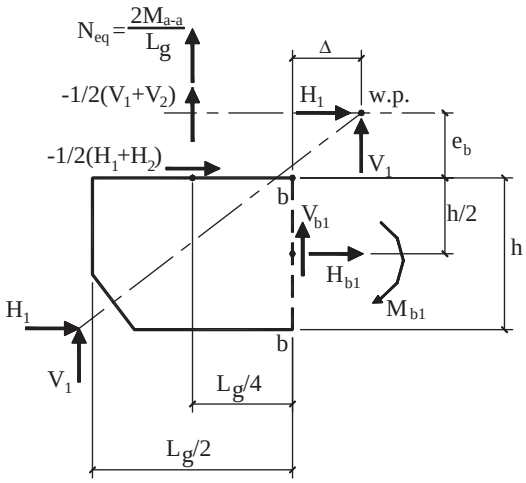

(d) Forces on left half of gusset

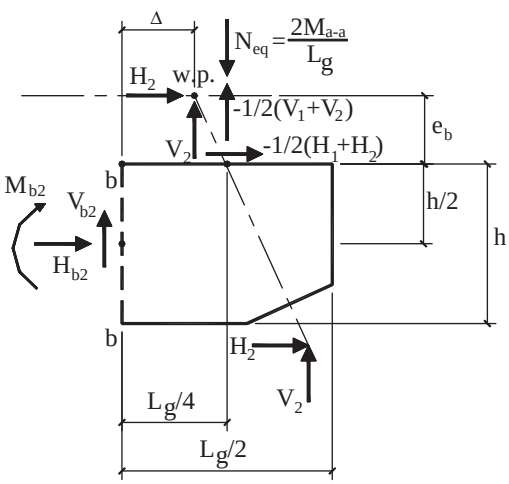

(e) Forces on right half of gusset

Fig. 3. Free body forces on critical horizontal and vertical gusset sections.

$$\sum M_b = 0$$

$$= M_{b2} + H_2\left(e_b + \frac{h}{2}\right) - V_2\Delta + \frac{2M_{a-a}}{L_g}\left(\frac{L}{4}\right)$$

$$+ \frac{1}{2}(V_1 + V_2)\left(\frac{L_g}{4}\right) - \frac{1}{2}(H_1 + H_2)\left(\frac{h}{2}\right)$$

$$M_{b2} = -\frac{L_g}{8}(V_1 + V_2) + \frac{h}{4}(H_1 + H_2)$$

$$-\frac{M_{a-a}}{2} + V_2\Delta - H_2\left(e_b + \frac{h}{2}\right)$$

In summary, the forces and moments acting on section *b-b* from the perspective of the right half of the gusset are as given in Equations 9, 10 and 11.

$$H_{b2} = \frac{1}{2}(H_1 + H_2) - H_2 \tag{9}$$

$$V_{b2} = \frac{1}{2}(V_1 + V_2) + \frac{2M_{a-a}}{L_g} - V_2 \tag{10}$$

$$M_{b2} = -\frac{L_g}{8}(V_1 + V_2) + \frac{h}{4}(H_1 + H_2) \tag{11}$$

$$-\frac{M_{a-a}}{2} + V_2\Delta - H_2\left(e_b + \frac{h}{2}\right)$$

Example 1: Brace Force Distribution

Figure 4 shows the chevron connection geometry and dimensions. The force distributions acting on sections *a-a* and *b-b* will be determined using Equations 1 through 4 and 6 through 8, respectively. Equation 5 will be used to calculate the couple of the moment, $M_{a\text{-}a}$.

The variables for Example 1 are shown below. Note the signs of the component brace forces and the calculation of Δ. Using the assumed sign convention, a component force acting to the right in the horizontal direction, or upward in the vertical direction, is positive. The vertical eccentricity parameter, Δ, is calculated as shown in Equation 1. In this solution, the forces acting on section *b-b* are calculated using the left-half gusset body (Equations 6, 7 and 8). Note that the right-half gusset body (Equations 9, 10 and 11) can be used just as easily giving the same results.

L_g = 70.63 in., L_1 = 44.56 in., L_2 = 26.06 in.

e_b = 9.75 in., h = 22.75 in.

$$\Delta = \frac{1}{2}(44.56 \text{ in.} - 26.06 \text{ in.}) = 9.25 \text{ in.}$$

H_1 = –338.6 kips

H_2 = –163.6 kips

V_1 = –225.8 kips

V_2 = 150.0 kips

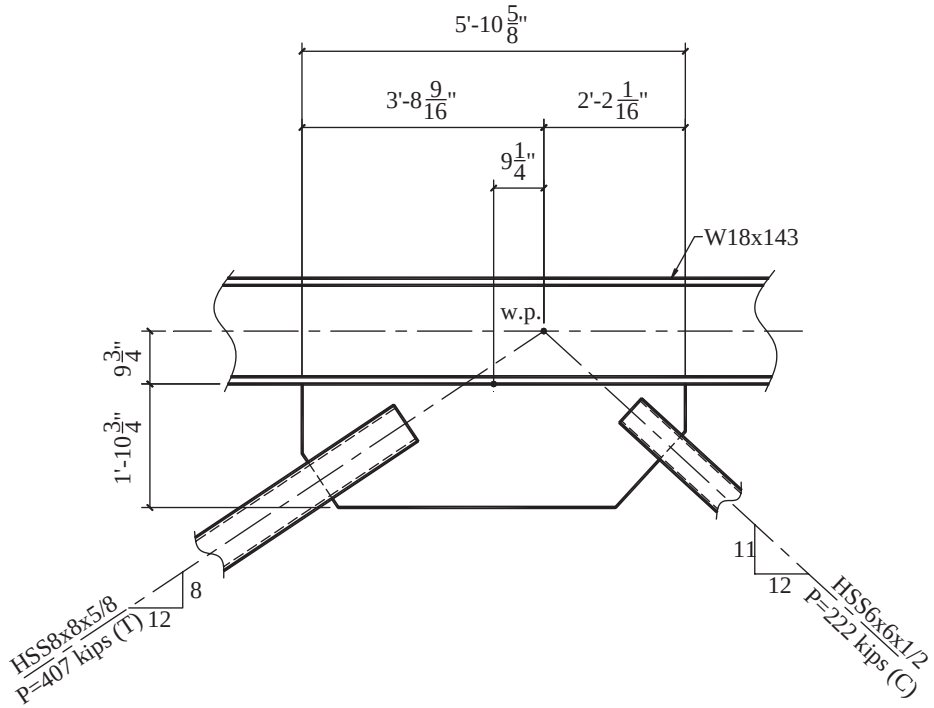

Fig. 4. Geometry and dimensions for Example 1.

Forces acting on section* a-a*:

$$H_{a-a} = -(H_1 + H_2) = -(-338.6 - 163.6)$$
$$= 502 \text{ kips}$$
$$V_{a-a} = -(V_1 + V_2) = -(-225.8 + 150)$$
$$= 75.8 \text{ kips}$$
$$M_{a-a} = (V_1 + V_2)\Delta - (H_1 + H_2)e_b$$
$$= (-225.8 + 150)(9.25) - (-338.6 - 163.6)(9.75)$$
$$= 4{,}195 \text{ kip-in}$$

Forces acting on section* b-b*:

$$H_{b-b} = H_{b1}$$
$$= \frac{1}{2}(H_1 + H_2) - H_1$$
$$= \frac{1}{2}(-338.6 - 163.6) - (-338.6) = 87.5 \text{ kips}$$

$$V_{b-b} = V_{b1}$$
$$= \frac{1}{2}(V_1 + V_2) - \frac{2M_{a-a}}{L} - V_1$$
$$= \frac{1}{2}(-225.8 + 150) - \frac{(2)(4{,}195)}{70.63} - (-225.8)$$
$$= 69.1 \text{ kips}$$
$$M_{b-b} = M_{b1}$$
$$= \frac{L}{8}(V_1 + V_2) + \frac{h}{4}(H_1 + H_2) - \frac{M_{a-a}}{2}$$
$$+ V_1\Delta - H_1\left(e_b + \frac{h}{2}\right)$$
$$= \frac{70.63}{8}(-225.8 + 150) + \frac{22.75}{4}(-338.6 - 163.6)$$
$$- \frac{4{,}195}{2} + (-225.8)(9.25) - (-338.6)(21.13)$$
$$= -559 \text{ kip-in.}$$

The free body diagrams are shown in Figure 5.

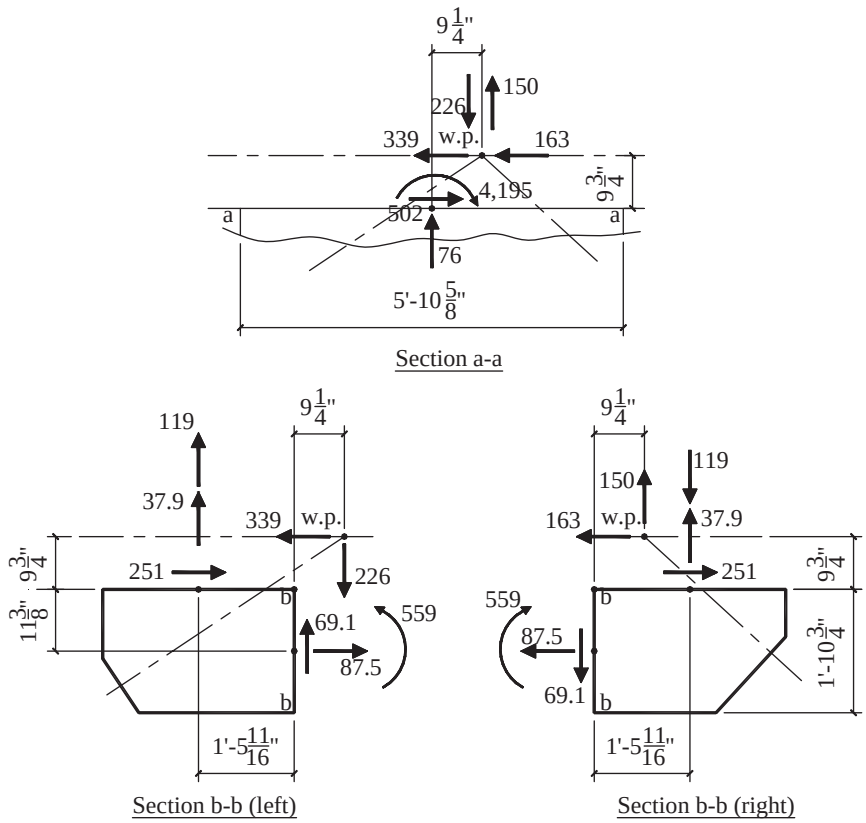

Fig. 5. Free body diagrams for Example 1.

2. CURRENT METHOD USED FOR BEAM SHEAR DETERMINATION

Typically, the shear imparted to the beam by the brace force distribution is evaluated as if the connection is isolated from the frame. The beam span and the location of the work point along the span of the beam are not considered. Consider the joint shown in Figure 6, where the brace bevels are equal, the magnitude of the brace forces are equal and one brace is in tension while the other is in compression. Using the procedure presented previously, the forces acting at the gusset-to-beam interface are given in Figure 7. Without considering the span of the beam or the location of the work point along the span of the beam, the shear in the beam, V_{beam}, is constant between the two points of applied load and would be taken as the $M_{a\text{-}a}$ couple of 60.94 kips ($M_{a\text{-}a}$ = 96.49 k-ft, L_g = 3 ft, 2 in.). The moment in the beam would be taken as one-half of the area under that shear gradient, which would be that given in Equation 12. It's worth noting that evaluating the shear demand on the beam would typically be a consideration to determine if the beam required a web doubler in the connection region. Beam moment in the connection region is not typically considered. The beam moment in the connection region is calculated as given in Equation 12.

$$M_{beam} = \frac{V_{beam} L_g}{4} \tag{12}$$

It is no coincidence that Equation 12 is equivalent to one-half of the summation of the horizontal components of the brace forces times one-half the beam depth as given by Equation 13. Figure 8 shows the beam shear and moment distribution resulting from the forces acting on section *a-a*.

$$M_{beam} = \frac{\sum H_i e_b}{2} \tag{13}$$

With the type of configuration and forces shown in Figures 6 through 8, the impact of the brace forces on the beam is determined to be V_{beam} = 60.94 kips and M_{beam} = 48.24 kip-ft, when the connection is evaluated as if it is isolated from the frame. Is this isolated evaluation adequate? Should the span of the beam, and the location of the work point, be considered? Before addressing these questions, we first have to consider how the forces acting on section *a-a* will be assumed to be distributed for the evaluation of the load effects on the beam.

3. GUSSET-TO-BEAM INTERFACE FORCE DISTRIBUTION

For the analysis and design of the gusset and the gusset-to-beam weld, the normal forces acting on the beam are assumed to be distributed uniformly along the gusset-to-beam interface length. The horizontal forces, $H_{a\text{-}a}$, are assumed to act on the interface eccentrically with a lever arm equal to e_b, as discussed previously. When a normal force, $V_{a\text{-}a}$ is present, the normal force is assumed to be distributed uniformly along the gusset-to-beam interface length. The moment at the interface, $M_{a\text{-}a}$, is assumed to act as distributed tension/compression normal forces equal to the couple of $M_{a\text{-}a}$ (see

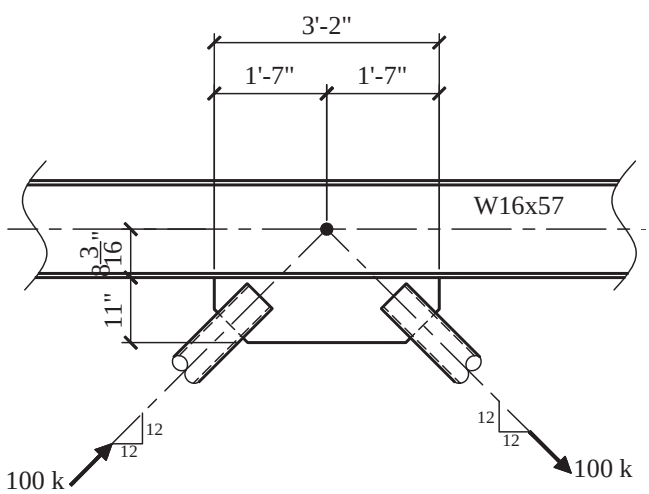

Fig. 6. Equal brace bevels and forces in a compression-tension brace arrangement.

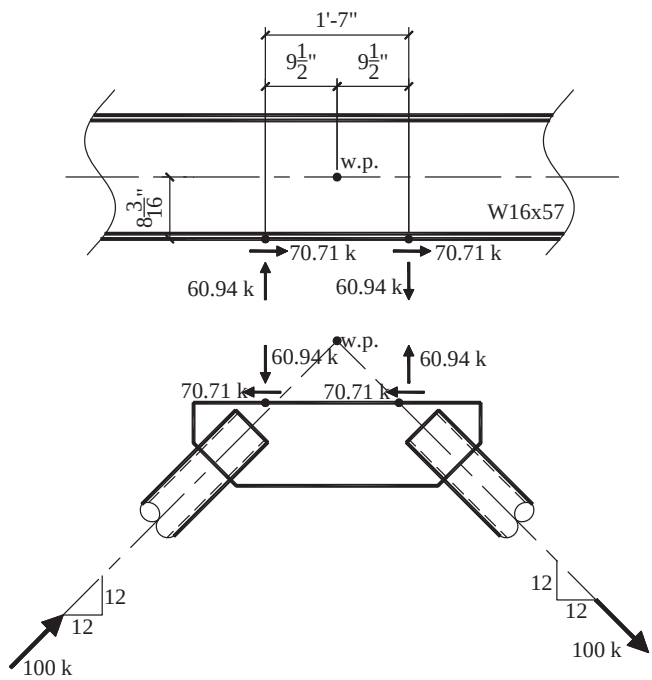

Fig. 7. Forces acting on section a-a *for connection shown in Figure 6.*

Equation 5) divided by one-half the gusset length, $L_g/2$ (see Equation 14). Figure 9 shows the force distributions that are typically assumed for the gusset plate design and the design of the gusset-to-beam weld.

$$n_{eq} = \frac{\frac{2M_{a-a}}{L_g}}{\frac{L_g}{2}} = \frac{4M_{a-a}}{L_g^2} \tag{14}$$

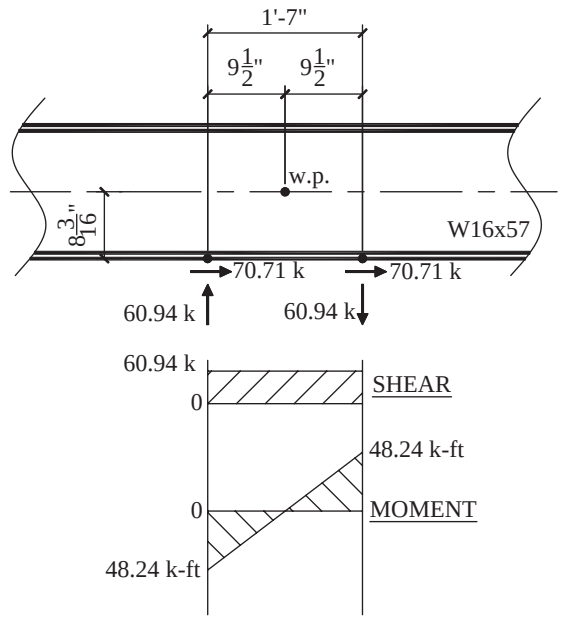

Fig. 8. Beam shear and moment distribution for the isolated connection shown in Figure 6.

The forces and moment acting on the gusset-to-beam interface are treated as externally applied loads to evaluate beam shear and moment. The distributions of these interface forces can be uniformly distributed as shown in Figure 9. However, using these distributions can be tedious when evaluating beam shear and moment distribution. To simplify the beam analysis, it is recommended that the resultant force like those shown in Figure 5 be used to evaluate the beam. The following is an example to illustrate the differences between the two methods of beam evaluation (i.e., the distributed method versus the resultant method).

Suppose the connection presented in Example 1 is part of a frame with a beam spanning 25 ft, and the work point is located 15 ft 6 in. from the left support, as shown in Figure 10a. The forces acting on the gusset-to-beam interface can be assumed to be distributed uniformly along the length of the interface, as shown in the loading diagram in Figure 11, or as resultant forces acting at the centroids of the two half gusset bodies, as shown in Figure 12. The beam shear and moment distributions along the length of the beam are shown in Figures 11 and 12 for each method, respectively. As can be seen in the two figures, the beam shear and moment gradients are a little different as a result of the types of loads. Both loading conditions produce the same maximum beam shear, and the maximum beam shears are located at the same locations. The maximum moment, for this example, is about 37% larger when the resultant loads are used and occurs within the connection region. The conservativeness in the maximum moment calculation using the resultant method can be attributed to two facts:

1. The beam end reactions are the same regardless of which method is used. However, the area under the shear gradient is larger using the resultant loads because the length of the gradient interval is longer. For example, the left support reactions using both methods is 28.83 kips, as can be seen in Figures 11 and 12. The

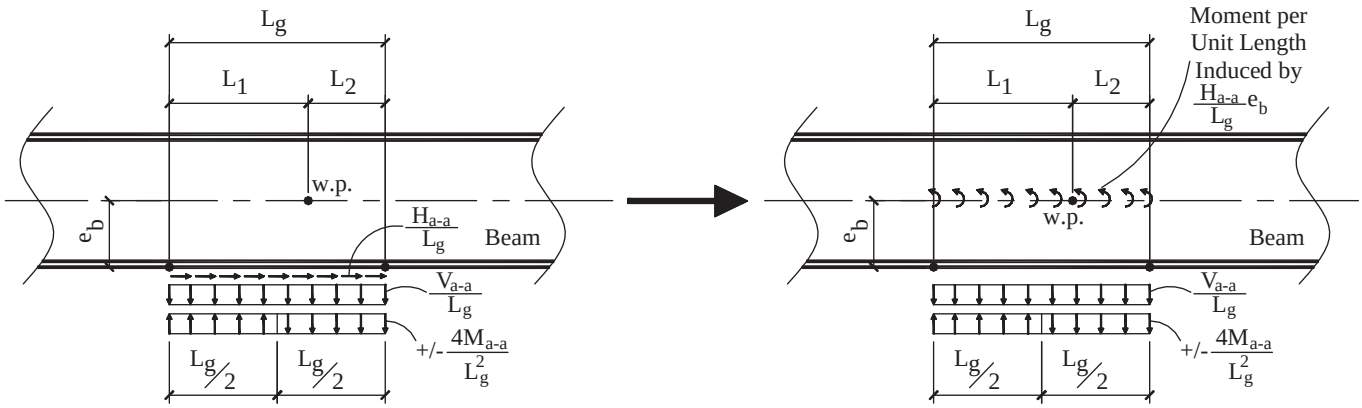

Fig. 9. Interface forces uniformly distributed.

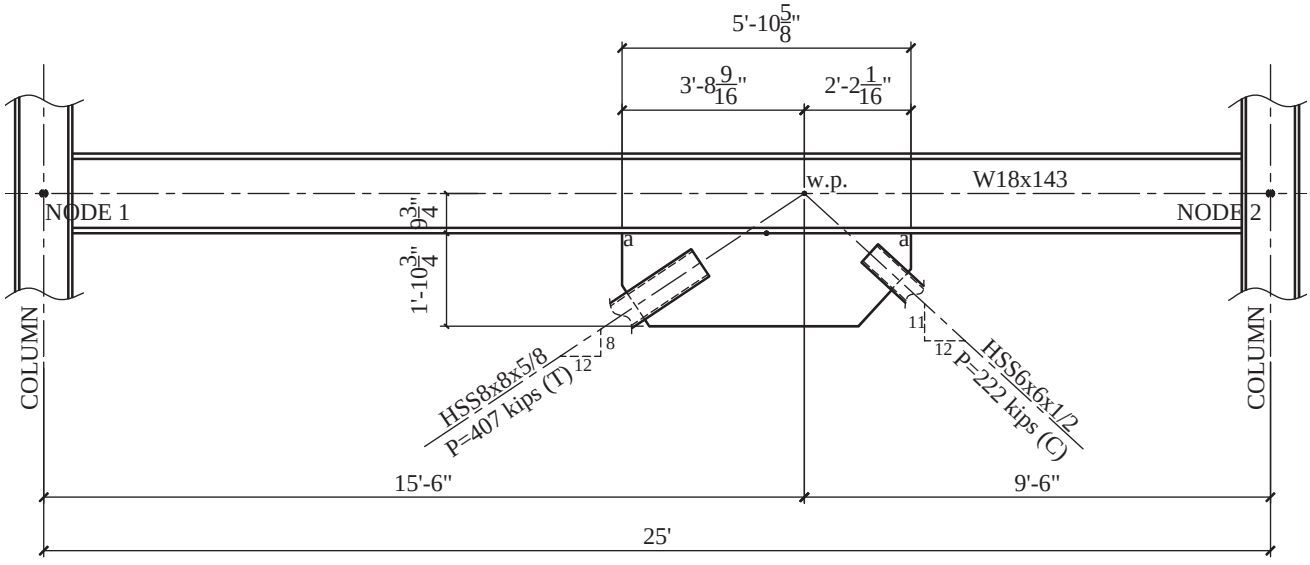

(a)

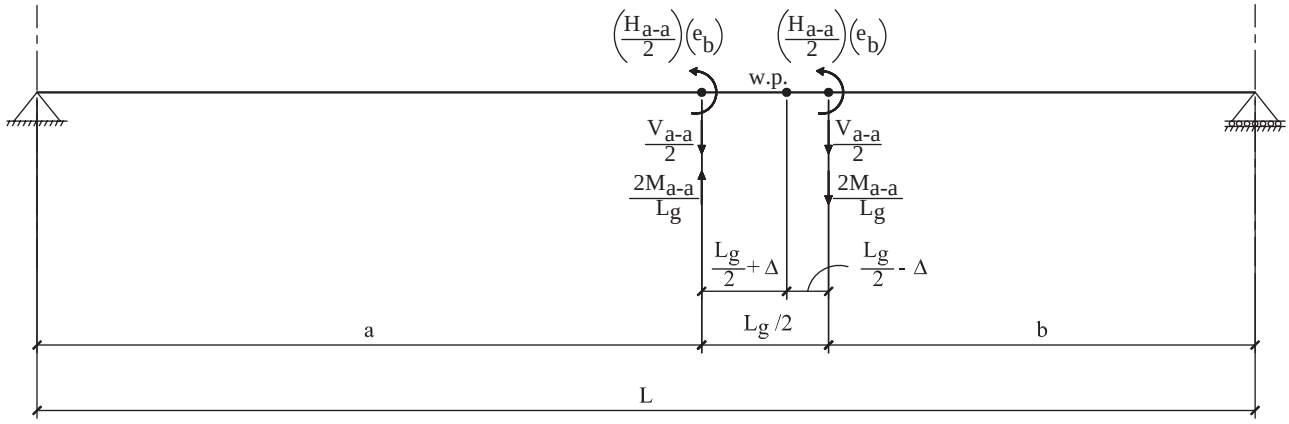

(b)

Fig. 10. (a) Gusset connection shown in Figure 5 in context of a frame; (b) beam model: resultant force loading and boundary conditions.

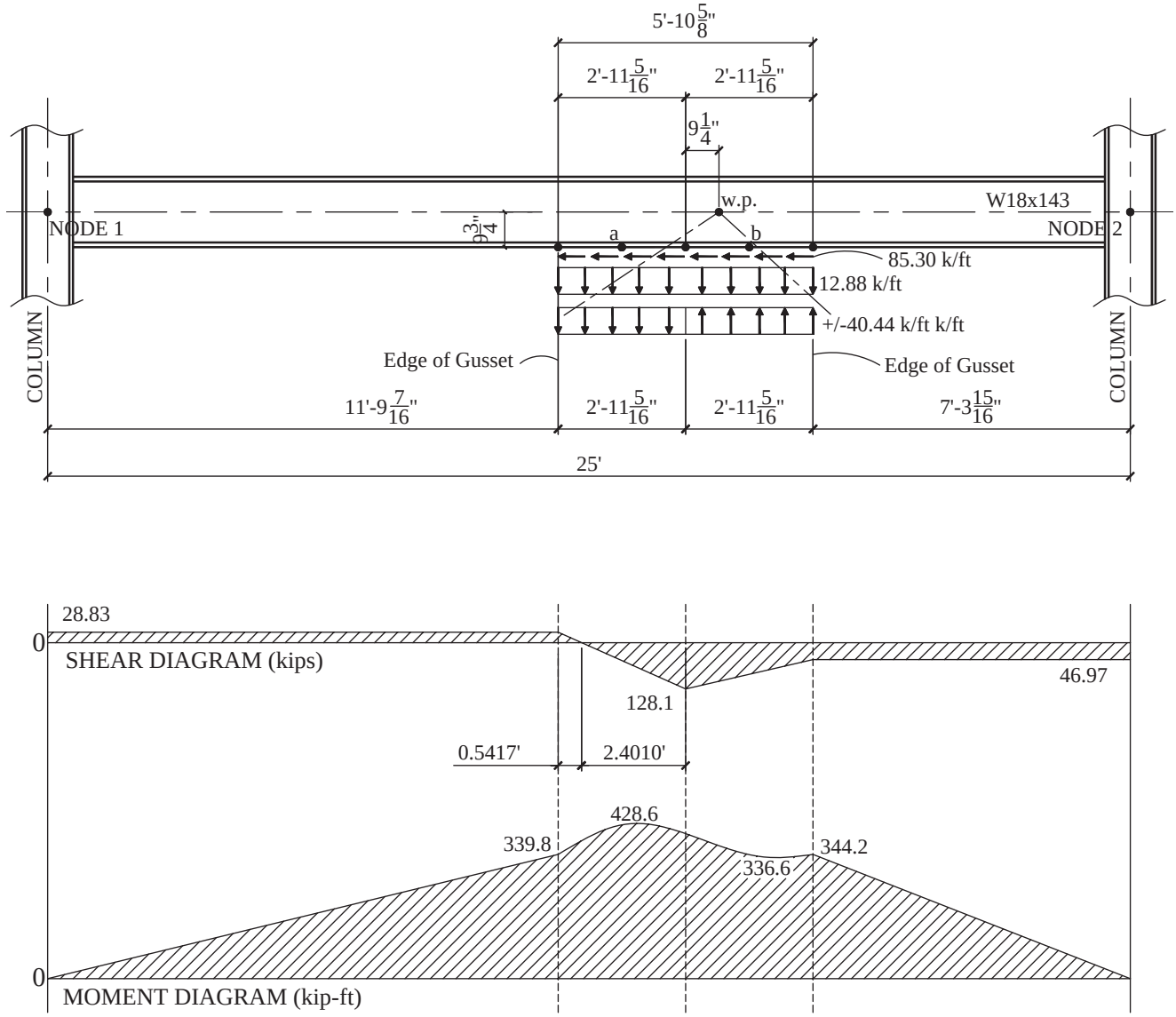

Fig. 11. Beam shear and moment with uniformly distributed loads acting on interface.

distance from the left support to the change in loading in Figure 11 is the distance to the left edge of the gusset (11 ft 9⁷⁄₁₆ in.) assuming distributed load; the distance from the left support to the change in loading in Figure 12 is the distance to the centroid of the left half gusset body (13 ft 3⅛ in.). The difference between the two distances is ¼ of the gusset length, L_g. Thus, the longer the gusset, the more conservative the moment calculation will be when using resulting loads.

2. The concentrated moment using the resultant method is more conservative relative to distributing the moment over the entire length of the gusset.

Given that using resultant loads gives the same beam end reactions and maximum beam shears (for most cases), that the calculated moment will always be conservative and that the resultant load method is far simpler relative to assuming distributed loads, resultant loads will be used throughout this discussion and in the example problems presented, except for beam web doubler plate detailing where the distributed loads are used. Figure 10b shows the general beam model that will be used to determine beam shear and moment distribution for beam evaluations.

Note that both methods give the same maximum beam shear in this example. However, it should be noted that when braces frame to both the top and bottom of the beam, and the Δ parameter is non-zero, it is possible that the resultant load method will produce a slightly larger maximum beam shear. The resultant load method will be conservative when comparing required beam shear strength to available beam shear strength. However, when the required beam shear strength exceeds the available beam shear strength, the distributed load method should be used to determine required web doubler thickness as well as the extent of the required beam web

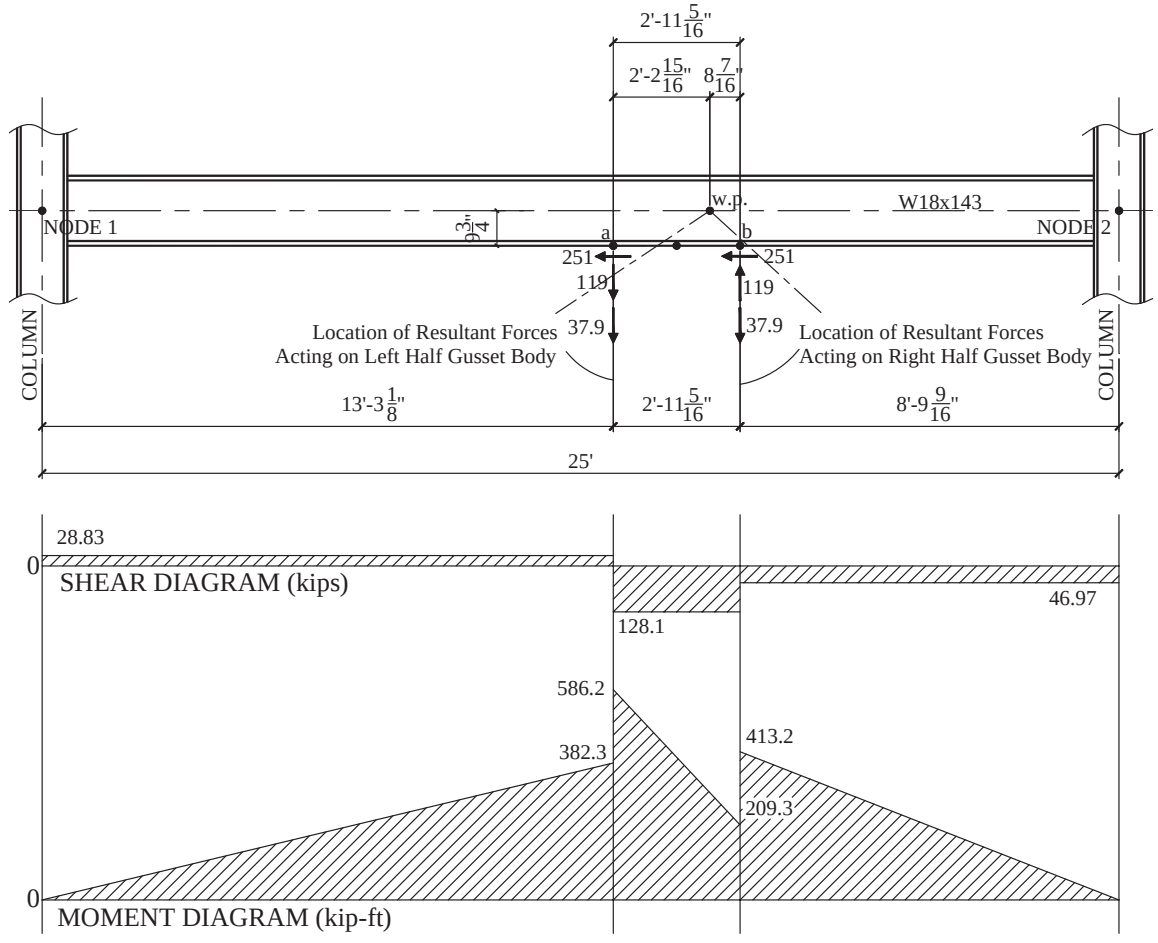

Fig. 12. Beam shear and moment with resultant forces acting at interface.

doubler plate. An example of how to detail a beam web doubler plate is provided in Part 4 of Example 3 presented later in this paper.

4. BEAM SHEAR AND MOMENT DISTRIBUTION

As discussed previously, the shear and moment imparted to the frame beam by the brace forces is typically evaluated as if the connection joint is isolated from the frame. Is this a valid approach, or does the span of the beam and the location of the work point along the span of the beam need to be considered when evaluating the brace load effects on the frame beam? If the algebraic sum of the vertical components of the brace forces is zero, shear and moment imparted to the beam is independent of the span of the beam and the location of the work point. If the algebraic sum of the vertical components of the brace forces is non-zero, the shear and moment imparted to the beam is dependent on the span of the beam and the location of the work point.

Figures 13a and 13b show a W16×57 spanning 28 ft. The brace geometry and forces are such that the algebraic sum of the vertical components of the brace forces is zero. Figure 13a has the work point located at mid-span of the beam, while Figure 13b has the work point located 6 ft (for simplicity, the brace bevels are assumed unchanged to illustrate a point) from the right support. Figures 14 and 15 show the beam shear and moment diagrams for the two work point locations, respectively. Referring to Figures 14 and 15, it can be observed that the beam shear and moment imparted to the beam is contained within the connection region. Beam

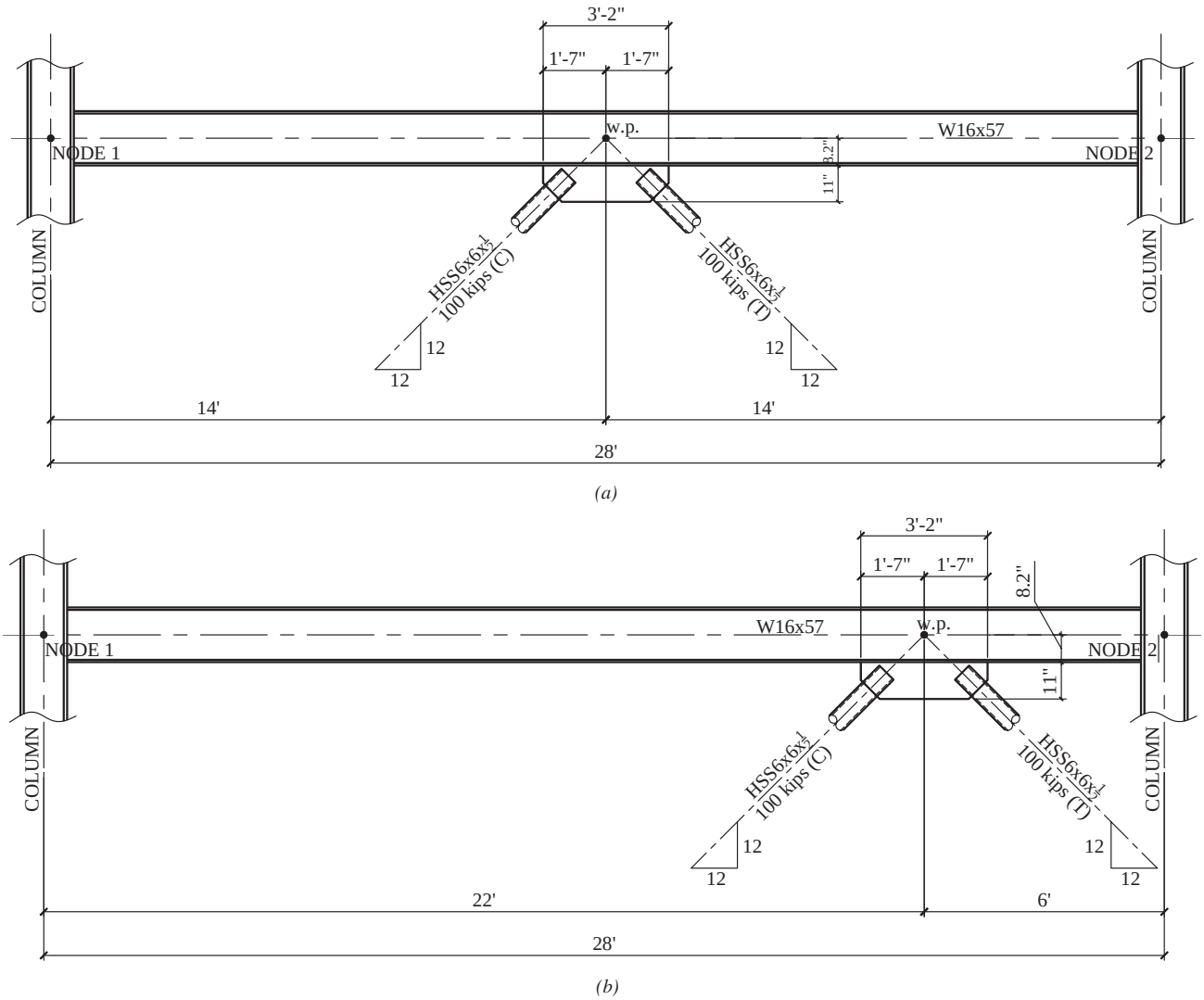

Fig. 13. $\Sigma V_i = 0$ at different locations along beam span: (a) connection located at mid-span; (b) connection located 6 ft from right support.

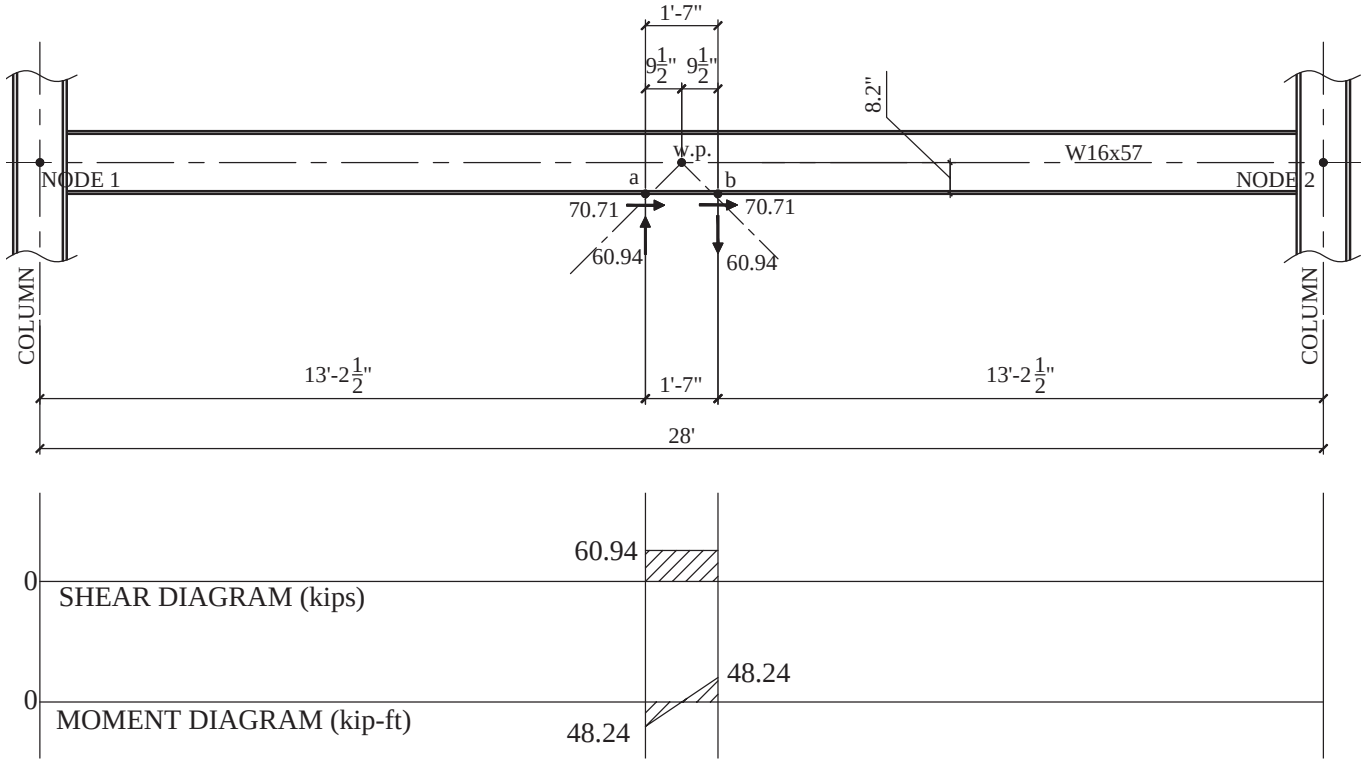

Fig. 14. $\Sigma V_i = 0$; *beam shear and moment with work point at mid-span.*

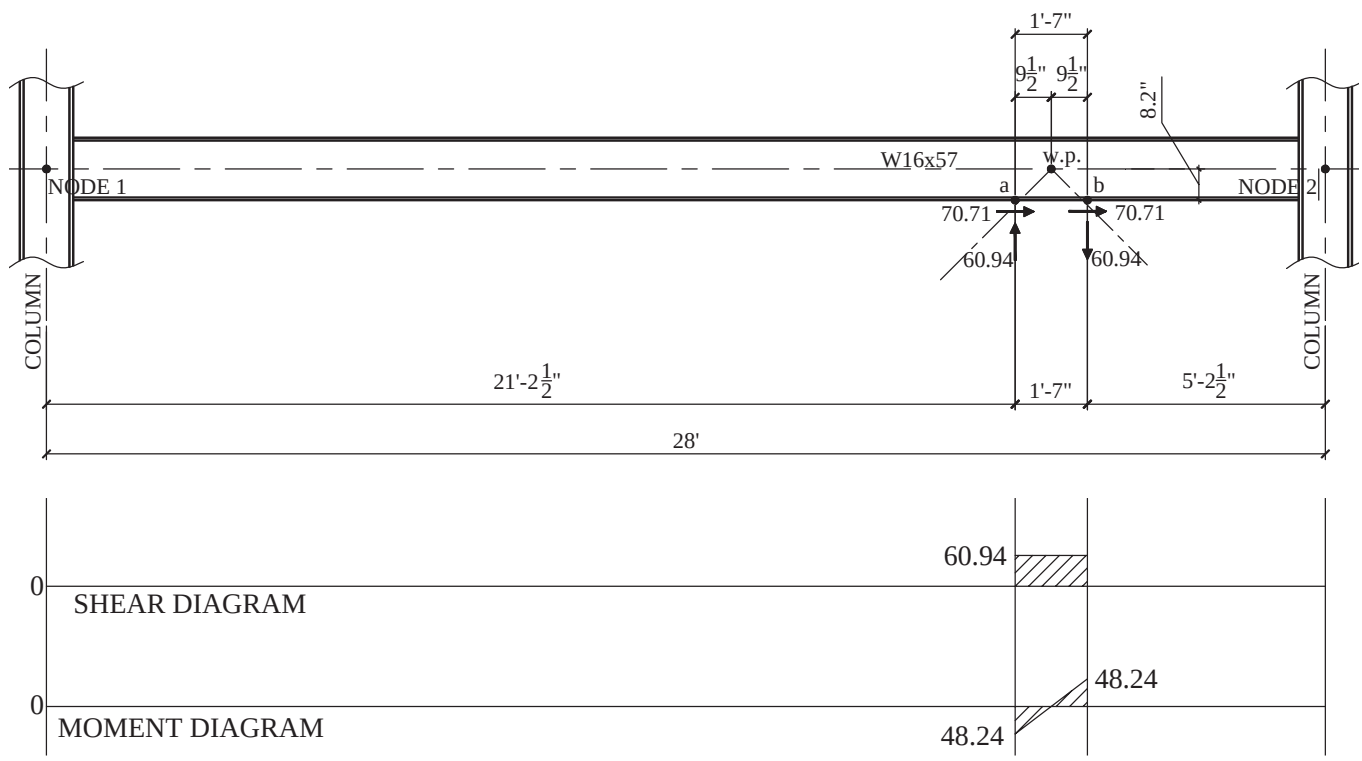

Fig.15. $\Sigma V_i = 0$; *beam shear and moment with work point off mid-span.*

shear and moment outside of the connection region is zero. If the connection was evaluated as if the joint was isolated from the frame, the beam shear and moment would be the same as that shown in Figures 14 and 15. Thus, the shear and moment imparted to the beam by the brace forces is independent of the beam span and the location of the work point along the beam span. Therefore, when the algebraic sum of the vertical components of the brace forces is zero, it is sufficient to evaluate the beam as if the connection is isolated from the frame. Historically, this is probably the reason that this type of connection has been designed in isolation.

Now consider that the tension brace force shown in Figure 13 is increased from 100 kips to 300 kips while the compression brace force remains at 100 kips, as shown in Figures 16a and 16b. The algebraic sum of the vertical components of the brace forces is now non-zero. The summation of the vertical components of the brace forces is 141.2 kips. Figures 16a and 16b show the geometry and forces for these cases. Figures 17 and 18 show the beam shear and moment diagrams for the case where the work point is at mid-span and when the work point is 6 ft from the right support. As can be seen in Figures 17 and 18, the location of the work

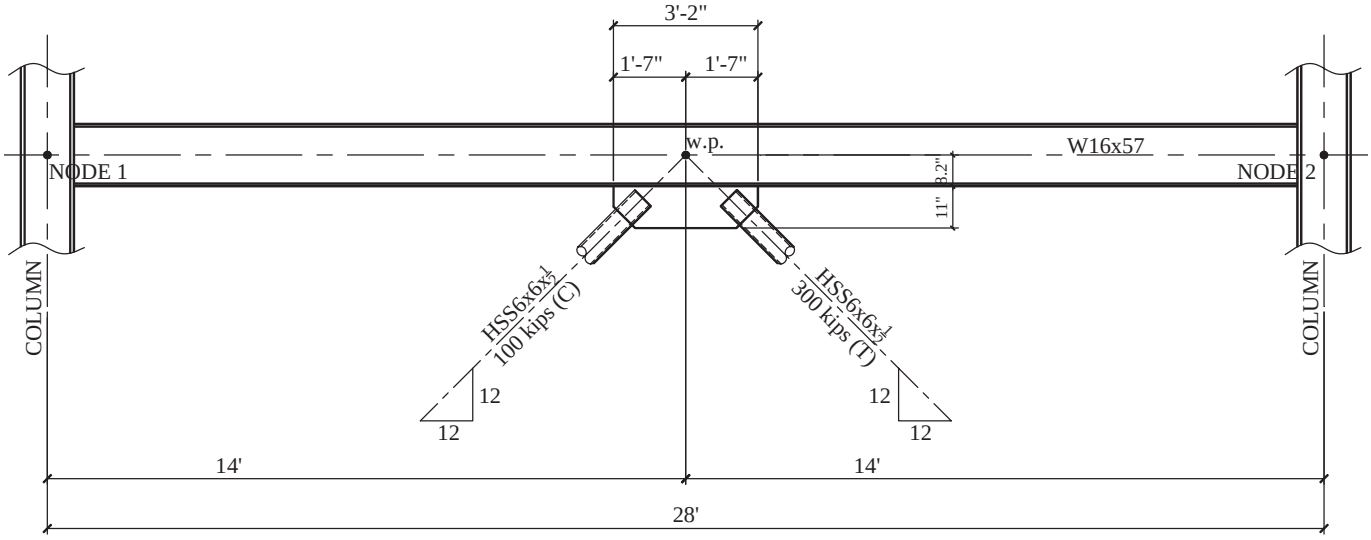

(a)

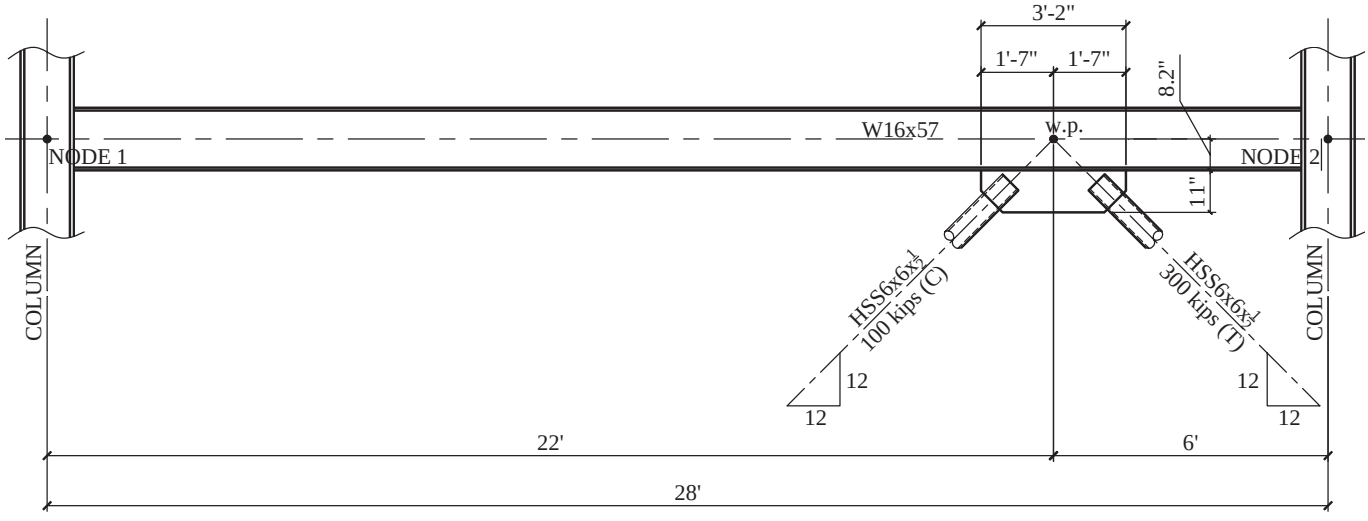

(b)

Fig. 16. $\Sigma V_i \neq 0$ (141.2 kips) at different locations along beam span: (a) connection located at mid-span; (b) connection located 6 ft from right support.

point has an effect on how the beam shear and moment are distributed along the length of the beam and has an effect on the maximum beam shears and moments.

Referring to the beam shear diagram in Figure 17, it can be seen that the beam shear within the connection region is equal to the couple of the moment, $M_{a\text{-}a}$ (in this case, 122.1 kips), and the shear outside of the connection region is equal to one-half of the algebraic sum of the vertical components of the brace forces (in this case, 70.6 kips). This may lead one to conclude that this is always the case when there is an unbalanced vertical force and the work point is at mid-span of the beam. However, this is not always the case; there is one other parameter that must be satisfied. The centroid of the gusset interface must also be vertically aligned with the work point. In other words, the parameter Δ must be zero. For the beam shear within the connection region to be equal to the couple, and the shear outside of the connection region to be equal to one-half of the unbalanced force, the work point must be located at mid-span of the beam and the parameter Δ must be equal to zero. This will also be true if Δ is non-zero but the centroid of the gusset happens to be vertically aligned with the mid-span work point. Simply put, this is only true when the resultant normal forces acting on the interface are symmetric about the mid-span work point.

Comparing the beam shear distributions shown in Figures 17 and 18, it can be concluded that the beam shear and moment distribution, as well as the maximum shear and moment, are dependent on the location of work point along the span of the beam. If the beam shear and moment are evaluated as if the connection is isolated from the frame, the beam shear and moment would be determined to be 122.1 kips and 96.7 kip-ft, respectively, regardless of the beam span and the location of the work point along the span of the beam (refer to previous discussion). If the beam shear and moment are evaluated considering the frame, with the work point at mid-span, the maximum beam shear and moment is 122.1 kips and 1,030 k-ft, respectively. The beam shears are the same because the resultant normal forces are symmetric about the work point. However, the beam moment is 1,030/96.7 = 10.6 times larger when the frame is considered. When the frame is considered and the work point is not at mid-span (6 ft from the right support in this case), the maximum beam shear and moment is 111.0 kips and 674.4 k-ft (see Figure 18). The maximum beam shear is overestimated by 122.1/111.0 = 1.10 times and the moment is underestimated by 674.4/96.7 = 7.97 times when the frame is considered. Furthermore, as can be seen in Figure 18, the maximum beam shear occurs outside of the connection region. This would not be noticed if the beam shear is evaluated as if the connection is isolated from the frame—a problematic issue if one was to evaluate the need for web doubler plates and the location where such reinforcement would be required.

The effect of the location of the work point has been illustrated in Figures 17 and 18. The span of the beam also has an effect on the beam shear and moment distribution. Although not illustrated in this discussion, one can deduce that a change in beam span has an effect on the beam end

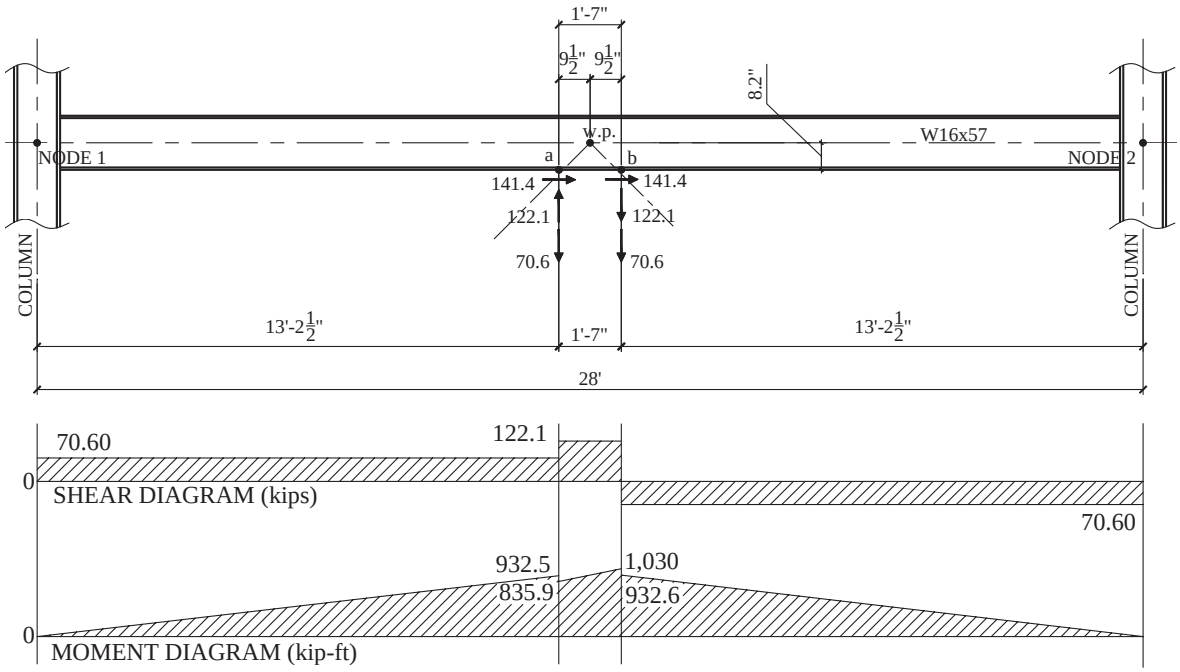

Fig. 17. $\Sigma V_i \neq 0$ *(141.2 kips) beam shear and moment with mid-span work point.*

reactions. Given that the beam shear and moment distributions are a function of the beam end reactions, the span of the beam also affects the beam shear and moment distribution as well as the maximum beam shears and moments.

5. THE CHEVRON EFFECT

When evaluating the brace forces in a chevron braced frame subjected to lateral loads, the analysis will reveal that one brace is in tension while the other is in compression. For static equilibrium, the vertical components of the brace forces will sum algebraically to zero. However, it is sometimes necessary, or required, to perform some type of mechanism analysis where in such a case, the algebraic sum of the vertical components of the brace forces will be non-zero. One example of a mechanism analysis is that required in a seismic braced frame where the brace in tension is assumed to reach the expected tensile strength of the brace, while the brace in compression is assumed to reach its buckling strength, or even a post-buckling strength. The impact of the brace forces on the frame beam needs to be evaluated in either case.

The following example problem illustrates the chevron effect, and emphasizes the importance of accounting for the span of the beam as well as the location of the work point along the span of the beam.

Example 2: The Chevron Effect with Mechanism Analysis

For the chevron bracing configuration shown in Figure 19:

1. Determine the force distribution in the connection for the brace forces given in Table 1. For this analysis only the forces acting on section *a-a* need to be determined using Equations 1 through 4. For an actual gusset design, the forces acting on section *b-b* are also required, but not necessary, for this example problem.
2. Determine the beam shear and moment distribution along the span of the beam for each load case based on the forces and moments acting on section *a-a* determined in Section 1 of this paper.
3. Compare the maximum beam shears and moments determined as if the connection was isolated from the frame to those values obtained from the beam shear and moment diagrams.

Assume that $(KL)_x$ and $(KL)_y$ for both braces is 22 ft. Note that this length accounts for the pull-off dimensions at both ends of each brace.

Typically, both directions of lateral load would be considered. For this example, only the three load cases shown in Table 1 will be considered.

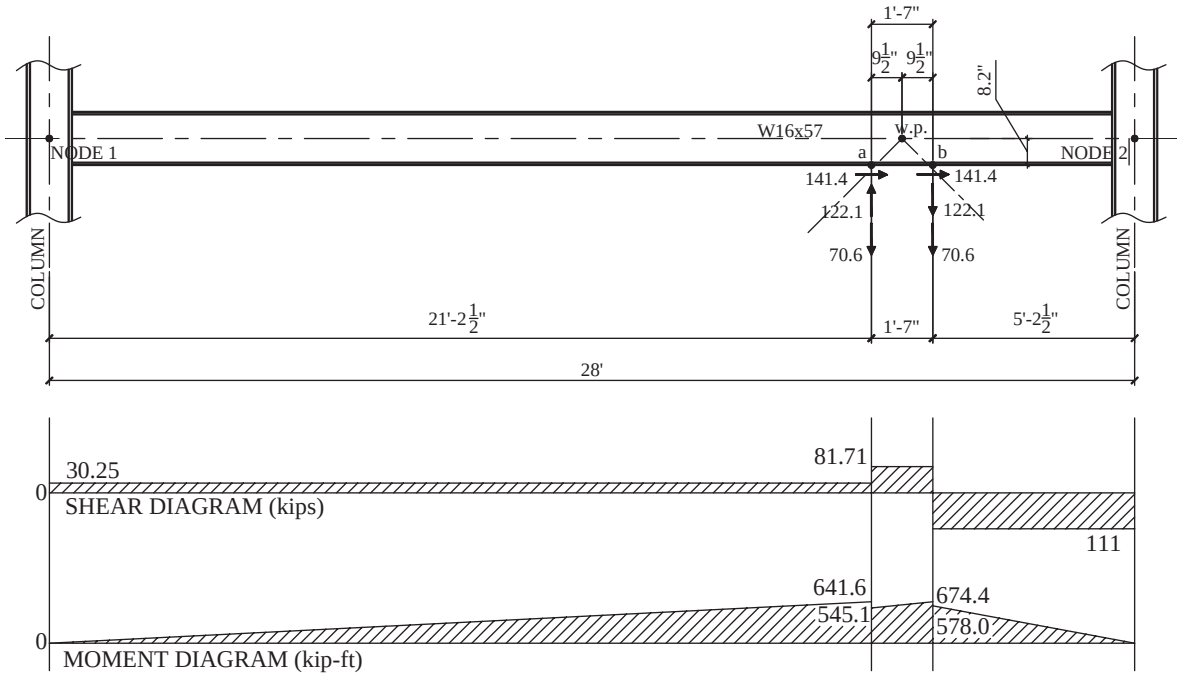

Fig. 18. $\Sigma V_i \neq 0$ *(141.2 kips) beam shear and moment with work point off mid-span.*

Table 1. Load Cases for Example 2		
Load Case	**P1 (kips)**	**P2 (kips)**
1	+449	–540
2	$+R_yF_yA_g = +1{,}205$	$Pb = -1.14F_{cre}A_g = -778$
3	$+R_yF_yA_g = +1{,}205$	$(0.3)P_b = -233$

Sign convention: (+) indicates tension; (–) indicates compression.

It is worth noting here that load cases 2 and 3 are representative of the mechanistic analysis required by the AISC *Seismic Provisions.*

Example 2: Solution

The variables for Example 2 are shown below.

$L_g = 47.75$ in., $L_1 = 20.50$ in., $L_2 = 27.25$ in.

$e_b = 10.70$ in., $h = 9.125$ in.

$$\Delta = \frac{1}{2}(20.50 \text{ in.} - 27.25 \text{ in.}) = -3.375 \text{ in.}$$

Load Case 1

$H_1 = -269.40$ kips

$H_2 = -403.25$ kips

$V_1 = -359.18$ kips

$V_2 = 359.18$ kips

Figure 20 shows the geometry and brace forces for Load Case 1. From the data given in Figure 20, the forces acting on section *a-a* can be determined.

Forces acting on section* a-a*:

$$H_{a-a} = -(H_1 + H_2)$$
$$= -(-269.40 - 403.25)$$
$$= 672.65 \text{ kips}$$
$$V_{a-a} = -(V_1 + V_2)$$
$$= -(-359.18 + 359.18)$$
$$= 0 \text{ kips}$$
$$M_{a-a} = (V_1 + V_2)\Delta - (H_1 + H_2)e_b$$
$$= (-359.18 + 359.18)(-3.375)$$
$$-(-269.40 - 403.25)(10.70)$$
$$= 7{,}195.57 \text{ kip-in.}$$

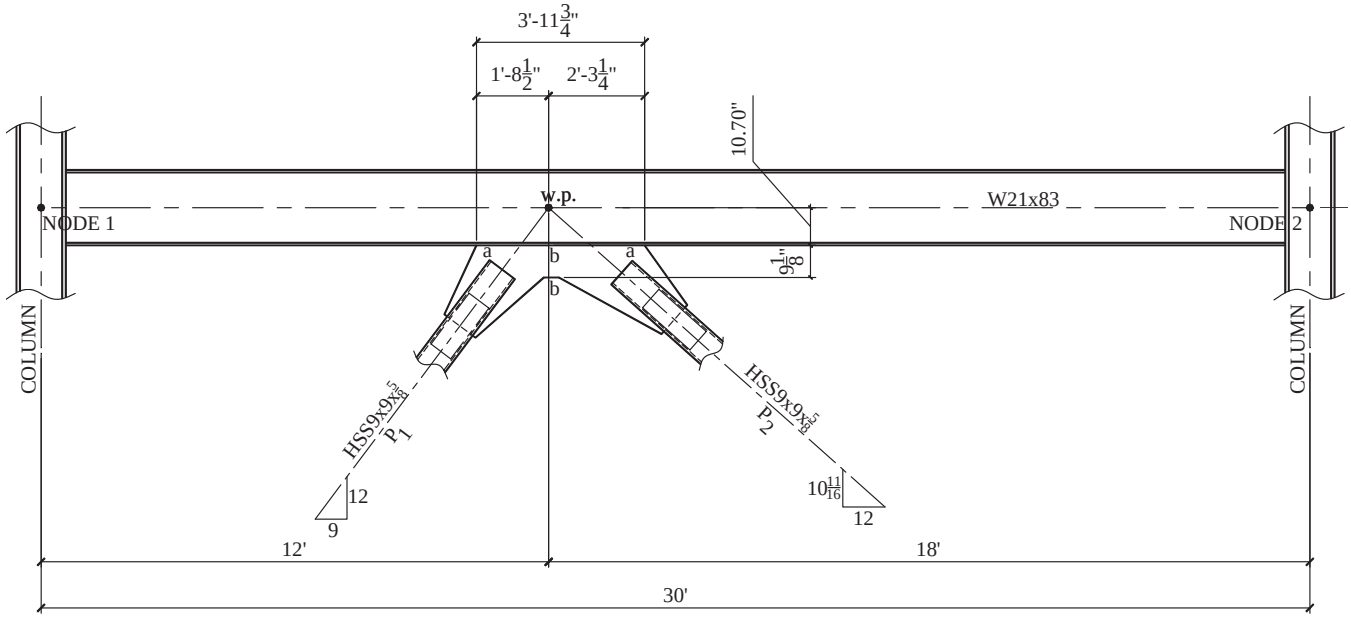

Fig. 19. Connection geometry and dimensions for Example 2.

The couple of $M_{a\text{-}a}$ is:

$$N_{eq} = \frac{(2)(7{,}195.57)}{47.75} = 301.4 \text{ kips}$$

Figure 21 shows the resulting interface forces and beam shear and moment distributions. As can be seen in Figure 21, the maximum beam shear and moment are:

$$V_{u,\max} = 301.4 \text{ kips}$$
$$M_{u,\max} = 299.8 \text{ kip-ft}$$

Load Case 2

Figure 22 shows the geometry and brace forces for load case 2. From the data given in Figure 22, the forces acting on section *a-a* can be determined.

$$H_1 = -723.00 \text{ kips}$$
$$H_2 = -580.89 \text{ kips}$$
$$V_1 = -964.00 \text{ kips}$$
$$V_2 = 517.44 \text{ kips}$$

Forces acting on section* a-a*:

$$H_{a-a} = -(H_1 + H_2) = -(-723.00 - 580.89)$$
$$= 1{,}303.98 \text{ kips}$$

$$V_{a-a} = -(V_1 + V_2) = -(-964.00 + 517.44)$$
$$= 446.56 \text{ kips}$$
$$M_{a-a} = (V_1 + V_2)\Delta - (H_1 + H_2)e_b$$
$$= (-964.00 + 517.44)(-3.375)$$
$$-(-723.00 - 580.98)(10.70)$$
$$= 15{,}459.77 \text{ kip-in.}$$

The couple of $M_{a\text{-}a}$ is:

$$N_{eq} = \frac{(2)(15{,}459.77)}{47.75} = 647.53 \text{ kips}$$

Figure 23 shows the resulting interface forces and beam shear and moment distributions. As can be seen in Figure 23, the maximum beam shear and moment are:

$$V_{u,\max} = 602.9 \text{ kips}$$
$$M_{u,\max} = 3{,}605 \text{ kip-ft}$$

Load Case 3

Figure 24 shows the geometry and brace forces for load case 3. From the data given in Figure 24, the forces acting on section *a-a* can be determined.

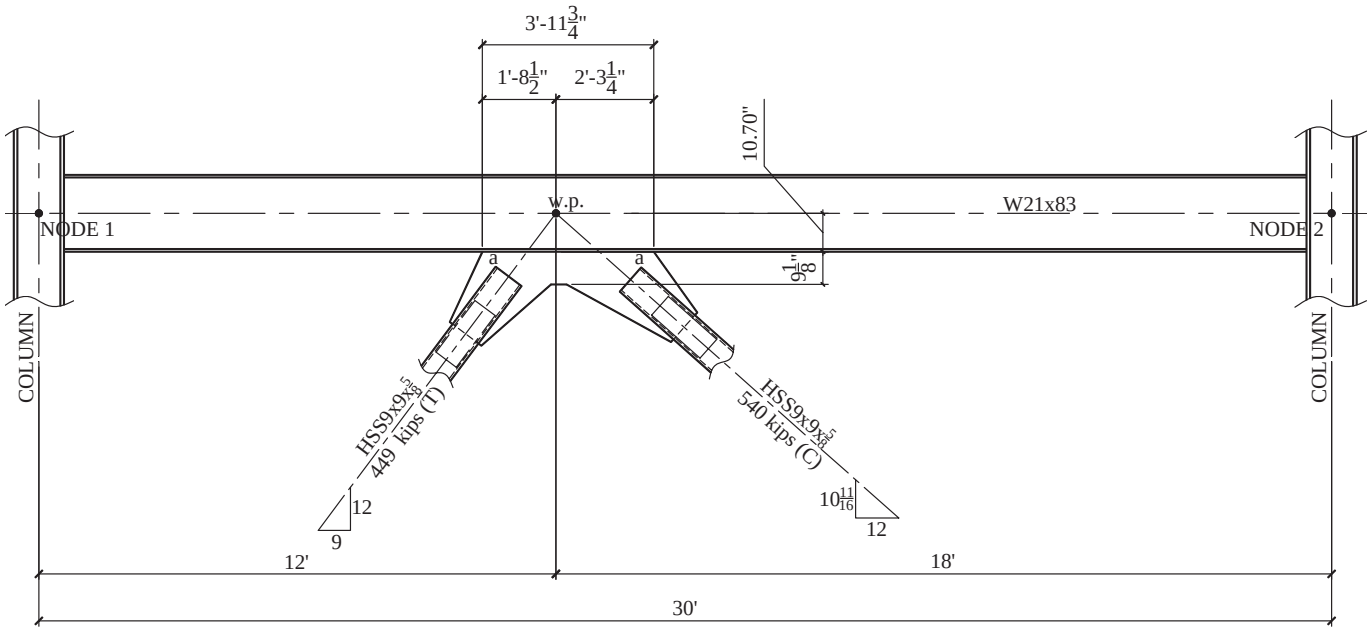

Fig. 20. Geometry and brace forces for Example 2, load case 1.

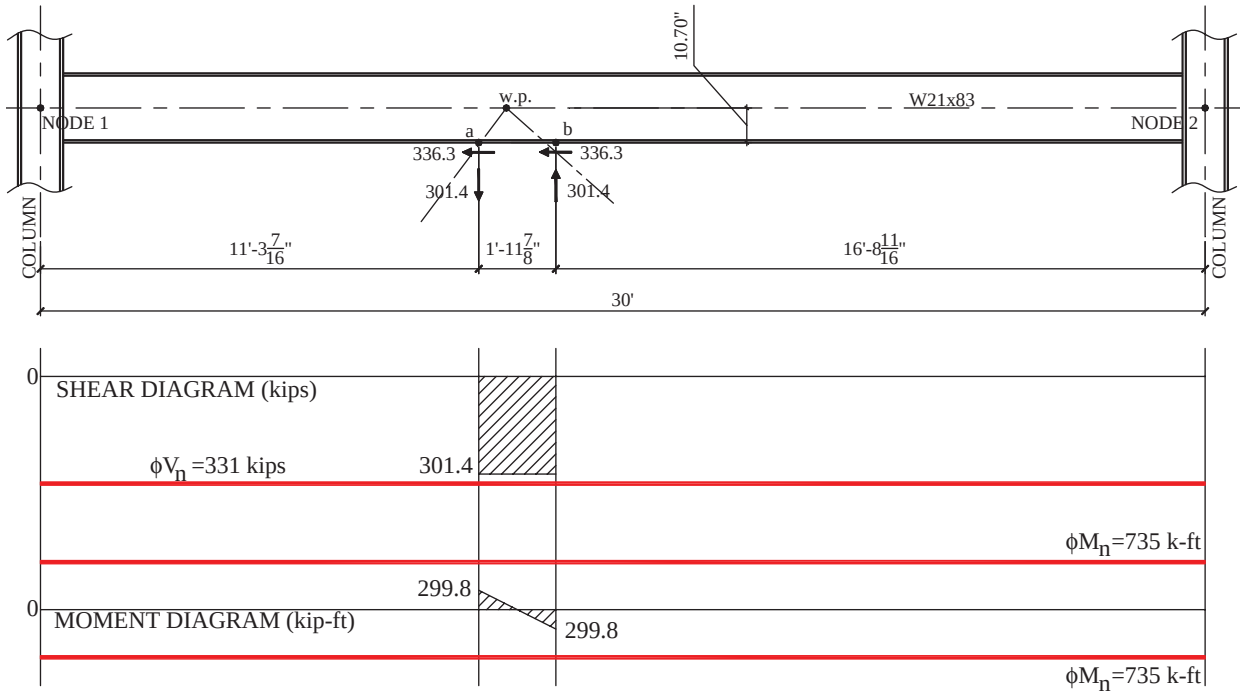

Fig. 21. Beam shear and moment distribution for load case 1.

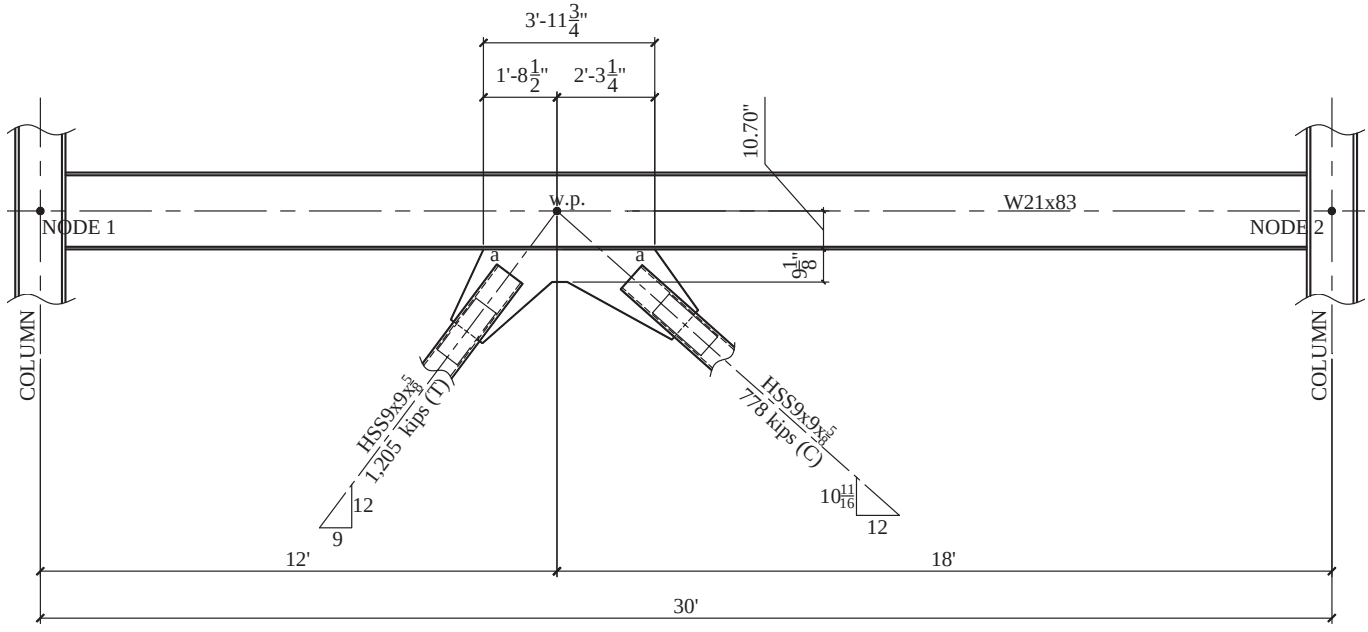

Fig. 22. Geometry and brace forces for Example 2, load case 2.

$H_1 = -723.00$ kips

$H_2 = -174.00$ kips

$V_1 = -964.00$ kips

$V_2 = 154.97$ kips

Forces acting on section* a-a*:

$$H_{a-a} = -(H_1 + H_2) = -(-723.00 - 174.00)$$
$$= 897.00 \text{ kips}$$
$$V_{a-a} = -(V_1 + V_2) = -(-964.00 + 154.97)$$
$$= 809.03 \text{ kips}$$
$$M_{a-a} = (V_1 + V_2)\Delta - (H_1 + H_2)e_b$$
$$= (-964.00 + 154.97)(-3.375)$$
$$-(-723.00 - 174.00)(10.70)$$
$$= 12{,}328.35 \text{ kip-in.}$$

The couple of $M_{a\text{-}a}$ is:

$$N_{eq} = \frac{(2)(12{,}328.35)}{47.75} = 516.37 \text{ kips}$$

Figure 25 shows the resulting interface forces and beam shear and moment distributions. As can be seen in Figure 25, the maximum beam shear and moment are:

$V_u = 485.6$ kips

$M_u = 5{,}881$ kip-ft

A summary of Example 2 results are shown in Table 2. Upon reviewing these results, three primary observations can be made.

1. The maximum beam shear occurs within the connection region in load cases 1 and 2 and outside of the

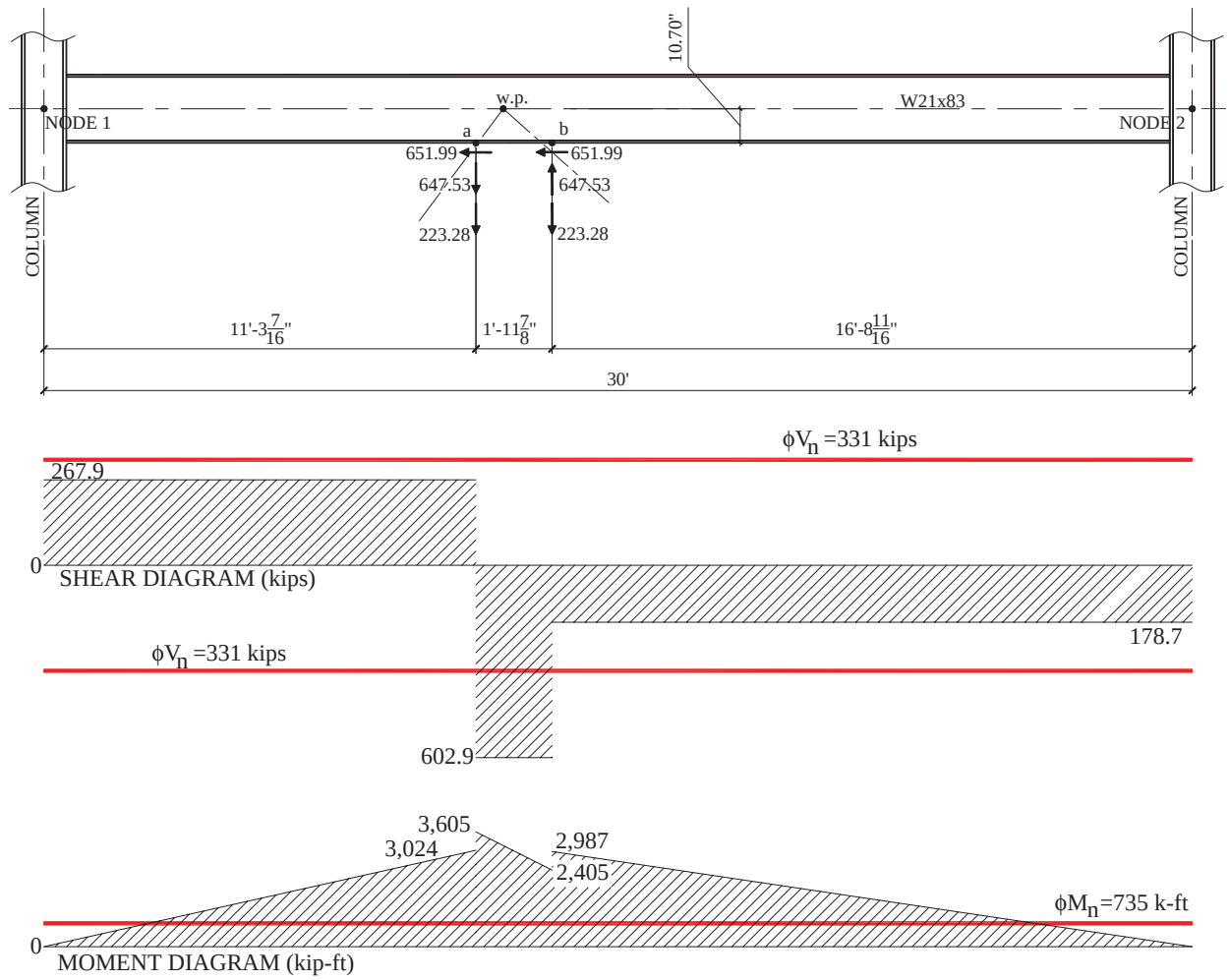

Fig. 23. Beam shear and moment distribution for load case 2.

Table 2. Beam Shears and Moments: Summary of Example 2 Results											
			Connection Isolated from Frame				Considering Frame Beam Span and Work Point Location				V_u,max [Within (W) or outside (O) connection region]
Load Case	ϕV_n (kips)	ϕM_n (k-ft)	$V_{u,\max}$ (kips)	$M_{u,\max}$ (k-ft)	$\frac{V_{u,\max}}{\phi V_n}$	$\frac{M_{u,\max}}{\phi M_n}$	$V_{u,\max}$ (kips)	$M_{u,\max}$ (k-ft)	$\frac{V_{u,\max}}{\phi V_n}$	$\frac{M_{u,\max}}{\phi M_n}$	
1	331	735	301.4	299.8	0.911	0.408	301.4	299.8	0.911	0.408	W
2	331	735	647.5	644.1	1.96	0.876	602.9	3,605	1.82	4.90	W
3	331	735	516.4	513.7	1.56	0.699	485.6	5,881	1.47	8.00	O

connection region in load case 3. Thus, if the span of the beam and the location of the work point are not considered when evaluating the beam shear, the maximum beam shear would not be captured for load case 3.

2. The algebraic sum of the vertical components of the brace forces is zero for load case 1. For load cases 2 and 3, the algebraic sums of the vertical components of the brace forces are −446.6 kips and −809.0 kips, respectively. Thus, the vertical components of the brace forces for load cases 2 and 3 are unbalanced. For load case 2, if the maximum beam shear is determined assuming the connection is isolated from the frame, the maximum beam shear is determined to be 647.5 kips. When the span of the beam and the location of the work point are considered for load case 2, the maximum beam shear is determined to be 602.9 kips, an overestimation of approximately 7.3%. For load case 3, if the maximum beam shear is determined assuming the connection is isolated from the frame, the maximum beam shear is determined to be 516.4 kips. When the span of the beam and the location of the work point are considered for load case 3, the maximum beam shear is determined to be 485.6 kips (and is located outside of the connection region), an overestimation of approximately 6.3%. For this example, the maximum beam shear is overestimated by 6.3% to 7.3%. Under different geometry and loading, it's quite possible to significantly underestimate or overestimate the maximum beam shear when the connection is evaluated as if it is isolated from the frame.

3. The beam moment is significantly underestimated when the connection is evaluated as if it is isolated from the beam when the vertical components of the

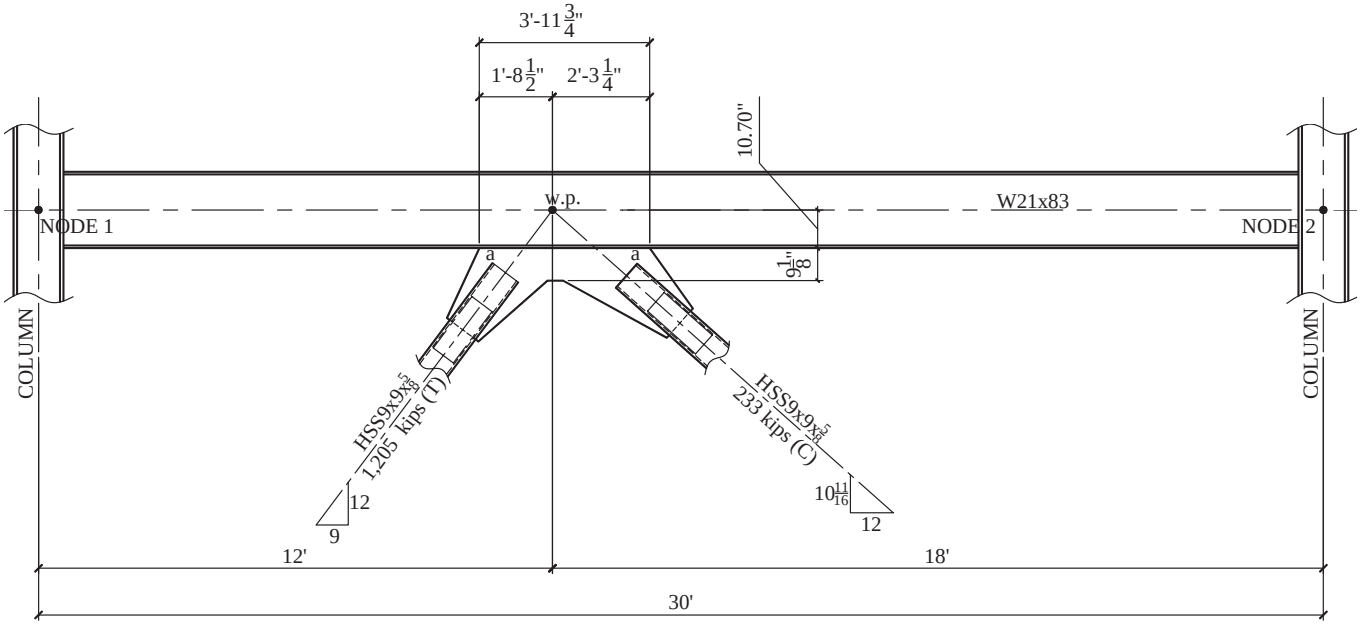

Fig. 24. Geometry and brace forces for Example 2, load case 3.

brace forces are unbalanced. Referring to Table 2, the ratios of available flexural strength to required flexural strength for load cases 2 and 3 are 0.20 and 0.12, respectively. Thus, the actual beam moment demands for load cases 2 and 3 are 4.90 and 8.00 times larger, respectively, than what would be determined if the span of the beam and location of the work point is not considered.

It is important to reiterate that the beam shears and moments calculated for this example are based on the brace forces only. Load effects from other types of loads (e.g., dead, live, etc.) must be superimposed to get the total shear and moment demands on the beam. In almost all cases, the additional loads will increase the maximum beam shear and moments beyond those imparted to the beam by the brace forces alone.

6. FINAL BEAM SIZE SELECTION

As demonstrated in the previous discussions, it is important to include brace force effects when making final beam size selections. To account for the brace force effects, the geometry of the connection must be known in order to calculate the gusset-to-beam interface forces. Typically, the connection geometry is not known at the time final beam size selection is made and, therefore, can be problematic. This is especially problematic when connection design is delegated to a contractor that is not the engineer-of-record for the design of the structure. To address this issue, the authors recommend a rule of thumb for accounting for the brace force effects.

To approximate the brace force effects on the beam, assume that the length of the gusset is approximately one-sixth of the beam span, and assume that the depth of the beam, d_b, in inches, is 75% of the span of the beam in feet.

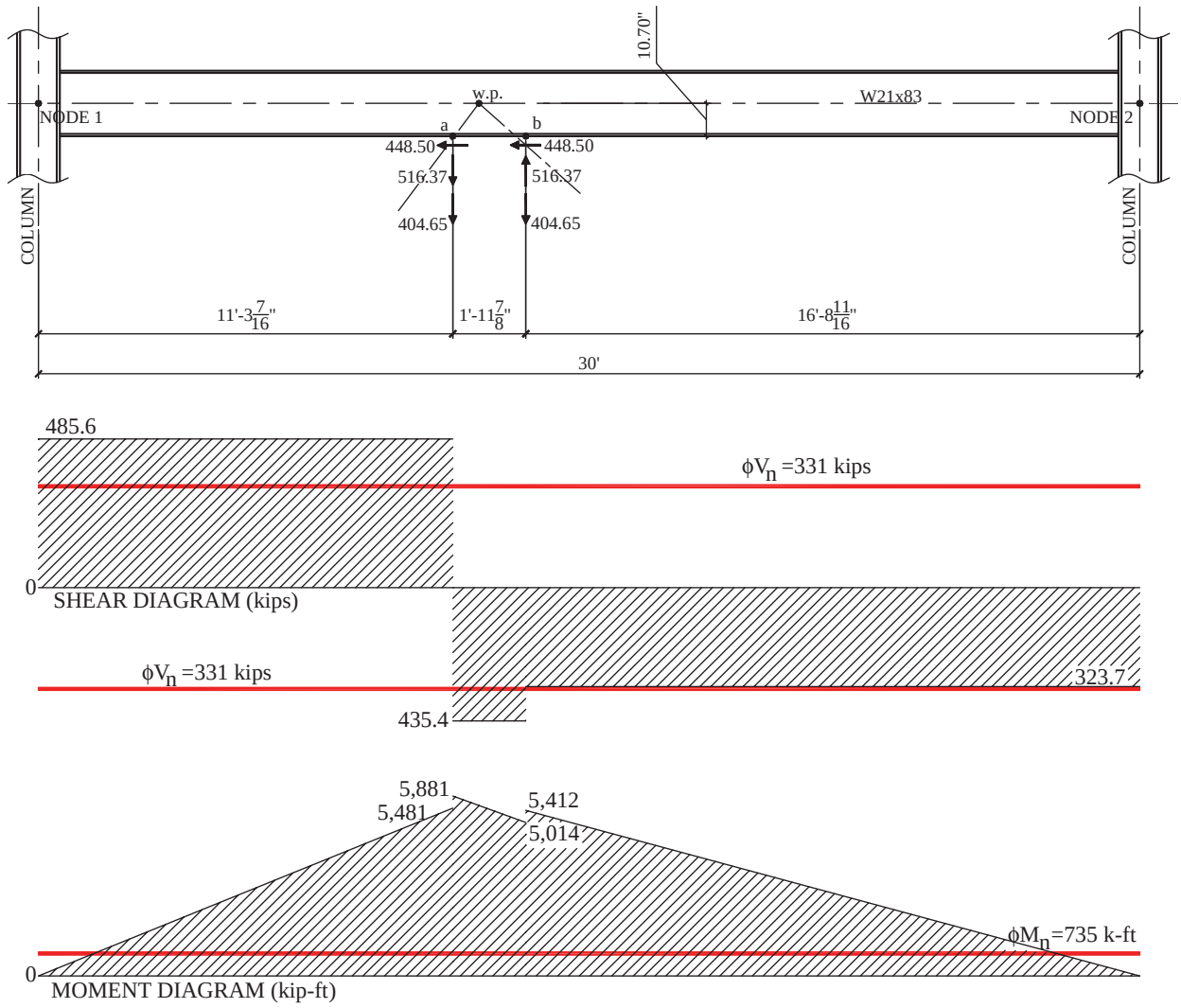

Fig. 25. Beam shear and moment distribution for load case 3.

Thus, the approximate value for e_b can be taken as one-half of the approximated beam depth. These approximations for a trial beam size are given in Equations 15 and 16. These approximations are ratios averaged from 20 different chevron brace connections taken from real connections designed by the authors over several years. The 20 different chevron connections were taken from a mix of different types of projects with varying types of braces, bevels, and brace forces.

$$L_{g,app} = \frac{L}{6} \tag{15}$$

$$e_{b,app}(\text{in.}) = 0.375(\text{span of the beam, ft}) \tag{16}$$

With the length of the gusset and e_b approximated, the moment acting at the gusset-to-beam interface can be conservatively estimated using Equation 17. Equation 17 contains the term with the horizontal components of the brace forces given in Equation 4. The couple of the moment acting on the gusset-to-beam interface can be estimated by dividing Equation 17 by the approximated gusset length. Equation 18 is the simplified expression for the approximated couple. The couples are placed at the centroids of the two half gusset bodies (i.e, at $L_{g,app}/4$ in from each gusset edge; $L_g/2$ apart). The direction of the couple should be considered to act in each direction to capture the "worst case" effect when combining the brace force effects with other types of loads (e.g., dead, live, wind load, etc.).

$$M_{a-a,app} = (H_1 + H_2)e_{b,app} \tag{17}$$

$$\begin{aligned} N_{eq,app} &= \pm\frac{2M_{a-a,app}}{L_{g,app}} \\ &= \pm\frac{(2)(6)(H_1 + H_2)e_{b,app}}{L} \\ &= \pm\frac{12(H_1 + H_2)(0.375L)}{(12\text{ in./ft})L} \\ N_{eq,app} &= \pm 0.375(H_1 + H_2) \end{aligned} \tag{18}$$

Referring to Equation 4, the moment at the gusset-to-beam interface, $M_{a\text{-}a}$, has two terms; the first term is a function of Δ and the second term is a function of e_b. The proposed method presented here for approximating the moment at the gusset-to-beam interface does not consider any potential vertical misalignment of the work point with the centroid of the gusset interface. That is, the first term of Equation 4, $(V_1+V_2)\Delta$, is not accounted for in the approximation. Upon close examination of Equation 4, it can be seen that the two terms may be the sum of the two terms or the difference of the two terms. Each term has the possibility of being positive or negative. When the signs of each parameter are such that the moment is the difference between the two terms, the approximated moment will be overestimated. When the signs of each parameter are such that the two terms are additive, the approximated moment will be underestimated. This is not a significant concern. Generally, the Δ term is a relatively small percentage of the total moment acting at the gusset interface. Additionally, the approximated gusset length given in Equation 15 will generally underestimate the actual gusset length resulting in a relatively larger couple. Thus, the rule of thumb presented here will provide a reasonably conservative estimate to be used for beam size selection.

7. DESIGN EXAMPLE

Example 3: Accounting for Brace Forces When Sizing Beam

Gravity Loads
D = 118 psf (includes all self-weight and all other superimposed dead loads)
L = 50 psf (non-reducible)
The tributary width of the frame beam is 28 ft.

Lateral Loads
The load effects on the braces from a wind load analysis are given in Figure 26. The brace forces given are LRFD loads and are used with load case 6 shown below.

Load Combinations
Evaluate only load combinations 2 and 4 from ASCE 7-10 (ASCE, 2010), as given below.
Load case 2: $1.2D + 1.6L$
Load case 4: $1.2D + 0.5L + 1.0W$ (note that L is less than 100 psf)

Deflection Limits for Frame Beam (gravity)
D+L: L/240
L: L/360
When checking deflection, assume that the clear span of the beam is from column centerline to column centerline.

Problem Statement
A partial elevation of the braced frame is shown in Figure 26. As can be seen in the figure, the geometry and brace forces are given. The brace forces shown are load effects from a wind analysis.

1. Calculate the design gravity load on the beam for load cases 2 and 4 given previously.
2. Make a beam selection neglecting the load effects of the brace forces acting at the gusset-to-beam interfaces:
   a. Provide a beam size that satisfies the strength, deflection and drift requirements given above. Do not include the effect of the brace force distributions

acting at the gusset interfaces, and assume the beam spans from column to column (i.e., the braces are not present to carry gravity load effects)

b. Calculate the brace force distributions at section *a-a* for the braces above and below the frame beam.

c. Draw the beam shear and moment diagrams that include both the LRFD gravity loads and forces acting on the beam imparted by the brace force distributions.

d. Compare the required beam shears and moments to the available beam shears and moments obtained in parts b and c.

3. Make a beam selection including the load effects of the brace forces acting at the gusset-to-beam interfaces:

   a. Determine a trial beam size that satisfies the strength, deflection and drift requirements given above. Include the effect of the brace force distributions using the rule of thumb recommended previously.

   b. Using the trial beam size selected in part 3a, calculate the brace force distributions at section *a-a* for the braces above and below the frame beam.

   c. Draw the beam shear and moment diagrams that include both the LRFD gravity loads and forces acting on the beam imparted by the brace force distributions.

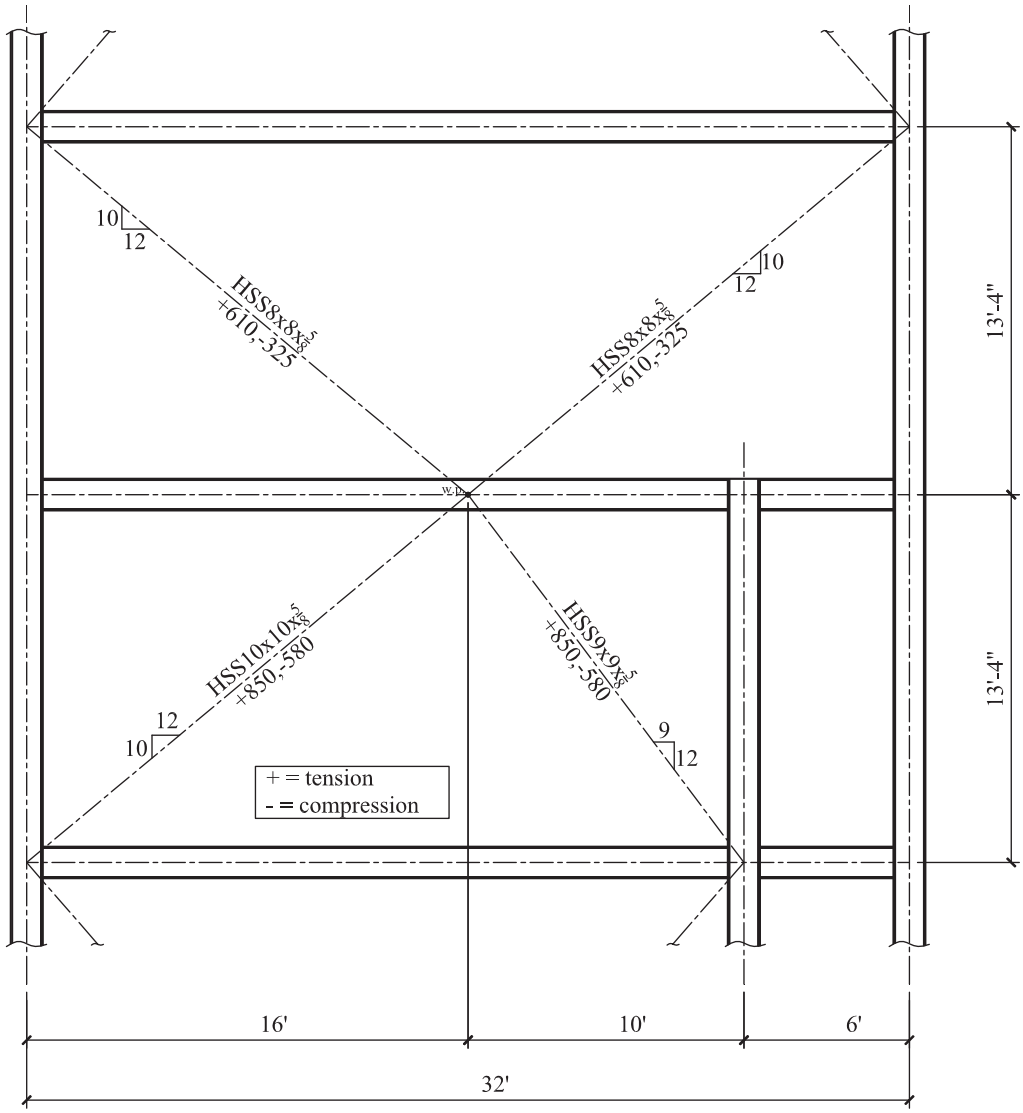

Fig. 26. Partial frame elevation for Example 3. Tributary width of frame beam is 28 ft.

d. Compare the required beam shear and moment to the available beam shear and moment

4. Assume that a connection designer is faced with a design scenario such as that shown later in Figure 30 where the required beam shear and moment exceed the available beam shear and moment. Calculate the required web doubler thickness and length of the web doubler for the beam and loading shown in Figure 30 (i.e., the beam used in part 2 of this problem). Evaluate the web doubler for each of the following two load distribution conditions:

   a. Using the resultant forces method.

   b. Using the distributed forces method.

Note that the available beam moment is also exceeded in this scenario which should be addressed in some manner. However, this issue is not covered here.

Use the brace force load case shown in Figure 27. In the following solution, the authors have established gusset plate geometry based on the trial e_b values established for each part of the problem.

Example 3: Solution

Part 1. *Calculate design beam gravity load.*

It is given in the problem statement that the tributary width of the frame is 28 ft. The design gravity loads for load cases 2 and 4 are:

Load case 2

$$w_D = \frac{(118 \text{ psf})(28 \text{ ft})}{1{,}000 \text{ lb/kip}} = 3.3 \text{ k/ft}$$

$$w_L = \frac{(50 \text{ psf})(28 \text{ ft})}{1{,}000 \text{ lb/kip}} = 1.4 \text{ k/ft}$$

$$w_{u,2} = 1.2D + 1.6L = (1.2)(3.3) + (1.6)(1.4)$$
$$= 6.20 \text{ k/ft}$$

Load case 4

$$w_D = \frac{(118 \text{ psf})(28 \text{ ft})}{1{,}000 \text{ lb/kip}} = 3.3 \text{ k/ft}$$

$$w_L = \frac{(50 \text{ psf})(28 \text{ ft})}{1{,}000 \text{ lb/kip}} = 1.4 \text{ k/ft}$$

$$= 1.2D + 0.5L = (1.2)(3.3) + (0.5)(1.4)$$

$$w_{u,4} = 4.66 \text{ k/ft}$$

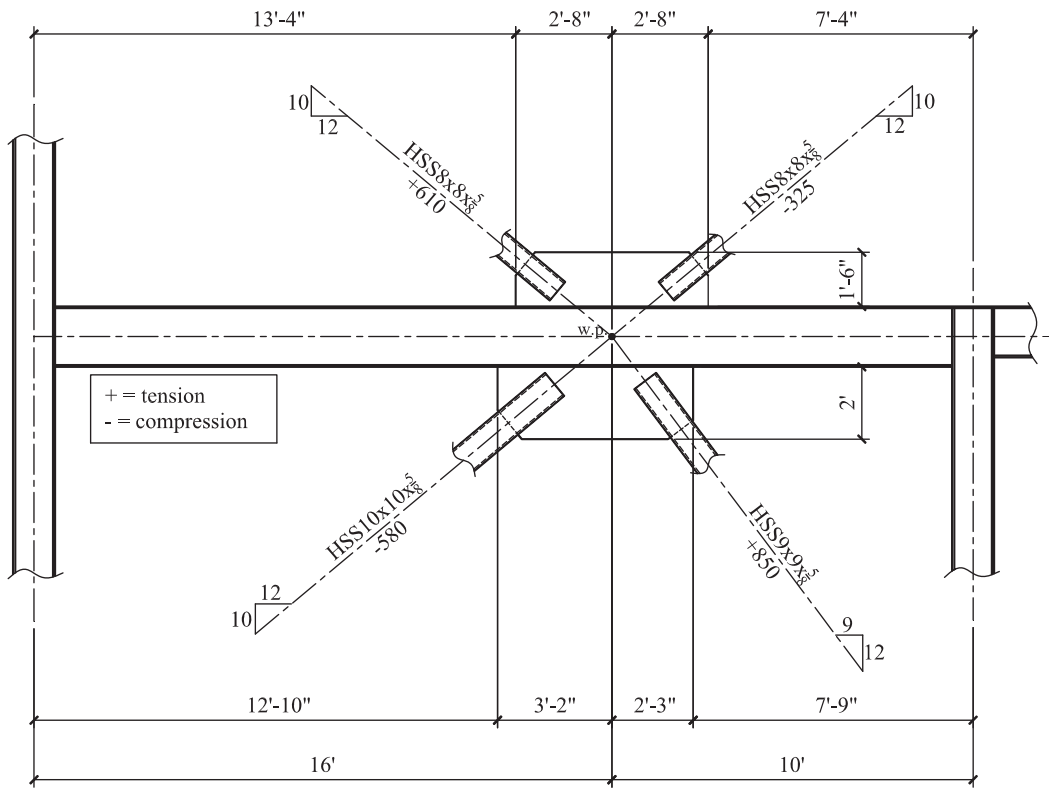

Fig. 27. Connection geometry and brace forces for Example 3.

Part 2a. *Size beam for load determined in part 1; include deflection check. Do not include brace forces.*

The required beam shears and moments are:

$$V_{u,2} = \frac{w_{u,2}L}{2} = \frac{(6.20 \text{ k/ft})(26 \text{ ft})}{2}$$
$$= 80.6 \text{ kips}$$
$$M_{u,2} = \frac{w_{u,2}L^2}{8} = \frac{(6.20 \text{ k/ft})(26 \text{ ft})^2}{8}$$
$$= 524 \text{ k-ft}$$
$$V_{u,4} = \frac{w_{u,2}L}{2} = \frac{(4.66 \text{ k/ft})(26 \text{ ft})}{2}$$
$$= 60.6 \text{ kips}$$
$$M_{u,4} = \frac{w_{u,2}L^2}{8} = \frac{(4.66 \text{ k/ft})(26 \text{ ft})^2}{8}$$
$$= 394 \text{ k-ft}$$

Load case 2 governs the design for strength. The plastic section modulus, Z, required to resist $M_{u,2}$ is:

$$Z_{req} \geq \frac{(524 \text{ k-ft})(12 \text{ in./ft})}{(0.9)(50 \text{ ksi})} = 140 \text{ in.}^3$$

The moment of inertia required for the deflection limits is:

$$\delta_i = \frac{5w_iL^4}{384EI_i} \rightarrow I_i \geq \frac{5w_iL^4}{384E\delta_i}$$
$$I_{D+L} \geq \frac{(5)\left(\frac{3.3+1.4}{12}\right)[(26)(12)]^4}{(384)(29,000)\left(\frac{(26)(12)}{240}\right)} = 1,282 \text{ in.}^4$$
$$I_L \geq \frac{(5)\left(\frac{1.4}{12}\right)[(26)(12)]^4}{(384)(29,000)\left(\frac{(26)(12)}{360}\right)} = 573 \text{ in.}^4$$

Therefore, $I > 1{,}282$ in.^{4}

Thus, for a trial beam size, select a beam that satisfies the following requirements.

$V_u = 80.6$ kips
$M_u = 524$ k-ft
$Z_{req} \geq 140$ in.^{3}
$I \geq 1{,}282$ in.^{4}

Try a W21×83 beam.

$\phi M_n = 735$ k-ft $> M_u = 524$ k-ft **o.k.**
$\phi V_n = 331$ k $> V_u = 80.6$ k **o.k.**
$I = 1{,}830$ in.$^4 > I = 1{,}282$ in.^{4} **o.k.**

Part 2b. *Calculate brace force distributions on sections* a-a *at top and bottom of beam.*

With the size of the beam known, the force distributions at the gusset interfaces can be calculated using the procedure presented previously in this paper. Figure 28 shows the beam shear and moment diagrams for gravity load. Note that load case 4 is the load combination with wind. Thus, the diagrams shown in Figure 28 are based on load case 4 (i.e., 1.2D + 0.5L).

Part 2c. *Draw beam shear and moment diagrams for braces force determined on part 2b.*

Figure 27 shows the geometry and brace forces. From the data given in the figure, the forces acting on sections *a-a* at the top and bottom of the beam can be determined.

Note that the forces acting at the top gusset-to-beam interface are calculated using the analysis procedure and sign convention presented in Section 1, Figure 3, of this paper, assuming that the free body diagrams shown in Figure 3 are rotated 180 degrees about an axis perpendicular to the work point.

Section* a-a*—top of beam:

$H_1 = 249.67$ kips
$H_2 = 468.61$ kips
$V_1 = 208.06$ kips
$V_2 = -390.51$ kips

Forces acting on section* a-a*:

$$H_{a-a} = -(H_1 + H_2)$$
$$= -(249.67 + 468.61)$$
$$= -718.29 \text{ kips}$$
$$V_{a-a} = -(V_1 + V_2) = -(208.06 - 390.51)$$
$$= 182.45 \text{ kips}$$

$$\Delta = \frac{1}{2}(L_1 - L_2) = 0.5(32.0 - 32.0)$$
$$= 0$$
$e_b = 10.70$ in.
$$M_{a-a} = (V_1 + V_2)\Delta - (H_1 + H_2)e_b$$
$$= (208.06 - 390.51)(0)$$
$$-(249.67 + 468.61)(10.70)$$
$$= -7{,}685.67 \text{ kip-in.}$$

The couple of M_{a-a} is:

$$N_{eq} = \pm\frac{(2)(7{,}182.67)}{64.0} = 240.18 \text{ kips}$$

Section* a-a *– bottom of beam:

$H_1 = 445.57$ kips
$H_2 = 510.00$ kips
$V_1 = 371.31$ kips
$V_2 = -680.00$ kips

Forces acting on section* a-a*:

$$H_{a-a} = -(H_1 + H_2) = -(445.57 + 510.00) = -955.57 \text{ kips}$$

$$V_{a-a} = -(V_1 + V_2) = -(371.31 - 680.00) = 308.69 \text{ kips}$$

$$\Delta = \frac{1}{2}(L_1 - L_2) = 0.5(38.0 - 27.0) = 5.50 \text{ in.}$$

$e_b = 10.70$ in.

$$M_{a-a} = (V_1 + V_2)\Delta - (H_1 + H_2)e_b = (371.31 - 680.00)(5.50) - (445.57 + 510.00)(10.70) = -11{,}922.39 \text{ kip-in.}$$

The couple of $M_{a\text{-}a}$ is:

$$N_{eq} = \pm\frac{(2)(11{,}922.39)}{65.0} = 366.84 \text{ kips}$$

Figure 29 shows the force distribution acting at the gusset-to-beam interfaces as determined in the preceding calculations, along with the beam shear and moment diagrams generated by the brace forces acting on the beam. Figure 30 shows the beam shear and moment diagrams for all of the load effects given in load case 4 (the combination of the load effects shown in Figures 28 and 29).

Part 2d. *Compare beam shear and moment diagrams generated for parts 2b and 2c.*

Referring to Figure 28, if the beam is evaluated for gravity load effects only, the beam has sufficient shear and moment strength. This should be no surprise considering that the beam size was selected based on required gravity load and deflection considerations. However, the brace forces do have an impact on the forces imparted to the beam.

Figure 29 shows the beam shear and moment diagrams for the brace force effects only. Note in the force distributions acting at the gusset-to-beam interfaces that the couples, N_{eq}, of the moments, $M_{a\text{-}a}$, acting at the top and bottom of the beam act in the same direction. However, the normal forces acting at the top and bottom of the beam due to the unbalanced vertical components of the brace forces, $\frac{1}{2}V_{a\text{-}a}$, act in the opposite direction. This is always true for the typical case where one line of braces is in tension while the other line of braces is in compression. Thus, the moments acting at the interfaces of a two-story X-braced frame accumulate,

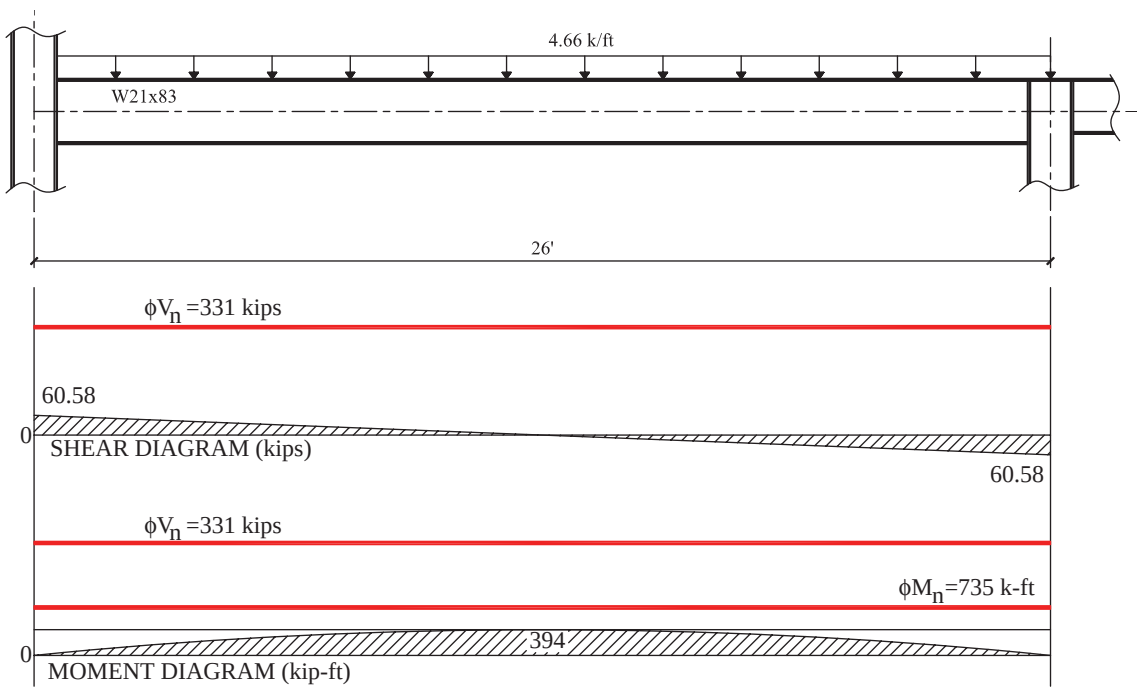

Fig. 28. Beam shear and moment for gravity: load case 4 for part 2 of Example 3.

while the unbalanced vertical component force at the top and bottom subtract in regard to the impact on the beam.

Referring to the shear and moment diagrams in Figure 29, considering the brace forces only, the required beam shear and moment strength is 592 kips and 1,389 k-ft, respectively. The available beam shear and moment strength is 331 kips and 735 k-ft, respectively. The beam is undersized for the brace forces alone with required strength to available strength ratios for shear and moment equal to 592/331 = 1.79 and 1,389/735 = 1.89, respectively. These ratios will be more severe when considering the gravity load effects in combination with the brace forces.

It is also worth noting that if the beam is evaluated for shear and moment as if the joint is isolated from the frame, the maximum beam shear and moment due to the brace force distribution would be determined to be 607 kips and 712 kip-ft, respectively (see Figure 31). This analysis gives a conservative value for the required shear and significantly underestimates the moment demand on the beam. This is another example of why the impact of chevron bracing on the frame beam should not be evaluated as if the joint is isolated from the frame when an unbalanced vertical force is present. The isolated approach is further complicated when the Δ parameter is non-zero as with this example problem. Referring to Figure 31, note the Σ*V*Δ moment shown in the loading diagram; this couple needs to be included in order to close the moment diagram. However, the Σ*V*Δ moment must be neglected in order to satisfy static equilibrium within the isolated free body diagram; this is a further complication associated with incorrectly evaluating the beam as if the joint is isolated from the frame.

Referring to Figure 30, it can be seen that when all load effects from load case 4 are considered, and the span of the beam and location of the work point are considered, the required beam shear and moment is 585 kips and 1,748 kip-ft, respectively. The W21×83 beam has available shear and

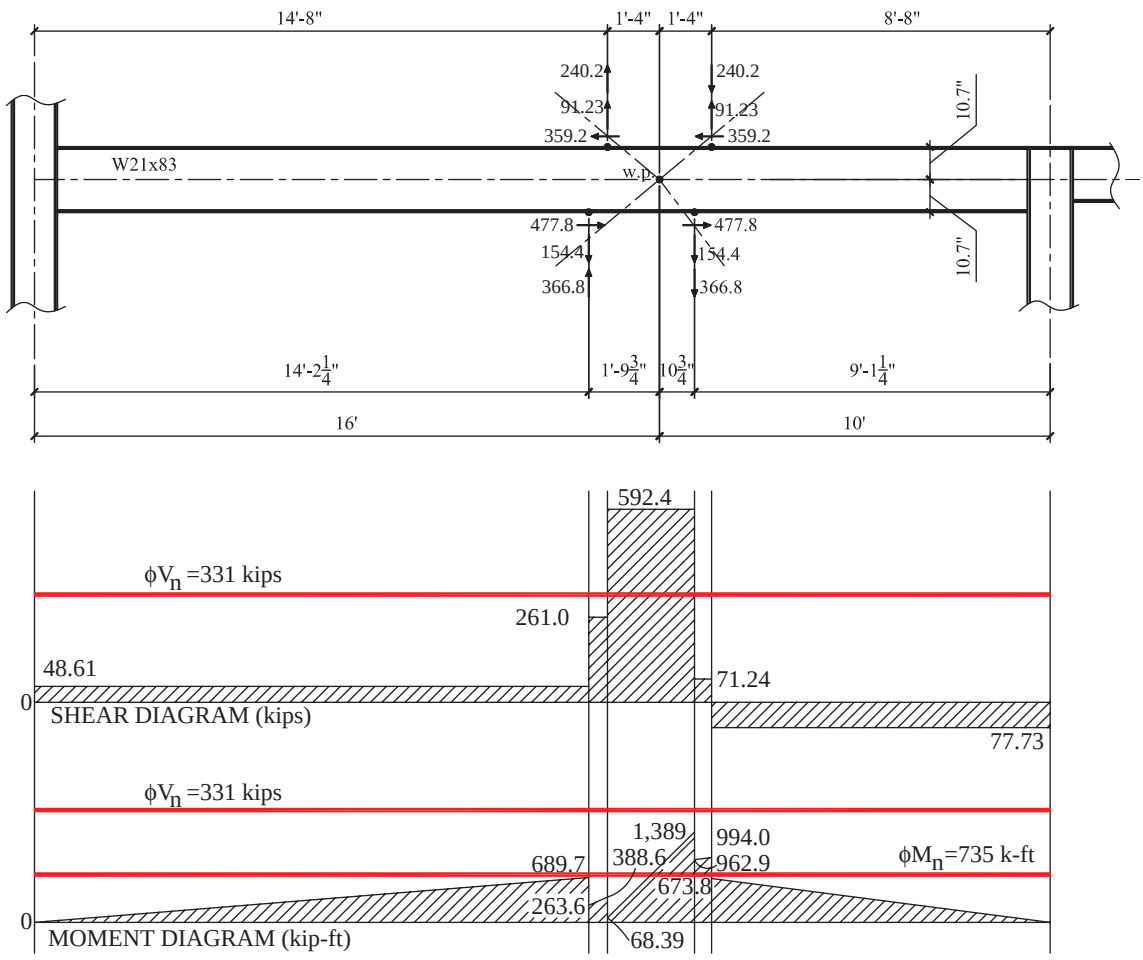

Fig. 29. Forces and moments acting at gusset-beam interfaces and beam shear and moment from brace forces: load case 4 for part 2 of Example 3.

moment strength equal to 331 kips and 735 k-ft, respectively. Thus, the beam is inadequate and has required strength to available strength ratios for shear and bending equal to 585/331 = 1.77 and 1,748/745 = 2.35, respectively. At the connection design stage, modifications to the beam would be required to increase both the shear and moment strength of the beam. Web doubler plates would be required to increase the beam shear strength. Cover plates, or some other manner of reinforcement would be required to increase the beam moment strength.

Based on the observations made here in part 2d, it is evident that the effect of the brace forces should be included when sizing the frame beam. Furthermore, the span of the beam and the location of the work point along the span of the beam should be considered when evaluating the frame beam.

Part 3a. *Select a trial beam size based on strength and deflection; include effects of brace forces using the rule of thumb presented previously.*

To obtain a trial beam size, the length of the gusset (L_g) and one-half the depth of the beam (e_b) are approximated using Equations 15 and 16. It was previously calculated that the gravity design load using load case 4 is 4.66 k-ft, and the beam shear and moment distribution is given in Figure 28. To determine the beam shear and moment distribution resulting from the brace forces, the moments and normal forces acting on the gusset-to-beam interfaces need to be approximated.

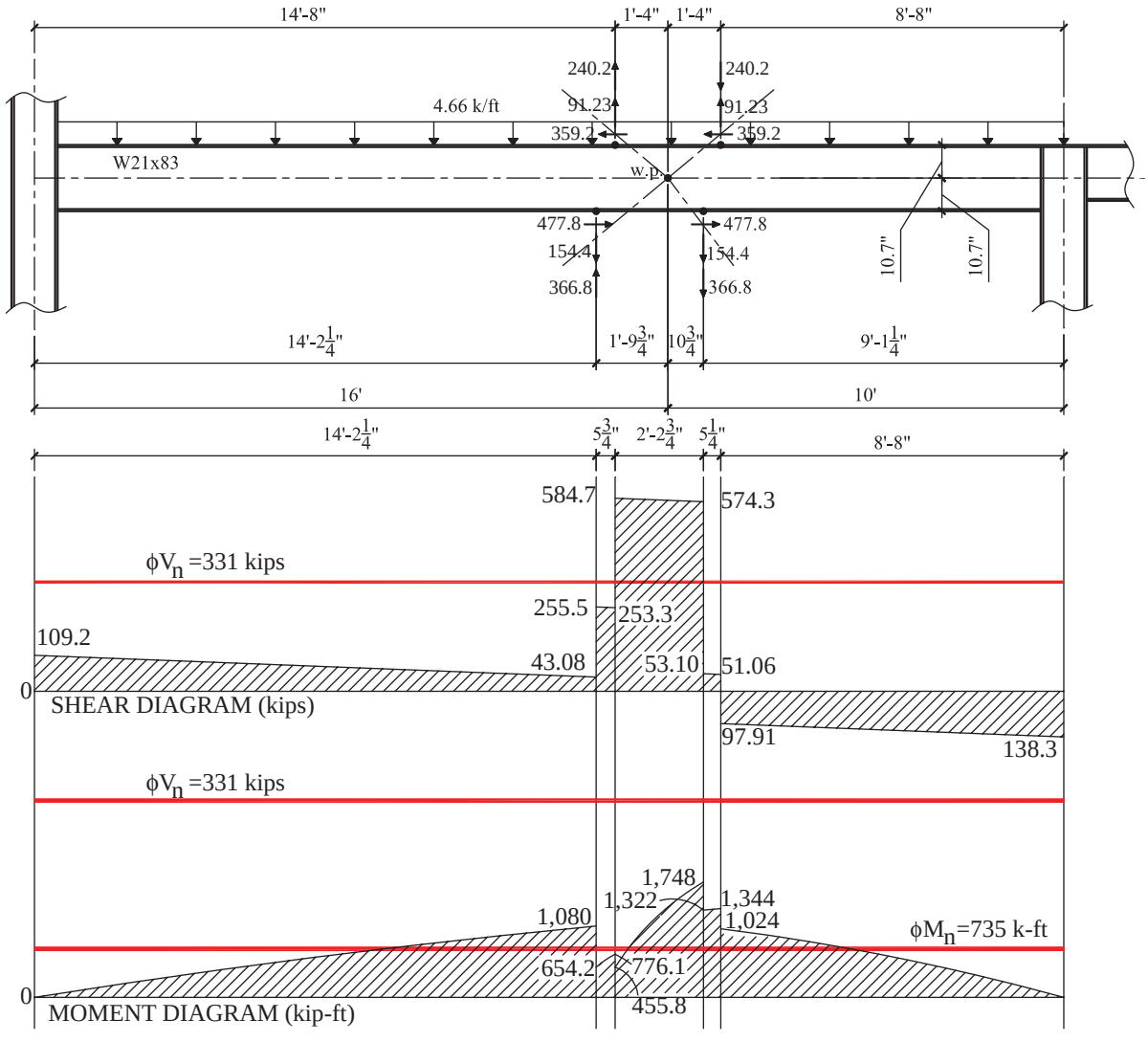

Fig. 30. Forces and moments acting at gusset-beam interfaces and beam shear and moment from gravity load plus brace forces: load case 4 for part 2 of Example 3.

Section* a-a—*top of beam:

$H_1 = 249.67$ kips
$H_2 = 468.61$ kips
$V_1 = 208.06$ kips
$V_2 = -390.51$ kips

The length of the gusset is approximated as:

$$L_{g,app} = \frac{L}{6} = \frac{(26 \text{ ft})(12 \text{ in./ft})}{6} = 52.0 \text{ in.}$$

One-half of the beam depth, e_b, is approximated as:

$$e_{b,app} = (0.375)(26 \text{ ft}) = 9.75 \text{ in.}$$

The approximated moment acting on section *a-a* at the top of the beam is:

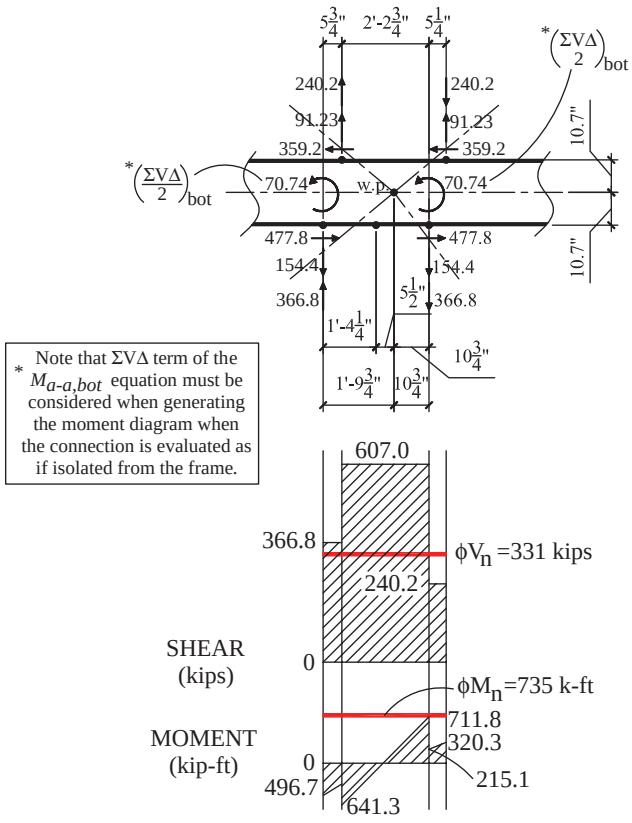

Fig. 31. Beam shear and bending if connection is evaluated as if isolated from the frame. Effect of brace forces only; part 2 of Example 3.

$$M_{a-a,app} = (H_1 + H_2)e_{b,app} = (249.67 + 468.61)(9.75) = 7{,}003.23 \text{ k-in.}$$
$$N_{eq,app} = \pm 0.375(249.67 + 468.61) = \pm 269.36 \text{ kips}$$

The horizontal force acting on section *a-a* is:

$$H_{a-a} = -(249.67 + 468.61) = -718.29 \text{ kips}$$

For each half gusset body, the horizontal force is $-718.29/2 = -359.15$ kips.

The normal force acting on section *a-a* from the unbalanced vertical force is:

$$V_{a-a} = -(V_1 + V_2) = -(208.06 - 390.51) = 182.45 \text{ kips}$$

For each half gusset body, the normal force is $182.45/2 = 91.23$ kips.

Section* a-a—*bottom of beam:

$H_1 = 445.57$ kips
$H_2 = 510.00$ kips
$V_1 = 371.31$ kips
$V_2 = -680.00$ kips

The length of the gusset is approximated as:

$$L_{g,app} = \frac{L}{6} = \frac{(26 \text{ ft})(12 \text{ in./ft})}{6} = 52.0 \text{ in.}$$

One-half of the beam depth, e_b, is approximated as:

$$e_{b,app} = (0.375)(26 \text{ ft}) = 9.750 \text{ in.}$$

The approximated moment acting on section *a-a* at the bottom of the beam is:

$$M_{a-a,app} = (H_1 + H_2)e_{b,app} = (445.57 + 510.00)(9.75) = 9{,}316.81 \text{ k-in.}$$
$$N_{eq,app} = \pm 0.375(445.57 + 510.00) = \pm 358.34 \text{ kips}$$

The horizontal force acting on section *a-a* is:

$$H_{a-a} = -(445.57 + 510.00) = -955.57 \text{ kips}$$

For each half gusset body, the horizontal force is −955.57/2 = −477.79 kips.

The normal force acting on section *a-a* from the unbalanced vertical force is:

$$V_{a-a} = -(V_1 + V_2) = -(371.31 - 680.00)$$
$$= 308.69 \text{ kips}$$

For each half gusset body, the normal force is 308.69/2 = 154.35 kips.

With the forces acting on the top and bottom interfaces approximated, the loading diagram used to obtain a trial beam size can be generated. Figure 32 shows the loading diagram and the resulting beam shear and moment diagrams based on load case 4 loads. Note that the approximation does not take into account any potential Δ values that would be present in the final connection design. Therefore, the resultant forces acting on the gusset-to-beam interfaces are symmetrically placed about the work point location at a distance equal to $L_g/4$ to either side of the work point (i.e., the resultant forces are separated by a total distance of $L_g/2$).

Referring to required beam shears and moments shown in the diagrams in Figure 32, and considering the minimum moment of inertia given in the problem statement, the following are the design parameters for the beam selection.

$V_{u,max}$ = 604.2 kips
$M_{u,max}$ = 1,729 k-ft
I_{min} = 1,282 in.^{4}
Target beam depth, d = (9.75 in.)(2) = 19.5 in.

For this solution, two possible beam sizes will satisfy the design parameters. The properties of the two beams are shown in Table 3. The W21×201 is the lighter of the two beams, but the W18×211 has a depth closer to the approximated depth of 19.5 in. Given that the W18 is only a few pounds heavier than the W21, but has a depth closer to the approximated depth, the W18×211 is selected as the trial beam size. Note that selecting the W21×201 is an acceptable choice, if that is the preference of the designer.

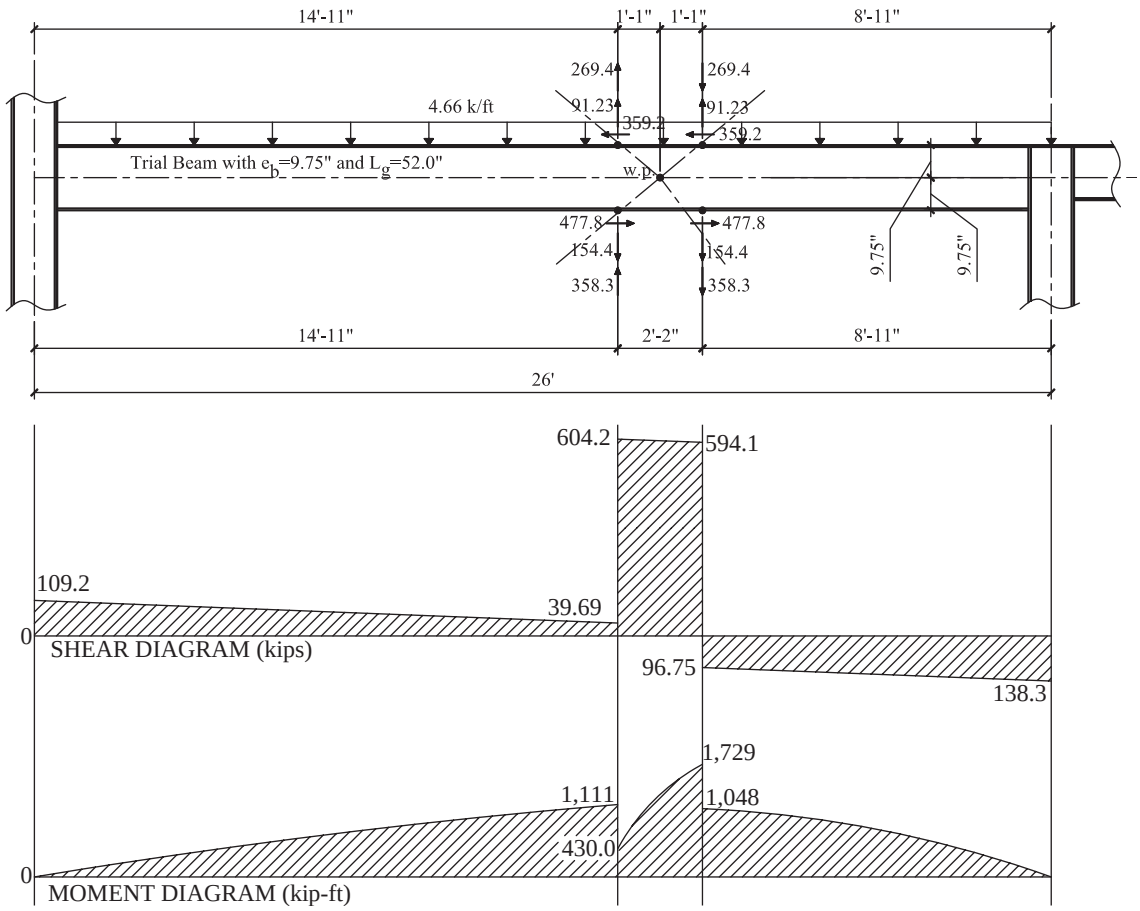

Fig. 32. Beam shear and bending for trial beam size: L_g *= 52.0 in.,* e_b *= 9.75 in.; part 3a of Example 3.*

Table 3. Possible Trial Beam Sizes for Part 3a of Example 3.				
Beam Size	ϕV_n **(kips)**	ϕM_n **(k-ft)**	I **(in.^{4})**	d **(in.)**
W21×201	629	1,990	5,310	23.0
W18×211	657	1,840	4,330	20.7

Try a W18×211.

Parts 3b and 3c. *Using the trial size selected in part 3a, calculate the brace connection force distribution on section* a-a. *Generate the beam shear and moment diagrams.*

A W18×211 has been selected for the frame beam. Knowing the loading, geometry and beam size, a gusseted brace connection can be designed. Figure 33 shows an elevation of the frame beam with the gusset geometry. Based on the geometry given in Figure 33, the brace force distributions at the gusset-to-beam interfaces can be calculated.

Section* a-a—*top of beam:

$$H_1 = 249.67 \text{ kips}$$
$$H_2 = 468.61 \text{ kips}$$
$$V_1 = 208.06 \text{ kips}$$
$$V_2 = -390.51 \text{ kips}$$

Forces acting on section* a-a*:

$$H_{a-a} = -(H_1 + H_2)$$
$$= -(249.67 + 468.61)$$
$$= -718.29 \text{ kips}$$
$$V_{a-a} = -(V_1 + V_2)$$
$$= -(208.06 - 390.51)$$
$$= 182.45 \text{ kips}$$
$$\Delta = \frac{1}{2}(L_1 - L_2) = 0.5(33.0 - 33.0)$$
$$= 0$$
$$e_b = 10.35 \text{ in.}$$
$$M_{a-a} = (V_1 + V_2)\Delta - (H_1 + H_2)e_b$$
$$= (208.06 - 390.51)(0)$$
$$-(249.67 + 468.61)(10.35)$$
$$= -7,434.27 \text{ kip-in.}$$

The couple of $M_{a\text{-}a}$ is:

$$N_{eq} = \pm\frac{(2)(7,434.27)}{66.0} = 225.28 \text{ kips}$$

Section* a-a—*bottom of beam:

$$H_1 = 445.57 \text{ kips}$$
$$H_2 = 510.00 \text{ kips}$$
$$V_1 = 371.31 \text{ kips}$$
$$V_2 = -680.00 \text{ kips}$$

Forces acting on section* a-a*:

$$H_{a-a} = -(H_1 + H_2) = -(445.57 + 510.00)$$
$$= -955.57 \text{ kips}$$
$$V_{a-a} = -(V_1 + V_2) = -(371.31 - 680.00)$$
$$= 308.69 \text{ kips}$$
$$\Delta = \frac{1}{2}(L_1 - L_2) = 0.5(38.5 - 27.5)$$
$$\Delta = 5.50 \text{ in.}$$
$$e_b = 10.35 \text{ in.}$$
$$M_{a-a} = (V_1 + V_2)\Delta - (H_1 + H_2)e_b$$
$$= (371.31 - 680.00)(5.50)$$
$$-(445.57 + 510.00)(10.35)$$
$$= -11,587.94 \text{ kip-in.}$$

The couple of $M_{a\text{-}a}$ is:

$$N_{eq} = \pm\frac{(2)(11,587.94)}{66.0} = 351.15 \text{ kips}$$

The force distributions at the gusset-to-beam interfaces are shown in Figure 34 along with the beam shear and moment diagrams resulting from load case 4.

Part 3d. *Compare required to available beam shear and moment strengths.*

The W18×211 is adequate for the required beam shear and bending. When the beam was selected based on gravity load effects only, the beam was found to be woefully inadequate for shear and moment. When the brace force distribution is considered in combination with the gravity load effects, a satisfactory beam is selected eliminating any need for web doubler plates, cover plates, or any other type of reinforcement. The method presented (rule of thumb) for approximating the moment at the gusset interface provides an adequate

method for accounting for the effects of the brace forces during the beam selection process.

Parts 4a and 4b. *Determine the required beam web doubler for the shear distribution shown in Figure 30. Check assuming (a) resultant force distribution on section* a-a*, and (b) distributed uniform force distribution on section* a-a

Figure 30 shows the beam shear diagram using the resultant force method. Referring to Figure 30, the maximum shear is 584.7 kips and is constant over the region from 14 ft 8 in. to 16 ft 10¾ in. from the left support. The available shear strength of the beam is 331 kips. Therefore, a web doubler plate is required. The required web doubler thickness is:

$$\phi V_n = (1.0)(0.6)(50)(21.4)(0.515 + t_d) \geq 584.7$$
$$= 330.63 + 642t_d \geq 584.7$$
$$t_d \geq \frac{584.7 - 330.63}{642} = 0.396 \text{ in.}$$

Use a ½ in. web doubler plate.

The web doubler plate must be within the region of the beam where the shear is 584.7 kips. Since the shear is constant over this region, the web doubler plate must be extended beyond this region a distance sufficient to get the load into the web doubler plate (see Figure 35). The shear required to be carried by the web doubler is 584.7 – 331 = 253.7 kips. Therefore, the shear on the horizontal edges of the web doubler plate is:

$$V_h = \frac{(253.7 \text{ kips})(26.75 \text{ in.})}{19.73 \text{ in.}} = 344.0 \text{ in.}$$

The length required to transfer the load into the doubler plate (i.e., develop the doubler plate) is the length, x (see Figure 35), of the ½-in.-thick web doubler plate required to develop the web doubler plate for a shear equal to one-half of the shear force acting on the horizontal edge of the web doubler plate and is calculated as shown below.

$$x = \frac{\left(\frac{344.0 \text{ in.}}{2}\right)}{(1.0)(0.60)(50 \text{ ksi})(0.5 \text{ in.})} = 11.46 \text{ in.}$$

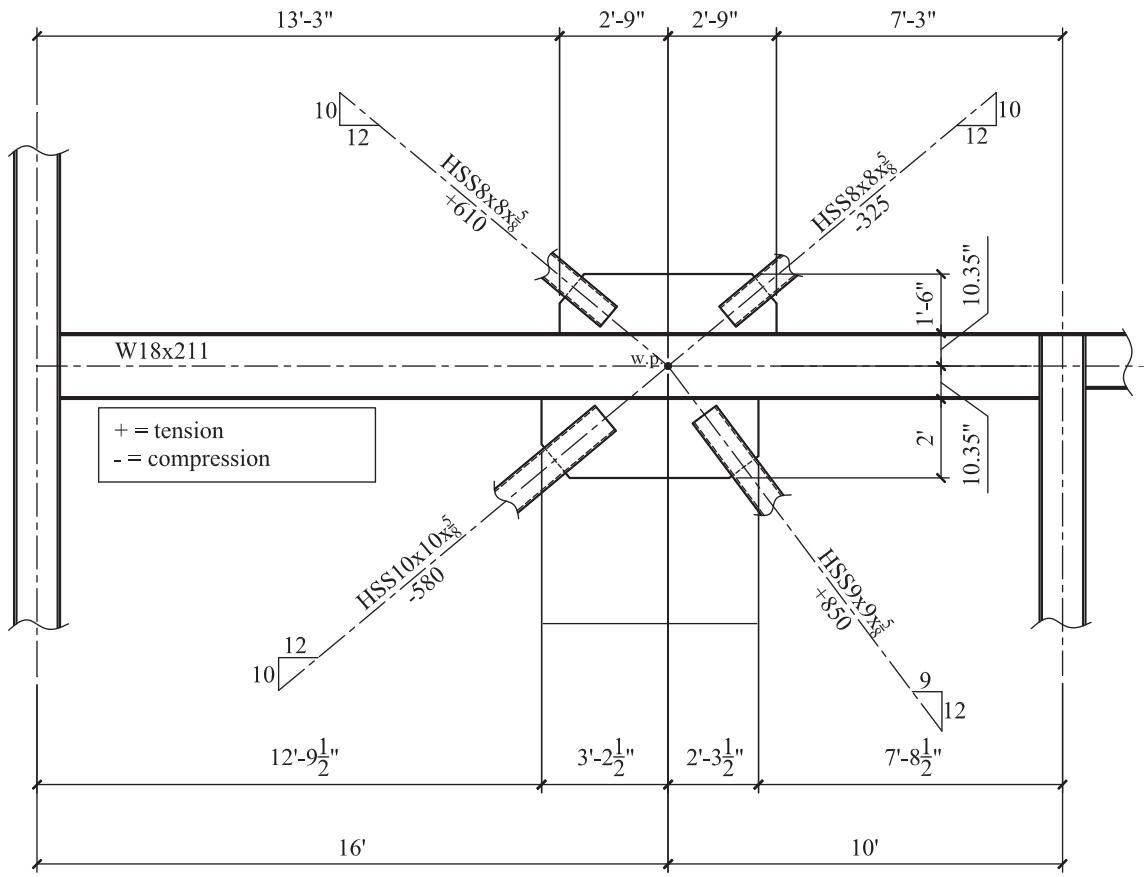

Fig. 33. Brace and gusset geometry for trial W18×211 *frame beam; part 3b of Example 3.*

The web doubler plate requires a development length of 11.5 in. to each side of the region of the beam where the beam's available shear strength is required (see Figure 35).

Figure 36 shows the beam shear diagram when the brace force distribution acting on the gusset-to-beam interfaces are uniformly distributed. Note that the maximum beam shear is 523.9 kips, compared to a maximum shear of 584.7 kips when the resultant force method is used (see Figure 30). As discussed previously, the difference in the maximum shear is due to the non-zero Δ parameter associated with the geometry of the bottom flange gusset. As can be seen in Figure 36, the beam's available shear strength is exceeded over a 2 ft 0-¾ in. portion of the beam starting at 14 ft 6 13⁄16 in. from the left support. A web doubler plate is required in this region. The required web doubler plate thickness is:

$$\phi V_n = (1.0)(0.6)(50)(21.4)(0.515 + t_d) \geq 523.9$$
$$= 330.63 + 642 t_d \geq 523.9$$
$$t_d \geq \frac{523.9 - 330.63}{642} = 0.301 \text{ in.}$$

Use a ⅜-in. web doubler plate.

Referring back to Figure 35, recall that the web doubler plate is required to be developed in order to get the load out of the beam and into the web doubler plate. Because the beam shear shown in Figure 30 is approximately constant over the region where the beam's available strength is exceeded, the web doubler plate needs to be developed outside of this region. However, when the distributed force method is used, the web doubler plate does not need to be developed outside

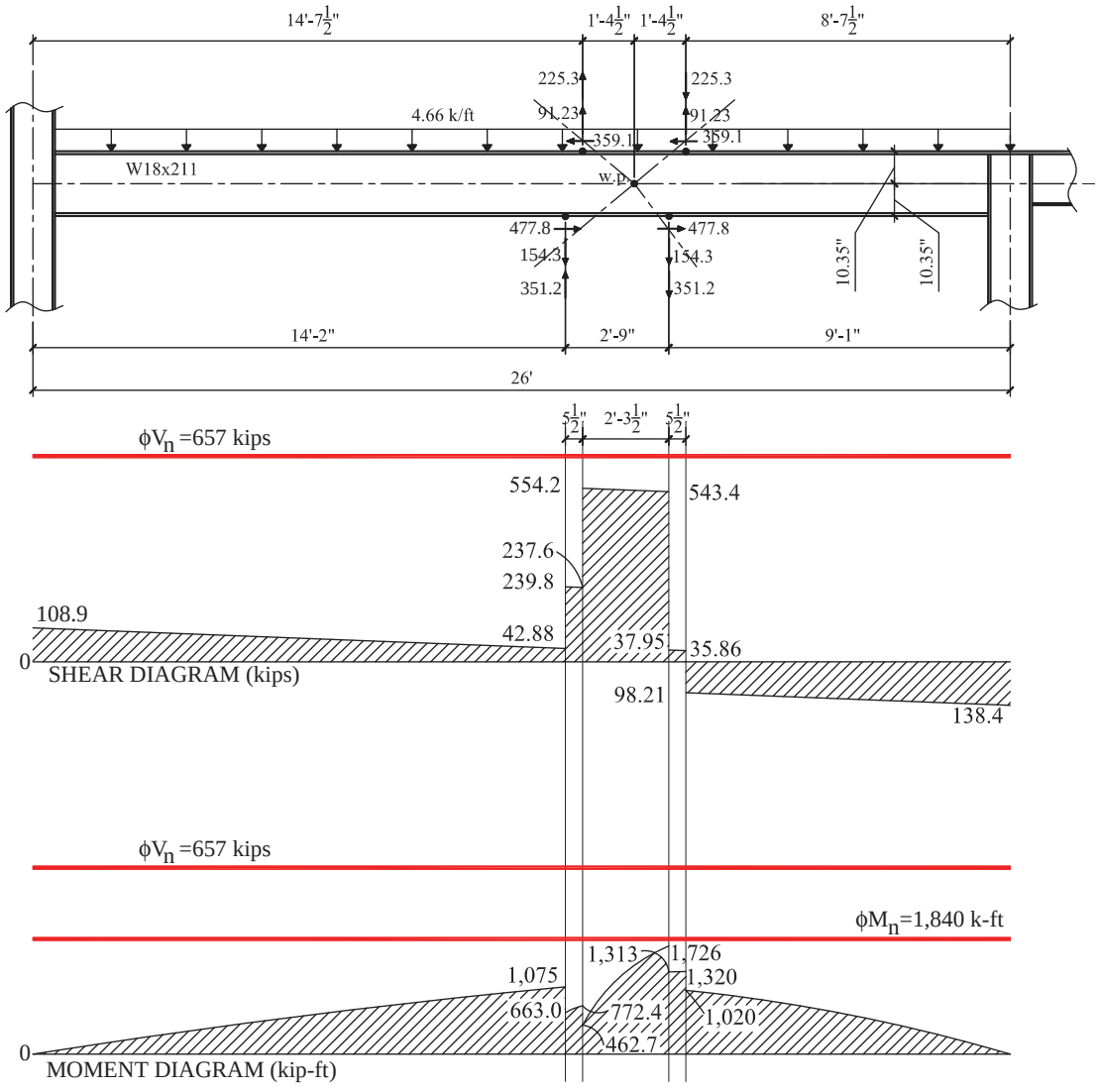

Fig. 34. Force distribution and beam shear and moment diagrams with W18×211 *frame beam; part 3c of Example 3.*

of the region where the beam's available shear strength is exceeded.

For this example, when the resultant load method is used, a ½-in. × 49.75-in. web doubler plate is required. When the distributed load method is used, a ⅜-in. × 24.75-in. web doubler plate is used. Using the distributed load method will always result in a more economical web doubler plate, relative to the resultant load method. Considering that the distributed load method is a more accurate analysis method, it is recommended that the distributed load method be used when evaluating the need for web doubler plates. It's worth noting that if the effects of the brace forces on the frame beam are appropriately considered, an appropriate beam size will be selected (as in part 3 of this example), making the discussion of web doubler plates moot.

SUMMARY

1. A method for generating an admissible force distribution in a chevron gusset connection has been presented. The analysis procedure uses the gusset-to-beam interface as a control section. The analysis procedure identifies both a horizontal critical section (gusset-to-beam interface) as well as a vertical critical section (section *b-b*). A set of equations for calculating the forces and moments acting on the two critical sections is provided.
2. Today's standard procedure during the connection design process used in chevron brace connection design is to evaluate the brace force effects on the beam as if the joint is isolated from the frame. When braced frame geometry and loading is such that the summation of the vertical components of the brace forces is zero (a balanced force),

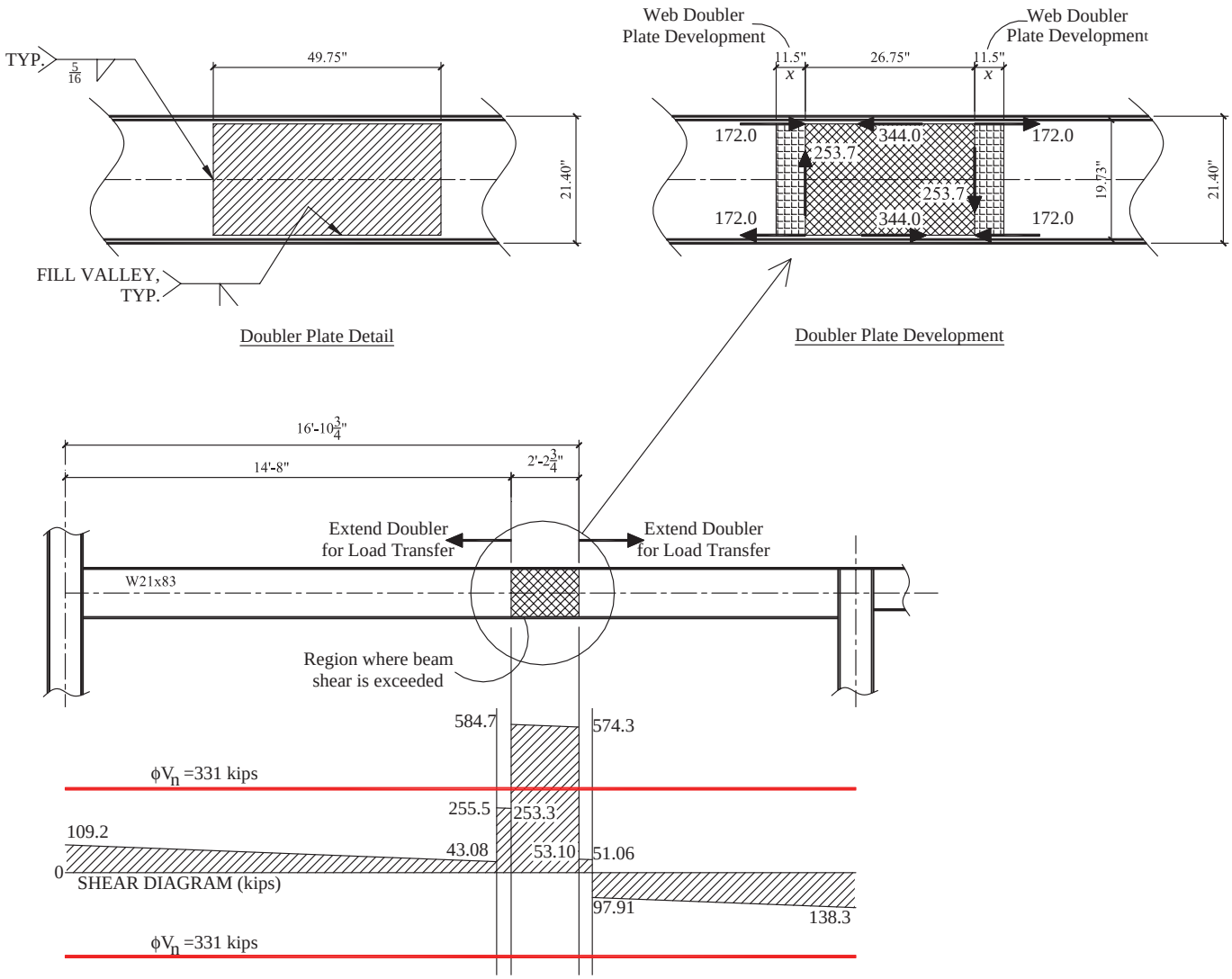

Fig. 35. Web doubler plate detail using the resultant load method.

this is an acceptable practice, regardless of the span of the beam or the location of the work point along the span of the beam.

3. When the braced frame geometry and loading is such that the summation of the vertical components of the brace forces is non-zero (an unbalanced force), the chevron effect must be evaluated. Because of the chevron effect, it is not adequate to evaluate the brace force effects on the beam as if the joint is isolated from the frame. The span of the beam as well as the location of the work point along the length of the beam must be considered.

   a. The maximum beam shear and moment can be over- or underestimated if the joint is evaluated as if it is isolated from the frame.

   b. Maximum beam shear and moment may be located within or outside of the connection region. Thus, the beam should not be evaluated as if the connection is isolated from the frame.

4. The effect of the brace forces on the beam should be considered during the process of making final member size selection. At this stage of design, information regarding connection geometry may not be known. An approximate method for estimating the brace force distribution at the gusset-to-beam interface has been presented. An example problem was provided demonstrating the application of the method during the member design process.

5. Two methods for distributing the section *a-a* forces were presented; the resultant method and the distributed method. The resultant method is a simplified method recommended to be used during the beam size selection process. The distributed method should be used for (a) the design of the gusset and the gusset-to-beam weld and (b) evaluating the required web doubler thickness as well as the portion of the beam where a web doubler should be provided.

6. If the effect of chevron brace forces is evaluated properly during the beam size selection process, the need for, and costs associated with, beam web doubler plates can be eliminated.

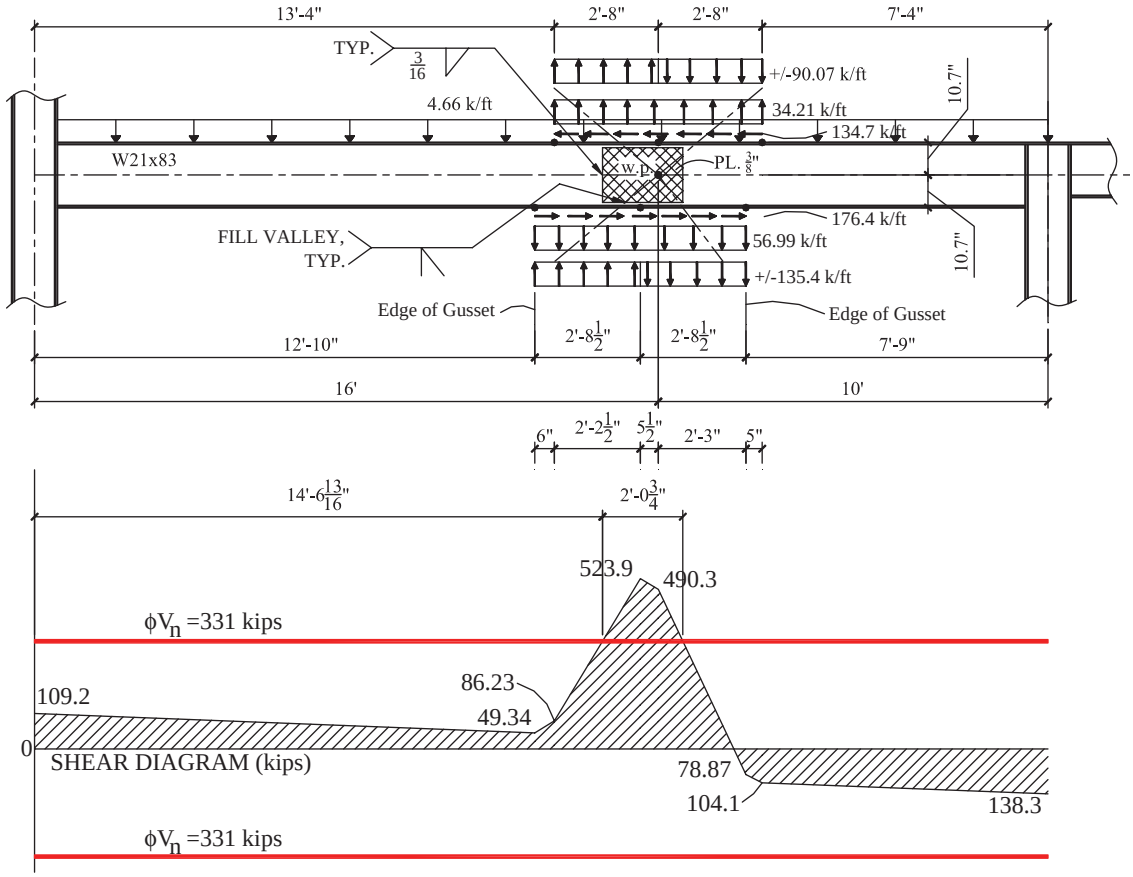

Fig. 36. Web doubler plate detail using the distributed load method.

SYMBOLS

A_g	The gross cross-sectional area of a framing member
D	Service level dead load (gravity)
F_{cre}	Critical stress calculated from *Specification* Chapter E
F_y	Nominal specified yield strength
H_1	The horizontal component of force in brace 1
H_2	The horizontal component of force in brace 2
$H_{a\text{-}a}$	The horizontal (shear) force acting at the gusset-to-beam interface
H_{bi}	The horizontal (normal) force acting on the critical vertical section of the gusset
I_x	Moment of inertia about bending axis
L_1	The horizontal distance from the left edge of the gusset to the work point
L_2	The horizontal distance from the right edge of the gusset to the work point
L	Service level live load (gravity)
L	Span of frame beam
L_g	The contact length of the gusset-to-beam interface
$L_{g,app}$	Approximation of length of gusset, L_g
$M_{a\text{-}a}$	The moment acting at the gusset-to-beam interface
$M_{a\text{-}a,app}$	Approximation of moment, $M_{a\text{-}a}$
M_{bi}	The moment acting on the critical vertical section of the gusset
M_{beam}	The moment in the frame beam
M_n	The nominal available flexural strength
M_u	The required (design) moment strength
$M_{u,max}$	The maximum required (design) flexural strength
N_{eq}	The couple of the moment, $M_{a\text{-}a}$
$N_{eq,app}$	Approximation of the couple of the moment, $M_{a\text{-}a}$
P_1	The axial force in brace 1
P_2	The axial force in brace 2
P_b	The buckling strength of brace in compression, $1.14F_{cre}A_g$
R_y	The ratio of expected yield stress to the specified minimum yield stress, F_y
V_1	The vertical component of the force in brace 1
V_2	The vertical component of the force in brace 2
$V_{a\text{-}a}$	The vertical (normal) force acting at the gusset-to-beam interface
V_{beam}	The shear in the frame beam
V_{bi}	The vertical (shear) force acting on the critical vertical section of the gusset
V_n	The nominal available shear strength
V_u	The required (design) shear strength
$V_{u,max}$	The maximum required (design) shear strength
W	Service level wind load
Z	The plastic section modulus
d	depth of frame beam
e_b	The perpendicular distance from the gusset interface to the gravity axis of the frame beam
$e_{b,app}$	Approximation of length of half-depth of the frame beam
h	The vertical dimension of the gusset
n_{eq}	The couple of the moment, $M_{a\text{-}a}$, per unit length of gusset
w_D	LRFD dead load (gravity)
w_L	LRFD live load (gravity)
w.p.	The brace work point
w_u	LRFD (design) uniform gravity load
Δ	The horizontal misalignment between the work point and the centroid of the gusset-to-beam interface
ΣH_i	The summation of horizontal brace force components
ΣV_i	The summation of vertical brace force components
δ	Beam deflection
ϕ	LRFD strength reduction factor

REFERENCES

AISC (2010a), *Seismic Provisions for Structural Steel Buildings,* ANSI/AISC 341-10, American Institute of Steel Construction, Chicago, IL.

AISC (2010b), *Specification for Structural Steel Buildings,* ANSI/AISC 360-10, American Institute of Steel Construction, Chicago, IL.

AISC (2011a), *Design Examples,* v.14.1, American Institute of Steel Construction, Chicago, IL.

AISC (2011b), *Steel Construction Manual,* 14th ed., American Institute of Steel Construction, Chicago, IL.

ASCE (2010), *Minimum Design Loads for Buildings and Other Structures,* ASCE 7-10, American Society of Civil Engineers, Reston, VA.

Steel Structures Research Update

Resilient Steel Plate Shear Walls

Second Quarter 2015

JUDY LIU

INTRODUCTION

Presented here are some highlights from a comprehensive, innovative and international study on resilient steel plate shear walls. The research capitalizes upon the high strength, elastic stiffness and energy dissipating capabilities of steel (a.k.a. special) plate shear walls, with steel web plates and boundary elements, to create more efficient, robust and economical systems. For example, the seismic force resisting system is reimagined as a recentering and easily repairable steel plate shear wall.

The research has also capitalized upon the expertise as well as computational and experimental capabilities of a team from Taiwan and across the United States. The research was conducted through the George E. Brown Network for Earthquake Engineering Simulation (NEES), funded by the National Science Foundation (NSF) with supplementary support from AISC. The research team is led by Professor Jeffrey Berman at University of Washington (UW). Key personnel from UW include Professor Laura Lowes, Dr. David Webster, now a Senior Associate at Thornton Tomasetti, and Dr. Patricia Clayton, now a professor at the University of Texas at Austin. Lead researchers from the University of Illinois at Urbana-Champaign (UIUC) are Professor Larry Fahnestock and Dr. Daniel Borello, now on the faculty at Oregon State University. Collaborators from the University at Buffalo (UB) include Professor Michel Bruneau and Dr. Daniel Dowden, now the Structural Engineer at the UB Structural Engineering and Earthquake Simulation Laboratory (SEESL). Professor Keh-Chyuan Tsai and Research Fellow Chao-Hsien Li have led the work at the National Center for Research on Earthquake Engineering (NCREE) in Taiwan. The research team received extensive additional support from student research assistants and technical staff, and these contributions are acknowledged in the cited documents.

Steel plate shear wall (SPSW) research has been active for over 30 years, and progress toward more widespread implementation is being made (Berman, 2014). The stiff and ductile system relies on yielding of tension strips after buckling of the web plates and yielding at the beam ends and at the column bases. Seismic design provisions for special plate shear walls are in the ANSI/AISC 341-10, and documents such as the AISC *Design Guide 20* (Sabelli and Bruneau, 2006) provide a framework for ductile design and detailing. Notable projects in the United States include the U.S. Federal Courthouse in Seattle (Seilie and Hooper, 2005) and the 56-story L.A. Live Hotel & Residences, the first SPSW high-rise building in Los Angeles (AISC, 2008).

The recently completed collaborative research has contributed to the state of the art with deeper investigations into the complex behavior of the web plates and boundary elements of SPSWs, creation of more efficient and resilient SPSWs, and development of validated performance-based design guidelines for those new systems. Highlighted here are research on the SPSW web plate stress field, studies on coupled SPSWs, investigation of self-centering SPSWs, modeling of the web plates for self-centering SPSWs and the viability of web plates connected only to the beams in the self-centering SPSWs.

SPSW WEB PLATE STRESS FIELD

The angle of inclination of the tension field in the web plate may change with inelastic response. Designs following the current provisions utilize a tension field inclination angle equation derived from elastic analysis. A computational and experimental evaluation of SPSWs was undertaken to examine the web plate stress field and to evaluate the interaction with the boundary elements (Figure 1a and 1b) (Webster et al., 2014).

The experimental program, which was conducted in the Structural Research Laboratory at the University of Washington, included tests on web plates anchored to a pin-connected frame. Specimens were subjected to either a monotonically increasing load to 6% lateral drift or cyclic loading up to 4% drift. An OptoTrak optical measurement system was utilized to measure deformations, including out-of-plane deflections, of the web plate and boundary elements. OptoTrak measurements, as well as strain gage data,

Judy Liu, Ph.D., Research Editor of the AISC Engineering Journal, Associate Professor of Civil Engineering, Purdue University, West Lafayette, IN. Email: jliu@purdue.edu

indicated for both types of loading that the tension field migrates from a relatively low angle of inclination (e.g., 37°) in the elastic range to an angle of 45° when inelastic and approaching 4% drift (Figure 1c and 1d).

The experimental results were confirmed with finite element analyses, and the finite element models were used in a parametric study on web plate inclination angle for a number of subassemblages of multi-story SPSWs. The frames used in the parametric study utilized various wide-flange horizontal boundary element (HBE) and vertical boundary element (VBE) sizes. At seismic drift levels, the angle ranged between 43° and 45°; the angle was independent of SPSW geometry and boundary element sizes. A constant angle of 45° is recommended for design, for simplicity and only slight conservatism with respect to demands on the VBE (Webster et al., 2014).

Additional work produced valuable information about the inelastic cyclic response of the web plates. One observation was that the compressive stresses are non-negligible and can affect load capacity and demands on the VBEs. A phenomenological material model developed by Webster (2013) for use in strip models of the plates captures this and other complex web plate behavior. The model has been put to good use in modeling for self-centering SPSWs, as summarized in a later section.

COUPLED SPSWs

A natural step in the research was to investigate the topic of coupled SPSWs, building upon the stiffness and energy dissipation of the SPSW and taking advantage of common architectural layouts that are well-suited for the coupled wall configuration. SPSWs are typically placed in pairs around passageways at the core of the building, so replacing the floor framing in between the walls with coupling beams to create an SPSW with coupling (SPSW-WC), shown in Figure 2, can increase the efficiency and effectiveness of the system.

The SPSW-WC study was comprised of a number of subtasks. Development of a design methodology, creation of validated component and subassembly models and nonlinear analysis of SPSW-WC models allowed for understanding of the behavior and design of SPSW-WCs. Parameters such as degree of coupling were studied computationally. The SPSW-WC study culminated in a large-scale experimental validation of the SPSW-WCs and the proposed design procedures.

The SPSW-WCs utilize the same capacity design methodology as in the AISC *Seismic Provisions* (AISC, 2010a). The behavior and strength of the system is largely governed by web plate buckling and development of tension field action. Aside from plastic hinges at the ends of the HBEs, the HBEs and VBEs are designed to remain elastic. The coupling

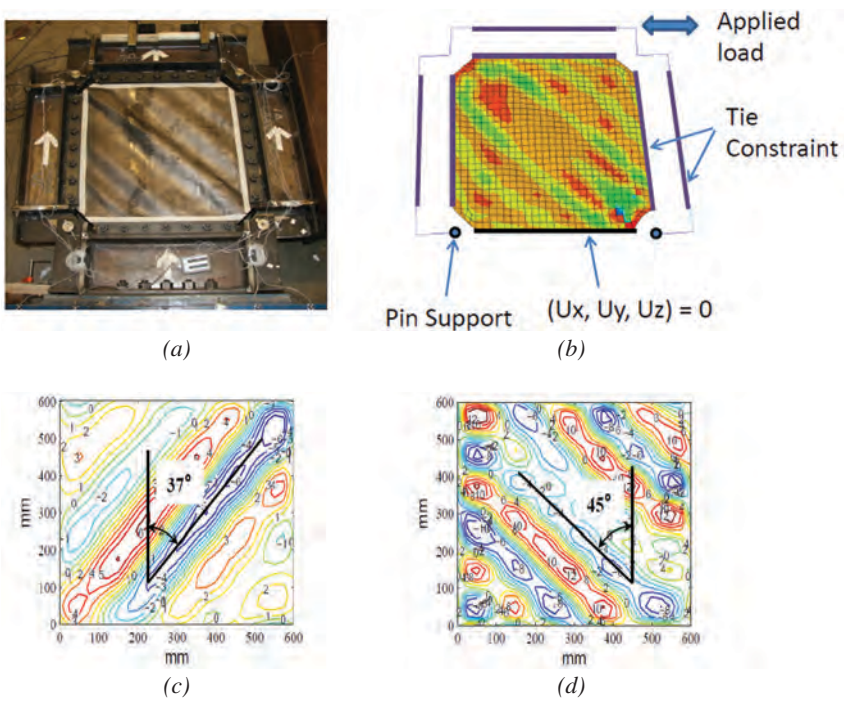

Fig. 1. Tension field inclination angle study: (a) typical test specimen, (b) finite element model, (c) inclination angle derived from Optotrak test data at 0.4% drift (d) inclination angle derived from Optotrak test data at 3.75% drift.

beams (CBs) can develop flexural or shear plastic hinges, or some combination. With the frame action provided by the CBs, the efficiency is improved relative to two independent SPSWs, and the web plate thicknesses and boundary element sizes can be reduced.

A number of 6- and 12-story prototype SPSW-WC office buildings were designed for Los Angeles, California, using both the equivalent lateral force (ELF) procedure and the inelastic lateral force (ILF) procedure (Chao et al., 2007; Ghosh et al., 2009). The square, five-bay buildings were based on plan dimensions of the SAC nine-story building (FEMA, 2000). Designs included single SPSWs (PLANAR), SPSW-WCs with intermediate flexural/shear yielding coupling beams (INT), SPSW-WCs with flexural yielding coupling beams (FLEX) and pairs of uncoupled SPSWs (UNCOUP). This resulted in eight combinations of configuration and design procedure for the 6-story prototypes and six combinations for the 12-story prototypes; the UNCOUP design was not feasible for the 12-story building (Borello and Fahnestock, 2013).

These prototype structures were evaluated using static and dynamic nonlinear analysis procedures. The models were validated against existing experimental data for assemblies such as a large-scale, four-story SPSW tested by Driver et al. (1997) and link beams tested by Lewis (2010). Tension strips were used to represent the web plates. Fiber elements were used to model the boundary elements and coupling beams. Details of the formulations and constitutive relationships are provided in Borello and Fahnestock (2013).

Nonlinear static pushover analyses demonstrated that all prototype configurations had comparable stiffness. The ultimate strengths of the PLANAR configurations were similar to those for the SPSW-WC configurations. The SPSW-WC ultimate strength is similar for different levels of coupling, and the values are slightly higher for the systems with the INT coupling beams as compared to the FLEX coupling beams. The higher degree of coupling also results in a lighter system. The UNCOUP prototypes exhibited the highest strength, but typically because of larger member sizes selected to satisfy lateral drift limits.

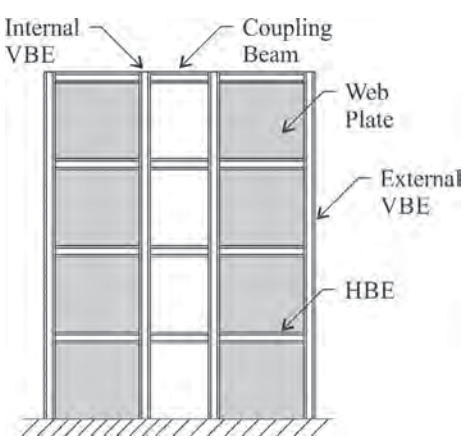

Fig. 2. Schematic of an SPSW-WC.

Nonlinear time history analyses revealed that the prototypes designed using ELF failed to satisfy lateral drift limits for the design-level ground motions (10% probability of exceedance in 50 years). Use of the ILF produced designs with better story drift performance. Regardless, the results also demonstrated that the more efficient (lighter) SPSW-WCs performed similarly to or better than the uncoupled systems. In addition, code-based seismic design parameters (R, Ω_0 and C_d) that are currently being used for the conventional uncoupled SPSW configuration (ASCE, 2010) appear to be appropriate for the SPSW-WC configuration.

The analyses also confirmed that the web plates in the SPSW-WCs have similar demands compared to SPSWs. Based on prior research, the SPSW-WCs are also expected to have similar levels of ductility and energy dissipation. Coupling beam rotation demands are also expected to be satisfied. Additional parametric studies of 6- and 12-story prototype structures were used to explore degree of coupling. Results demonstrated weight savings of as much as 40% for a 12-story SPSW-WC, as compared to an uncoupled pair of SPSWs. For the cases studied, the most efficient designs occurred within a range of degree of coupling (DC) from 0.4 to 0.6. A simple equation for determining DC for design was also developed (Borello and Fahnestock, 2012).

Important parameters for the experimental investigation were degree of coupling and coupling beam yield mechanism, either flexure or combined flexure and shear. Two approximately half-scale specimens, one FLEX (DC around 0.2) and one INT (DC around 0.4), were tested at UIUC (Borello et al., 2014). The HBEs had reduced beam section (RBS) connections. The coupling beams in the INT specimens were about twice as strong as those in the FLEX specimen, with 87 pounds additional coupling beam weight leading to 705 pounds of weight savings in the INT specimen VBEs.

The three-story specimens, which were tested in the NEES MUST-SIM facility at the University of Illinois at Urbana-Champaign, were anchored to the strong floor, braced at floor levels and secured to load and boundary condition box (LBCB) platens at the top (Figure 3). The specimen configurations and demands were based on the bottom three stories of the six-story prototype buildings. Therefore, vertical load and moment were applied in force control at the LBCBs, while increasing cycles of lateral displacement were applied in displacement control. The tests were used to confirm the expected global response, limit states, progression of yielding, design and detailing procedures for the SPSW-WCs.

The specimens performed well, with good energy

dissipation and high initial stiffness. Buckling in the web plates was first observed in the FLEX specimen at 0.25% top drift. Some flaking of whitewash in the web plates and second-floor coupling beam occurred in the first cycle at 0.5% drift. The coupling beams developed flexural hinges, as well as minor flange local buckling and more significant web local buckling near the connections at 2.5% drift. Complete fracture through the second-floor coupling beam occurred in the first negative excursion to 4% drift. Subsequent cycles at 4% saw fracture between a VBE and base plate, causing a drop in load, and then complete fracture of the third-story coupling beam.

The INT specimen had elastic buckling in the web plates at 0.1% drift. Flexural hinges formed in the VBE bases at 1% drift. At 1.5% lateral drift, shear yielding and flexural hinges in the HBEs were apparent, with flange local buckling occurring after 2% drift. Fractures appeared at the HBE flange local buckling regions in the 3.5% drift cycles, but the HBEs remained intact, and there was no appreciable overall loss in strength. At 4% drift, after repeated cycling at this limit of the actuator stroke, there was fracture between a VBE and base plate. The coupling beams exhibited distributed shear yielding and remained intact with no signs of fracture initiation even after the demanding loading protocol.

Although both specimens were designed for the same prototype building, the INT specimen was 17% lighter, initially 12% stiffer, and 10% stronger, with greater energy dissipation (Figure 4). Compared to that of the FLEX specimen, the INT specimen energy dissipation was slightly higher (in the range of 5% to 17% per cycle), but both specimens exhibited robust behavior with over 20% equivalent viscous damping in the 4% drift cycles. The experiments confirmed the viability of SPSW-WCs and demonstrated the importance of the coupling beam design for both seismic performance and economy. A SPSW-WC design with degree of coupling near the optimal and coupling beams dominated by shear yielding provides the lightest weight system with the most favorable cyclic behavior. In general, the SPSW-WC configuration was shown to provide excellent ductility and energy dissipation with only minor pinching, and it is a promising configuration that has the potential to significantly expand the range of application for SPSWs.

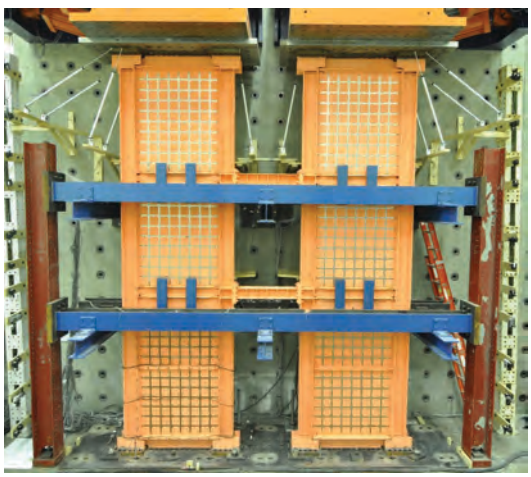

Fig. 3. SPSW-WC INT specimen before testing.

SELF-CENTERING SPSWs

Within this coordinated study, self-centering steel plate shear walls (SC-SPSWs) were envisioned as a more resilient and economical lateral force resisting system than even the ductile SPSWs. The SC-SPSWs would have recentering capability and yielding would be limited to the steel plates. The elimination of residual drift and the use of easily replaceable steel plates as seismic fuses would help to reduce repair costs after an earthquake.

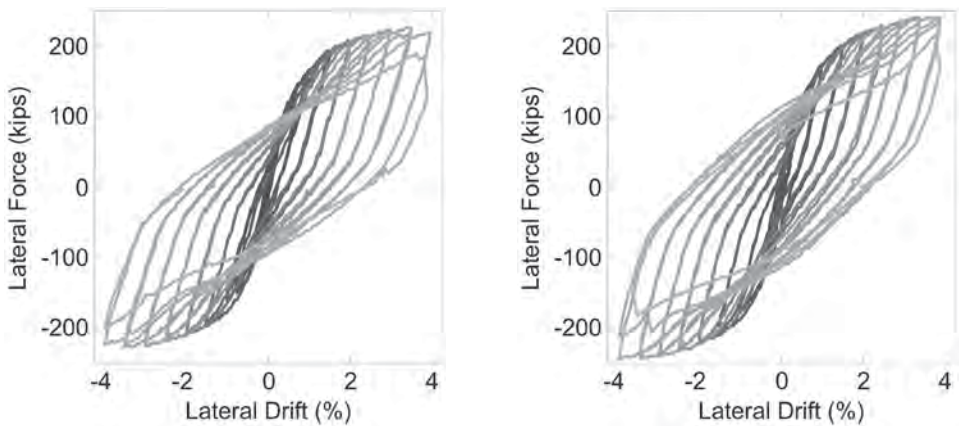

Fig. 4. Force-drift for (a) FLEX and (b) INT specimens.

Performance objectives for SC-SPSWs were established such that no repair would be required after an earthquake with 50% probability of exceedance in 50 years (50/50). After a 10% in 50 year earthquake (10/50), the recentered SC-SPSWs would require repair only to the web plates. Collapse prevention performance would be achieved for a 2% in 50 year earthquake (2/50) (Clayton et al., 2012b).

For the performance objective of recentering after an earthquake, a residual drift limit of 0.2% was set. This drift level follows the AISC Code of Standard Practice and its limit for acceptable column out-of-plumbness in new construction (AISC, 2010b).

The SC-SPSW uses post-tensioned (PT) beam-column and column base connections. These connections provide recentering capability without yielding in the frame members. As in prior research on self-centering moment resisting frames (SC-MRFs) (e.g., Christopoulos et al., 2002; Garlock et al., 2005; Chi and Liu, 2012), the post-tensioned strands or bars provide an initial clamping force. Decompression rotation of the connection and elastic elongation of the strands provides softening behavior without yielding or damage. The connections rotate, or rock, about both flanges. In the SC-MRFs, rocking about the top or bottom beam flange results in expansion of the frame along the centerlines of the girders. This type of flange-rocking (FR) connection, was investigated as part of the SC-SPSW. The NewZ-BREAKSS (NZ) connection was also investigated. The NZ connection rocks always about the top flange and was developed to eliminate the frame expansion observed for the FR connections with the tradeoff being reduced connection strength and stiffness (Dowden and Bruneau, 2011).

A number of validation tests were conducted on the SC-SPSWs at UW and UB. These included quasi-static cyclic tests on subassembly and third-scale three-story specimens. A number of parameters were investigated, such as different connection types including the FR and NZ connections. Those tests demonstrated the SC-SPSW's ability to recenter while maintaining ductile yielding and energy dissipation through tension field action in the web plates (Dowden et al., 2012; Clayton et al., 2012a, 2012b). Shake table tests were also conducted on three-story specimens. Test specimens included full SC-SPSW as well as bare frames with the FR and NZ connections. The test results confirmed the viability of the SC-SPSW, with both connections, for resisting demands with recentering (Dowden and Bruneau, 2014).

Two full-scale two-story SC-SPSW specimens were tested pseudo-dynamically at NCREE. One specimen utilized the FR connection, and the other incorporated the NZ connection (Figure 5). Both were designed following the performance-based design procedures from Clayton et al. (2012b) and were based on a regular two-story prototype building located in Los Angeles, California.

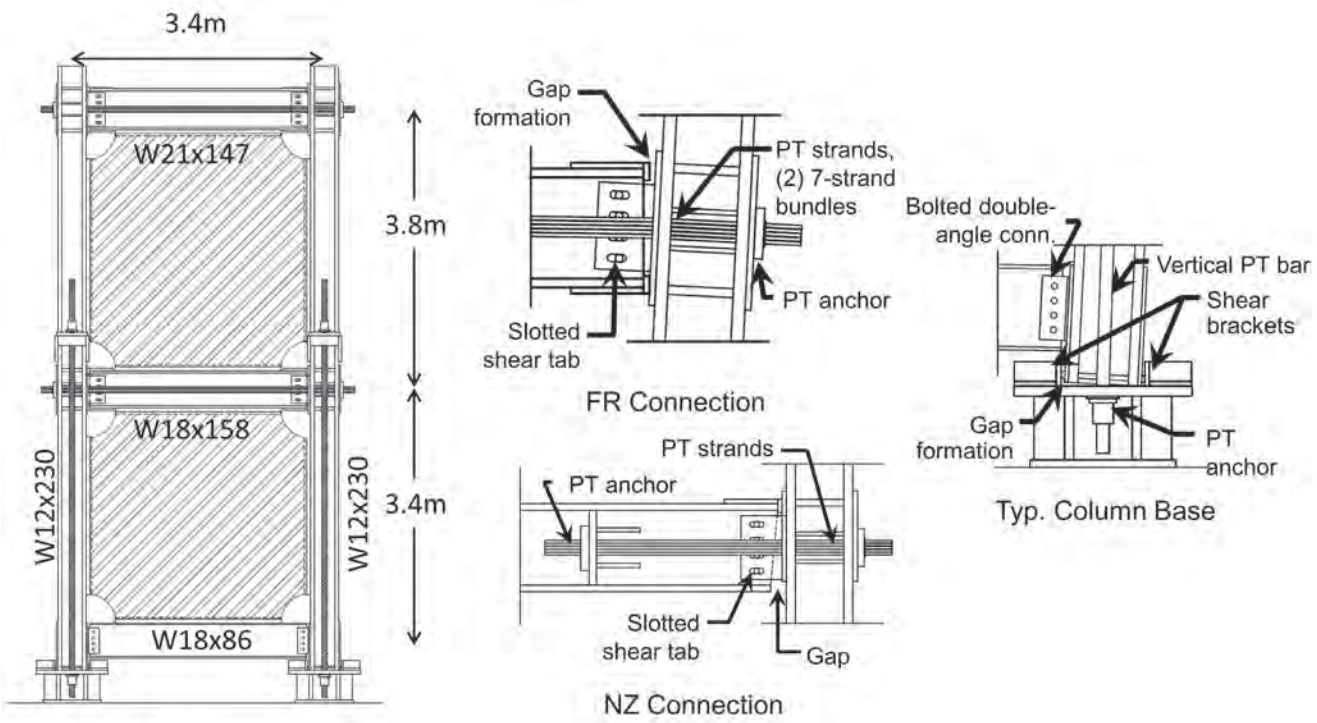

Fig. 5. SC-SPSW specimen drawing with FR, NZ and column base details.

The specimens were nominally the same, aside from the post-tensioned, beam-column connection details. At those connections, both specimens utilized shear tabs with slotted holes to accommodate the relative rotations. Bolted double-angle connections, detailed to also accommodate relative rotations, were used at the bottom beams. Web, or infill, plates with corner cut-outs were welded to fin plates at the boundary elements.

PT strands were used at the beam-column connections, and PT bars were used at the column bases. The PT strands were anchored outside of each column and ran along either side of the beam webs. The PT bars were anchored at the base and just above the middle beam connection. The PT strands and bars provided restoring forces to the connections and column bases. The PT bars also resisted column uplift. Shear resistance at the column bases was provided by bolted brackets.

The specimens were subjected to quasi-static cyclic and pseudo-dynamic (PSD) tests. PSD tests were used to evaluate the SC-SPSW response to ground motions at hazard levels of 50/50, 10/50 and 2/50. The PSD tests were followed by inelastic cyclic tests. The FR specimen was subjected to two cycles at 4.5% drift. The NZ specimen was subjected to increasing drift levels, with two cycles each at 2.5% and up to 4.5% in increments of 0.5% drift. It should be noted that no repairs were made to either specimen between tests. The specimens exhibited ductile response with recentering. Global system responses are shown in Figure 6.

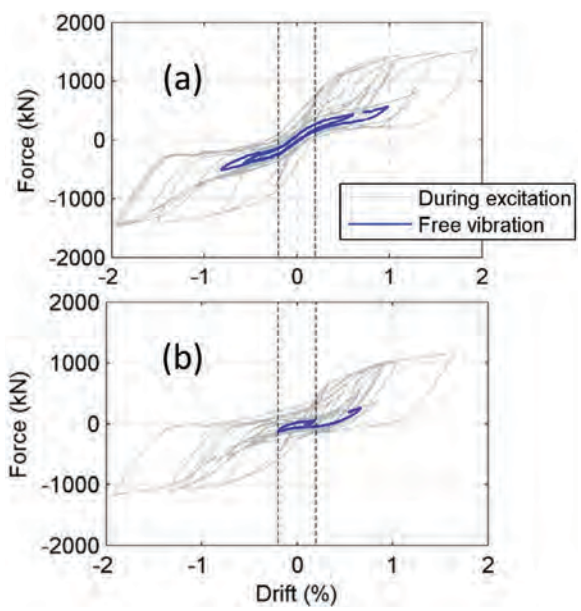

Fig. 6. Results from pseudo-dynamic testing using a ground motion representing the 10% in 50 year hazard for (a) specimen FR and (b) specimen NZ.

In the SC-SPSW specimens, the FR, NZ and PT column base connections behaved as expected. After the PSD and cyclic tests, the web plates were removed from the NZ specimen with the objective of evaluating the boundary frame. The PT frame was then subjected to quasi-static cyclic tests. The results confirmed that nearly all of the energy dissipation in the SC-SPSWs comes from the web plates. Meanwhile, about 30% of the SC-SPSW base shear resistance could be attributed to the PT boundary frame.

The SC-SPSW specimens were able to satisfy the performance objectives. Only minor web plate yielding was observed after the 50/50 hazard; therefore, no repair would be required. Some web plate tearing and minor yielding in the boundary elements (e.g., at the PT anchorage in the top beam of the NZ specimen) was observed for the 10/50 hazard. Residual drifts were less than the limit of 0.2%. Therefore, re-centering was achieved and only the web plates might need repair after the 10/50. The 2/50 event resulted in more tearing in the web plate, but boundary frames that remained essentially elastic. Recentering was also achieved, so the SC-SPSWs far exceeded the collapse prevention performance objective for the 2/50 hazard level.

WEB PLATE MODELING FOR SC-SPSWs

Investigation of the self-centering steel plate shear walls (SC-SPSWs) motivated improvements to the modeling of the web plates. The common tension strip model, a simple and generally effective method for idealizing the behavior of the web plate in conventional special plate shear walls, was shown to underestimate some important parameters. A simple modification of the tension strip model allowed for better representation of the complex web plate behavior and the seismic performance of the SC-SPSWs (Clayton, 2013).

Experimental and numerical research on SPSWs and SC-SPSWs has shown differences between the idealized tension strip behavior and web plates in pinned boundary frames (Clayton et al., 2012a; Clayton et al., 2013; Webster, 2013). For example, the web plate provides resistance during unloading as well as exhibiting strength and stiffness earlier in repeated cycles of loading than represented by the tension strip model. Figure 7 shows a comparison of one cycle (Exp) from a test of an SC-SPSW to the predicted force-drift curve from the tension strip, or tension-only, model (noted as TO in Figure 7). In SC-SPSWs, the web plates provide most of the energy dissipation in the system, so a model that could more accurately capture the web plate behavior would improve evaluation of seismic performance.

Modeling approaches for the web plate were investigated along with a couple of options for the post-tensioned boundary frame (PT-BF). Models of the two-story SC-SPSW specimen tested at NCREE were developed and analyzed. The web plate models included strip models (line elements)

with tension-only or tension-compression capacity, or shell elements with isotropic or kinematic hardening. Shell elements were also capable of simulating web plate buckling. The PT-BF was modeled with either line elements or shell elements. The shell PT-BF models also included representation of components such as continuity plates, reinforcement plates and double-angle shear connections (simulated with springs in the shell models; modeled as pins in the line element models). Models were subjected to the displacement history measured during one of the pseudo-dynamic tests.

Shell elements for the PT-BF exhibited more strength and energy dissipation. However, as long as the PT-BFs remained elastic, the differences between the line and shell elements results were not significant. For the web plate shell elements, the measured web plate demands were bounded by the results for the different hardening rules. A combined hardening rule might best represent the web plate behavior.

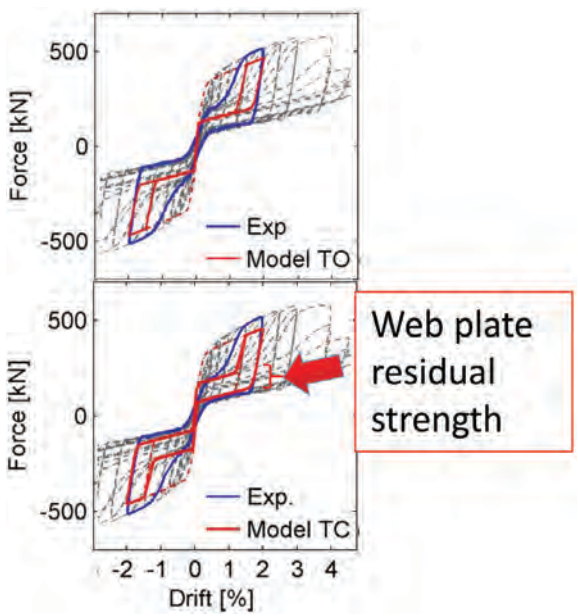

Fig. 7. Comparison of strip model hysteretic behaviors with experimental results for SC-SPSWs.

The results highlighted some benefits to using tension-compression strips. Compared to the tension-only strips, the tension-compression strips for the web plate provided better but still conservative estimates of energy dissipation, peak drift demands and residual drifts for the SC-SPSWs (see TC curve in Figure 7). The web plate strip models were also used in nonlinear response history analyses of three- and nine-story prototype SC-SPSWs for evaluation of effect on seismic performance. Use of the tension-compression strip models resulted in better performance than that predicted with the tension-only strips.

WEB PLATES CONNECTED TO BEAMS ONLY

Further investigation of the SC-SPSWs included the concept of connecting the web plates to the beams only. This change would eliminate the complex web plate demands on the columns, allowing for reduced column sizes. It would also improve energy dissipation in SC-SPSWs by delaying or preventing the web plate tearing that typically begins near the corners of the panel. Furthermore, for SC-SPSWs with FR connections, the PT frame expansion would no longer cause additional strains on the web plates. This expected behavior was validated by a two-story, large-scale specimen from quasi-static subassembly test program, and comparison to a fully-connected specimen (Figure 8; Clayton et al., 2013).

Cost-savings would be another benefit to using SC-SPSWs with web plates connected to the beams only. Although the web plates would need to be thicker than in their fully-connected counterparts, this increase in material could be offset by decreases in boundary frame member sizes. Furthermore, labor for installation of the web plates would be decreased.

The beam-only connected web plates were further investigated through nonlinear dynamic analysis. The tension-compression strip model described in the previous section was used. Three- and nine-story SC-SPSW prototype frames were designed for the performance levels defined by Clayton et al. (2012b) and used for the NCREE test specimens. The frames were computationally subjected to ground motions for 50/50, 10/50 and 2/50 hazard levels. Responses

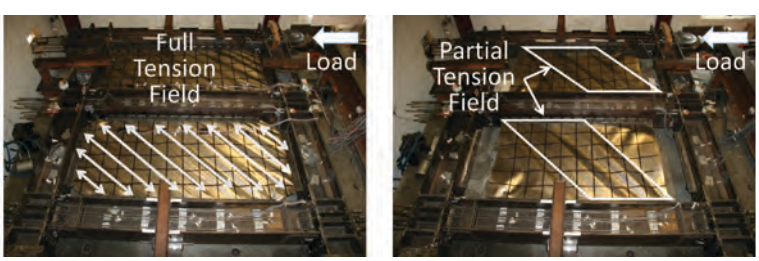

Fig. 8. Development of tension fields in a fully-connected (left) and beam-only (right) SC-SPSW.

of SC-SPSWs with beam-only and fully-connected web plates were compared. The results demonstrated that the beam-only SC-SPSWs were able to meet the performance objectives and are a viable alternative (Clayton et al., 2014).

FUTURE DIRECTIONS

Additional research is under way by the project team to:

1. Finalize a material model for use in OpenSees that is capable of representing complex web plate behavior including buckling, hardening, plastic contraction and other phenomena. The model will enable the most accurate representation of web plate behavior using strip models developed to date.
2. Finalize recommendations for considering web plate strain hardening in capacity design of SPSW beams and columns. These recommendations are based on observations from some of the experiments described above and extensive finite element modeling.
3. Explore the use of significantly smaller columns in SC-SPSWs using modified performance objectives and less conservative models of web plate strength and stiffness. Numerical analysis in OpenSees is being conducted to explore the performance of SC-SPSWs.
4. Finalize recommendations for SPSW-WC seismic design parameters (R, Ω_0 and C_d).

Related work includes research by Purba and Bruneau (2014) on seismic design parameters (R, Ω_0 and C_d) and different design approaches for SPSWs (Purba, 2014). Low and moderate seismic regions may also realize the benefits of ductile SPSWs based on research by Driver and Moghimi (2011). Modular, field-bolted SPSWs may provide economical, viable options for resisting the lower demands in these zones. As noted in Berman (2014), SPSW research has been active, and the technology is advancing. The results are some exciting possibilities for economical and resilient steel plate shear wall design.

ACKNOWLEDGMENTS

Special thanks to Jeffrey Berman, Larry Fahnestock, Patricia Clayton, David Webster, Daniel Borello, and Daniel Dowden for their contributions to this article. Financial support for the research was provided by the National Science Foundation (NSF) as part of the George E. Brown Network for Earthquake Engineering Simulation (CMMI-0830294). Patricia Clayton was also supported by the NSF East Asia and Pacific Summer Institute program (OISE-1209569) and by an NSF Graduate Research Fellowship (DGE-0718124). The researchers would also like to acknowledge material donations from the American Institute of Steel Construction.

REFERENCES

AISC (2008), "L.A. Live Hotel & Residences: An Innovative Steel-Plate Shear Wall Solution," AISC, 2008, Web, 14 Dec. 2014.

AISC (2010a), *Seismic Provisions for Structural Steel Buildings*, ANSI/AISC 341-10, Chicago, IL.

AISC (2010b), *Code of Standard Practice for Structural Steel Buildings and Bridges*, AISC 303-10, Chicago, IL.

ASCE (2010), *Minimum Design Loads for Buildings and Other Structures*, ASCE 7, American Society of Civil Engineers, Reston, VA.

Berman, J.W. (2014), "Advances in Steel Plate Shear Walls," *Structure*, NCSEA/SEI/CASE, September, pp. 26–28.

Borello, D.J. and Fahnestock, L.A. (2012). "Behavior and Mechanisms of Steel Plate Shear Walls with Coupling," *Journal of Constructional Steel Research*, Vol. 74, pp. 8–16.

Borello, D.J. and Fahnestock, L.A. (2013), "Seismic Design and Analysis of Steel Plate Shear Walls with Coupling," *Journal of Structural Engineering*, ASCE, Vol. 139, No. 8, pp. 1263–1273.

Borello, D.J., Quinonez, A.A. and Fahnestock, L.A. (2014), "Steel Plate Shear Walls with Coupling in High Seismic Regions," *Proceedings of the 10th National Conference in Earthquake Engineering*, Earthquake Engineering Research Institute, Anchorage, AK, July.

Chao, S.-H., Goel, S.C. and Lee, S.-S. (2007), "A Seismic Design Lateral Force Distribution Based on Inelastic State of Structures," *Earthquake Spectra*, Vol. 23, No. 3, pp. 547–569.

Chi, H. and Liu, J. (2012), "Seismic Behavior of Post-Tensioned Column Base for Steel Self-Centering Moment-Resisting Frame," *Journal of Constructional Steel Research*, Vol. 78, November, pp. 117–130.

Christopoulos, C., Filiatrault, A., Uang, C.M. and Folz, B. (2002), "Post-Tensioned Energy Dissipating Connections for Moment-Resisting Steel Frame," *Journal of Structural Engineering*, ASCE, Vol. 128, No. 9, pp. 1111–1120.

Clayton, P.M., Winkely, T.B., Berman, J.W. and Lowes, L.N. (2012a), "Experimental Investigation of Self-Centering Steel Plate Shear Walls," *Journal of Structural Engineering*, ASCE, Vol. 138, July, pp. 952–960.

Clayton, P.M., Berman, J.W. and Lowes, L.N. (2012b), "Seismic Design and Performance of Self-Centering Steel Plate Shear Walls," *Journal of Structural Engineering*, ASCE, Vol. 138, January, pp. 22–30.

Clayton P.M. (2013), *Self-Centering Steel Plate Shear Walls: Subassembly and Full-Scale Testing,* PhD Dissertation, Civil and Environmental Engineering Department, University of Washington, Seattle, WA.

Clayton, P.M., Berman, J.W. and Lowes, L.N. (2013), "Subassembly Testing and Modeling of Self-Centering Steel Plate Shear Walls," *Engineering Structures,* Vol. 56, November, pp. 1848–1857.

Clayton, P.M., Berman, J.W. and Lowes, L.N. (2014), "Design and Seismic Performance of Self-Centering Steel Plate Shear Walls with Web Plates Connected to the Beams Only*," Journal of Constructional Steel Research,* December 2014.

Dowden, D.M. and Bruneau, M. (2011), "NewZ-BREAKSS: Post-Tensioned Rocking Connection Detail Free of Beam Growth," *Engineering Journal*, AISC, Second Quarter, pp. 153–158.

Dowden, D.M. and Bruneau, M. (2014), "Cyclic and Dynamic Testing of Self-Centering Steel Plate Shear Walls," *Proceedings of the 10th National Conference on Earthquake Engineering*, Earthquake Engineering Research Institute, Anchorage, AK, July.

Dowden, D.M., Purba, R. and Bruneau, M. (2012), "Behavior of Self-centering Steel Plate Shear Walls and Design Considerations," *Journal of Structural Engineering.* ASCE, Vol. 138, No.1, pp. 11–21.

Driver, R.G., Kulak, G.L., Kennedy, D.J.L. and Elwi, A.E. (1997), "Seismic Behavior of Steel Plate Shear Walls," Structural Engineering Report No. 215, University of Alberta, Edmonton, AB, Canada.

Driver, R.G. and Moghimi, H. (2011), "Modular Construction of Steel Plate Shear Walls for Low and Moderate Seismic Regions," *Proceedings*, Structures Congress, Structural Engineering Institute, American Society of Civil Engineers, April 14–16, Las Vegas, NV.

FEMA (2000), *FEMA 355: State of the Art Report on System Performance of Steel Moment Frames Subject to Earthquake Ground Shaking,* Report No. FEMA-355C, FEMA, Washington, DC.

Garlock, M., Ricles, J. and Sause R. (2005), "Experimental Studies of Full-Scale Post-Tensioned Steel Connections," *Journal of Structural Engineering*, ASCE, Vol. 131, No. 3, pp. 438–448.

Ghosh, S., Adam, F., and Das, A. (2009), "Design of Steel Plate Shear Walls Considering Inelastic Drift Demand," *Journal of Constructional Steel Research*, Vol. 65, No. 7, pp. 1431–1437.

Lewis, G. (2010), *Replaceable Shear and Flexural Links for the Linked Column Frame System,* MS Thesis, Portland State University, Portland, OR.

Purba, R. (2014), *Seismic Performance of Steel Plate Shear Walls Considering Various Design Approaches*, PhD Dissertation, State University of New York at Buffalo, Buffalo, NY.

Purba, R. and Bruneau, M. (2014), "Seismic Performance of Steel Plate Shear Walls Considering Various Design Approaches," *Proceedings of the 10th National Conference on Earthquake Engineering*, Earthquake Engineering Research Institute, Anchorage, AK, July.

Sabelli, R. and Bruneau, M. (2006), *Steel Plate Shear Walls,* Design Guide 20, American Institute of Steel Construction, Chicago, IL.

Seilie, I.F. and Hooper, J.D. (2005), "Steel Plate Shear Walls: Practical Design and Construction," *Modern Steel Construction*, AISC, April.

Webster D.J. (2013), *The Inelastic Seismic Response of Steel Plate Shear Wall Web Plates and Their Interaction with the Vertical Boundary Members*, PhD Dissertation, University of Washington, Seattle, WA.

Webster D.J., Berman J.W. and Lowes L.N. (2014), "Experimental Investigation of SPSW Web Plate Stress Field Development and Vertical Boundary Element Demand," *Journal of Structural Engineering*, ASCE, Vol. 140, No 6, June, http://dx.doi.org/10.1061/(ASCE)ST.1943-541X.0000989.

GUIDE FOR AUTHORS

SCOPE: The ENGINEERING JOURNAL is dedicated to the improvement and advancement of steel construction. Its pages are open to all who wish to report on new developments or techniques in steel design, research, the design and/or construction of new projects, steel fabrication methods, or new products of significance to the uses of steel in construction. Only original papers should be submitted.

GENERAL: Papers intended for publication may be submitted by mail to the Editor, Keith Grubb, ENGINEERING JOURNAL, AMERICAN INSTITUTE OF STEEL CONSTRUCTION, One East Wacker Drive, Suite 700, Chicago, IL, 60601, or by email to grubb@aisc.org.

The articles published in the *Engineering Journal* undergo peer review before publication for (1) originality of contribution; (2) technical value to the steel construction community; (3) proper credit to others working in the same area; (4) prior publication of the material; and (5) justification of the conclusion based on the report.

All papers within the scope outlined above will be reviewed by engineers selected from among AISC, industry, design firms, and universities. The standard review process includes outside review by an average of three reviewers, who are experts in their respective technical area, and volunteers in the program. Papers not accepted will not be returned to the author. Published papers become the property of the American Institute of Steel Construction and are protected by appropriate copyrights. No proofs will be sent to authors. Each author receives three copies of the issue in which his contribution appears.

MANUSCRIPT PREPARATION: Manuscripts must be provided in Microsoft Word format. Include a PDF with your submittal. View our complete author guidelines at **www.aisc.org/ej**.

There's always a solution in steel.

ENGINEERING JOURNAL
American Institute of Steel Construction
One East Wacker Drive, Suite 700
Chicago, IL 60601

312.670.2400 www.aisc.org